

Construct accurate multi-continuum micromorphic homogenisations in multi-D space-time with computer algebra

A. J. Roberts *

July 8, 2024

Abstract

Homogenisation empowers the efficient macroscale system level prediction of physical problems with intricate microscale structures. Here we develop an innovative powerful, rigorous and flexible framework for asymptotic homogenisation of dynamics at the *finite* scale separation of real physics, with proven results underpinned by modern dynamical systems theory. The novel systematic approach removes most of the usual assumptions, whether implicit or explicit, of other methodologies. By no longer assuming averages the methodology constructs so-called multi-continuum or micromorphic homogenisations systematically based upon the microscale physics. The developed framework and approach enables a user to straightforwardly choose and create such homogenisations with clear physical and theoretical support, and of highly controllable accuracy and fidelity.

Contents

1	Introduction	3
2	Systematic multi-continuum homogenisation for 1-D spatial systems	8
2.1	Phase-shift embedding	11
2.2	Invariant manifolds of multi-modal any-order homogenization	12
2.2.1	Multi-modal, multi-continuum, models exist	14
2.2.2	Multi-modal, multi-continuum, models are relevant	14
2.2.3	Construct multi-modal, multi-continuum, homogenisations	15

*University of Adelaide, South Australia. <http://orcid.org/0000-0001-8930-1552>, <mailto:profajroberts@protonmail.com>

2.2.4	Analogy with machine learning	16
3	An example three-mode, tri-continuum, homogenization	17
3.1	Iteration systematically constructs	18
3.2	High-order three-mode homogenization	20
3.2.1	Convergence in heterogeneity a	20
3.2.2	Convergence in spatial wavenumber	20
3.3	Homogenise heterogeneous nonlinearity	22
4	An example of high-contrast multi-continuum homogenisation	23
4.1	Spectrum at each equilibrium	24
4.1.1	High-contrast thin layer	26
4.2	One-mode slow manifold model	28
4.3	Two-mode, bi-continuum, homogenisations exist and emerge .	30
4.4	Three-mode, tri-continuum, homogenisation exist and emerge	32
4.5	Homogenise nonlinear high-contrast heterogeneity	33
5	General multi-continuum, multi-mode, homogenisation of heterogeneity	35
5.1	Phase-shift embedding	38
5.2	Invariant manifolds of multi-continuum, micromorphic, any-order homogenization	41
5.2.1	Linear basis of invariant manifolds	42
5.2.2	Systems with significant dissipation	45
5.2.3	Wave-like systems	48
5.2.4	Fractional differential evolution	51
5.2.5	Improving spatial resolution	53
5.3	Construct a chosen invariant manifold multi-continuum homogenisation	56
6	Example in 2D elasticity homogenisation	57
6.1	Example cell problem	58
6.2	Phase-shift embedding of the 2D heterogeneity	61
6.3	Basis of invariant manifolds	62
6.4	Construct multi-continuum homogenisations	63
6.4.1	Classic 2-D homogenisation	63
6.4.2	Higher-order homogenisation	64
6.4.3	Tri-continuum homogenised model	65
7	Conclusion	66
A	Computer algebra construction	68
A.1	Iteration systematically constructs multi-modal model	69
A.2	Post-process	71

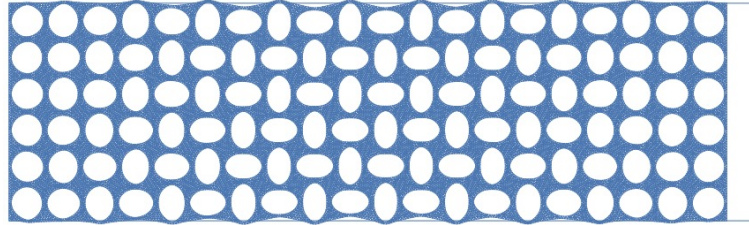
<i>1</i>	<i>Introduction</i>	3
B	Computer algebra construction of high contrast example	72
B.1	Parametrise a non-dimensional case	73
B.2	Spectrum of cell problem	74
B.3	Form inverse for homological updates	76
B.4	Iteration systematically constructs multi-modal model	77
B.5	Post-process	78
C	Computer algebra constructs 2-D elastic homogenisation	79
C.1	Compute the cell operator	81
C.2	Finds eigenmodes via cell Jacobian and SVD	82
C.3	Iteration systematically constructs multi-modal model	84
C.4	Post-process	86
D	General solution of modal fractional differential equation	87

1 Introduction

In most standard constitutive models for the mechanical behaviour of solids, the stress at a given point uniquely depends on the current deformation gradients (e.g., [Bažant & Jirásek 2002](#)). However, modern designed meta-materials have exceptional mechanical properties that depend largely on the intricate underlying complicated microstructure, rather than the bulk properties of their constituent materials (e.g., [Sarhil et al. 2024](#)). So-called multi-continuum or micromorphic homogenisations, or generalized Cosserat theories, are enhanced models which aim to capture the significant macro-scale effects of such heterogenous microstructure without fully-resolving the microstructures (e.g., [Alavi et al. 2023](#)). [Figure 1](#) shows one example of a microstructured material whose macroscale deformation can only adequately be predicted by the generalised modelling of non-standard microscale modes ([Rokoš et al. 2019](#)). The pioneering vision of [Muncaster \(1983a\)](#) was that the dynamical systems concept of invariant manifolds would provide a general rigorous route to coarse-scale modelling of nonlinear dynamics in mechanics. Here we develop a flexible, systematic and practical approach to the multi-continuum homogenisation modelling of heterogeneous systems (such as the material deformation of [Figure 1](#)) using modern developments in the rigorous theory and application of invariant manifolds for nonlinear dynamical systems ([Aulbach & Wanner 2000](#), [Potsche & Rasmussen 2006](#), [Haragus & Iooss 2011](#), [Roberts 2015a](#), [Bunder & Roberts 2021](#)).

This article greatly extends a novel dynamical systems approach ([Bunder & Roberts 2021](#)) to multi-continua/micromorphic homogenisation in two major parts. The first part, [Sections 2 to 4](#), introduce the key ideas and methods in the more accessible scenario of the linear self-adjoint dynamics of a scalar field in space-time with one large spatial dimension and microscale

Figure 1: 4% compression of a material with circular inclusions, seen near either end, may develop a nontrivial microscale structure, seen near the middle (from Figure 4(2nd) of Guo et al. (2024)). Macroscale homogenisation of such microscale structures may best be via a multi-continuum model.



periodic heterogeneity. The second part, Sections 5 and 6, develops the framework and theory of the methodology, and an application, to a wide class of nonlinear non-autonomous dynamics of a general field in space-time with arbitrary number of ‘large spatial’ dimensions and heterogeneity on both the macroscale and quasi-periodic microscale. For an example in 2-D elasticity: Section 6.4.2 derives a homogenisation in terms of *high-order gradients* of the usual two mean displacements; whereas Section 6.4.3 derives a *tri-continuum* homogenisation in three degrees of freedom as determined by the sub-cell physics of the heterogeneous elasticity.

Three broad families of methods enhance standard homogenisation (e.g., Bažant & Jirásek 2002, Forest & Trinh 2011, Sarhil et al. 2024): firstly, introduce extra fields, the multi-continua, that provide supplementary information on the small-scale kinematics; secondly, improve the resolution of the standard displacement-field modelling by incorporating higher-order gradients; and thirdly, introduce nonlocal effects into the homogenisation. Our systematic dynamical systems framework and results unifies the approach and connects to all three of these families, in order: firstly, multi-continuum Cosserat-like theories *are* the central theme; secondly, higher-order gradient models are invoked for examples of both basic homogenisation (Sections 4.2 and 6.4.2) and also multi-continua homogenisation (Sections 3.2, 4.3 and 4.4); and lastly, examples of accurate nonlocal models are created by regularising some of the higher-order models (Sections 3.2.2 and 4.2). Craster (2015) commented that “Homogenization theory is typically limited to static or quasi-static low frequency situations and the purpose of this contribution is to briefly review how to tackle dynamic situations” Our contribution also focusses on dynamics, with statics being the special case of no time variations.

Introduce the novel methodology In a plenary lecture Forest & Trinh (2011) discussed that “in most cases . . . proposed extended homogenization procedures [for micromorphic continua] remain heuristic”. In contrast, the

novel approach here is created by innovatively synthesising three separate ingredients from the mathematics of dynamical systems. Let's summarise the three ingredients.

- Firstly, it seems paradoxical that macroscale homogenisations have translationally invariant symmetry in space, say \boldsymbol{x} , given that the underling microscale is spatially heterogeneous in \boldsymbol{x} . Here is that we embed the given heterogeneous problem in the family of all phase-shifted problems (Sections 2.1 and 5.1). In the special embedding, the family of problems is translationally symmetric in \boldsymbol{x} , with the heterogeneity in an orthogonal 'thin space' dimension. Consequently, homogenisation then preserves the embedded system's translational symmetry in \boldsymbol{x} .
- Secondly, the orthogonal 'thin space' dimension gives rise to the classic cell-problem (RVE problem) with periodicity naturally required (Sections 2.2 and 5.2). Then the theory of invariant manifolds supports choosing multi-continuum modes from the eigenmodes corresponding to small eigenvalues because for a wide range of circumstances one is then guaranteed the multi-continuum modelling is exponentially quickly emergent (Section 5.2.2) Such multi-mode modelling in spatially extensive systems was initiated by Watt & Roberts (1995) for the shear dispersion in flow along a channel.
- Thirdly, recently Bunder & Roberts (2021) developed an invariant manifold at each spatial locale, weakly coupled to neighbouring locales, via a multivariate Taylor series in space. A new remainder term for the series (Bunder & Roberts 2021, expression (44)) quantifies the error of the modelling so that the multiscale homogenisation is valid simply wherever and whenever the remainder term is small enough for the purposes at hand.

Recently, Alavi et al. (2023) [p.2166] noted one limitation of other approaches is that "proper elaboration of the macroscopic kinematic and static quantities that pertain to the micromorphic continuum is a problematic issue . . . [previous] works did not relate macroscopic to microscopic kinematic quantities and they did not formulate a boundary value problem at the microscale." In contrast, here embedding the system provides via dynamics theory a sound boundary value problem (e.g., (2.4) and (5.4)), and the constructed invariant manifolds explicitly connect the microscale to the selected macroscale kinematic quantities (e.g., (3.3) and (4.6a)).

Strong theoretical support Alavi et al. (2023) [p.2165] also commented that "Periodic homogenization methods . . . are most of the time lacking a clear mathematical proof of convergence of the microscopic solution towards

the limit solution for vanishing values of the scale parameter” Complementing this, in their review [Fish et al. \(2021\)](#) discuss that [p.775] “Mathematical homogenization theory based on the multiple-scale asymptotic expansion assumes scale separation.” Such scale separation is usually defined as the mathematical limit $\ell/L \rightarrow 0$ for microscale lengths ℓ and macroscale lengths L . Here there is *no* such limit assumed. Instead, using established dynamical systems theory of invariant manifolds provides such proofs in two main cases (e.g., [Aulbach & Wanner 2000](#), [Potsche & Rasmussen 2006](#), [Haragus & Iooss 2011](#), [Roberts 2015a](#), [Bunder & Roberts 2021](#)). The first case is that of systems with some damping for which [Section 5.2.2](#) creates a framework with clear mathematical proofs of the existence of models with exact closure, with convergence in time to the macroscale model, and that is controllably approximated. The second case is that of undamped, wave-like, systems where [Section 5.2.3](#) argues that we can prove that constructed nearby systems possess exact guiding-centre macroscale homogenisations. Moreover, these proofs are not just for the vanishing scale parameter limit, but for the finite scale separations of real applications.

[Alavi et al. \(2023\)](#) [pp.2164–5] discussed how “generalized continuum models ... face some limitations in their capability to predict microstructures’ supposedly intrinsic mechanical properties accurately.” Similarly, [Fish et al. \(2021\)](#) [p.776] commented that “In upscaling methods, the fine-scale response is approximated or idealized, and only its average effect is captured.” In contrast, invariant manifold theory guarantees the existence of an *exact* closure for multi-continuum homogenisations in some domain ([Section 5.2](#)), a closure that exactly captures the fine-scale response. Importantly, our approach does *not* invoke assumed averaging. Further, theory ([Potsche & Rasmussen 2006](#)) guarantees we approximate the exact closure to a controllable accuracy.

Quantifying errors and uncertainty In a broad-ranging discussion of multiscale simulation of materials, [Chernatynskiy et al. \(2013\)](#) [p.160] asserted that “quantifying the errors at each scale is challenging, quantifying how those errors propagate across scales is an even more daunting task” which has two aspects rectified here. Firstly, as mentioned above, our approach connects with innovative quantitative estimates for the remainder error incurred by the macroscale modelling: in the case of one large spatial dimension via expression (23) of [Roberts \(2015a\)](#); in the case of multiple large dimensions via expression (44) of [Bunder & Roberts \(2021\)](#). Secondly, the dynamical systems framework established here comes with (in future research) a systematic accurate projection of initial conditions (e.g., [Roberts 1989](#), [Watt & Roberts 1995](#)). The same projection also rationally propagates errors and uncertainty from micro- to macro-scales. Thus error propagation no longer need be such a “daunting task”.

Clarify and guide the hierarchy of multi-continua choices Rizzi et al. (2021) [p.2253] concluded that “It is thus an an important future task ... to derive guidelines for a favorable choice among the numerous available micromorphic continuum models.” The dynamical systems approach established here clarifies and guides the choice of multi-continuum models depending upon the space-time scales the modelling needs to resolve. Sections 2.2, 4.1, 5.2 and 6.4 organise choices into a sequence of possibilities, and then guides a choice in the sequence depending upon the spatio-temporal scales of interest in the envisaged scenarios of application.

Alavi et al. (2023) [p.2164] also raises the “difficulty to choose a priori an appropriate model for a given microstructure. Enriched continuum theories are required in such situations to capture the effect of spatially rapid fluctuations at the mesoscopic and macroscopic levels. ... micromorphic homogenization raises specific difficulties compared to higher gradient and higher-order theories” The dynamical systems framework herein, as discussed by Section 5.2.5, empowers us to also guide the selection of multi-continuum modes aimed to improve spatial resolution, irrespective of the temporal resolution.

Efendiev & Leung (2023) also use a spectral decomposition to guide multi-continuum models. However, they require macroscale variables U_i to be *averages* and hence deduce [p.3] “unless there is some type of high contrast, the averages ... will become similar” which leads them to conclude [p.16] that for “multi-continuum models, ... one needs high contrast to have different average values”. In contrast, the approach here is *not* wedded to averaging, so is more flexible, and need not be limited to high contrast (although Section 4 details a high contrast example, the example of Section 3 is not). By measuring and being based upon whatever structures the physical equations tell us about sub-cell dynamics we here form and justify more general multi-continuum models.

Moreover, many commonly made assumptions are not needed here. There are no guessed fast/slow variables, no small ϵ s, no limits, no need to assume a variational formulation, nor energy functional, nor presume specific sub-cell modes, nor need oversampling regions, nor assume boundary conditions for RVEs, nor assume multiple times scaled by powers of a small ϵ .

Computer algebra handles complicated details Rizzi et al. (2021) [p.2237] began by highlighting that a “basic problem of all these theories ... is the huge number of newly appearing constitutive coefficients which need to be determined.” The systematic nature of our approach, together with theoretical support (e.g., Potzsche & Rasmussen 2006), empowers computer algebra to routinely handle the potentially “huge number” of constitutive coefficients via a robust and flexible algorithm introduced by Roberts (1997)

and documented for many applications in a subsequent book (Roberts 2015*b*). Appendices A to C list adaptable code for the three major examples of Sections 3, 4 and 6—the latter two integrating fine-scale numerics with the macroscale algebra. These codes specifically use the computer algebra system Reduce¹ as it is free, flexible, and fast (Fateman 2003).

Alavi et al. (2023) [p.2164] commented that “micromorphic homogenization raises specific difficulties compared to higher gradient and higher-order theories” In contrast, here we apply the same theoretical and practical framework for all cases with no difficulty, indeed with the same code via just a couple of parameter changes to change from standard to multi-continuum micromorphic homogenisations, and from leading order to any arbitrary higher-order.

Let’s proceed with the basics of the approach in 1-D space, Sections 2 to 4, before addressing the complexities of general nonlinear systems in multi-D space, Sections 5 and 6.

2 Systematic multi-continuum homogenisation for 1-D spatial systems

The idea here is to establish and construct so-called multi-continuum or micromorphic homogenised models in 1-D space. Now a “multi-continuum” or “micromorphic” model is phrased in terms of microscale structures/modes that have macroscale variations—in essence pursuing models with multiple mode-shapes in the microscale (e.g., Rokoš et al. 2019, Alavi et al. 2023, Sarhil et al. 2024). Here we develop multi-continuum homogenisation by the novel combination of analysing the ensemble of phase-shifts (Roberts 2015*a*) via innovations to the multi-modal dynamical systems modelling of Watt & Roberts (1995).

The distinguishing feature here is that we let the microscale physical dynamics of the system inform and determine almost all decisions. We do not assume any particular weighted averages are appropriate for variables, nor do we assume any particular weighted averages are appropriate for any upscaling dimensional reduction. The *only* subjective decision made herein is how many microscale modes one wishes to resolve in the multiscale modelling. This decision is strongly guided by the physics-determined spectrum of the microscale (Sections 4.1 and 5.2).

Consider materials with complicated microstructure. We want to model their macroscale dynamics over a large scale L by equations with effective ‘average’ coefficients, but *without presuming* any averaging. Heterogeneous second-order systems in 1-D space are the simplest such class of systems:

¹<http://www.reduce-algebra.com>

suppose the material, in spatial domain $[0, L]$, has structure so that ‘material’ or ‘heat’ $u(t, x)$ evolves according to the PDE

$$\frac{\partial^\alpha u}{\partial t^\alpha} = \frac{\partial}{\partial x} \left\{ \kappa(x) \frac{\partial u}{\partial x} \right\}, \quad 0 < x < L, \quad (2.1)$$

where the heterogeneous material coefficient $\kappa(x)$ has some complicated microscale structure on a microscale length ℓ , and so the solution field $u(t, x)$ has complicated multiscale structures. We assume that the coefficient $\kappa(x)$ is regular enough that there exist general solutions $u(t)$ in the Sobolev space $W^{2,2}([0, L])$.

The time evolution operator $\partial^\alpha / \partial t^\alpha$, usually written ∂_t^α herein, covers many cases: $\alpha = 1$ is a prototypical diffusion problem; $\alpha = 2$ is a prototypical wave problem; fractional α could represent the fractional calculus operator; but potentially ∂_t^α could represent any in a wide variety of time evolution operators that commutes with spatial derivatives, such as the time-step operator $\partial_t^\alpha u \mapsto (u|_t - u|_{t-\tau})/\tau$. We primarily discuss the two main cases of diffusive-like dynamics and of wave-like dynamics, $\alpha = 1, 2$ respectively.

Our approach provides a homogenisation at *finite* scale separation ℓ/L of real scenarios, we *do not* take the limit $\ell/L \rightarrow 0$. The approach is informed by the emergent physics arising from the microscale interactions. However, we require that the length L is sufficiently large that we can focus on modelling interesting dynamics in the interior of the domain, say the open set $\mathbb{X} \subset [0, L]$, significantly away from the boundaries at $x = 0, L$ and the associated boundary layers. A systematic and accurate homogenisation modelling of physical boundaries and associated boundary layers in multiscale homogenisation is a topic for future research (perhaps via the approach of [Roberts 1992](#), [Chen et al. 2018](#)).

For the multiscale PDE (2.1), and in the diffusive case $\alpha = 1$, [Roberts \(2024\)](#) derived, supported, and characterised the *one-mode* macroscale homogenised PDE

$$\partial_t^\alpha U = KU_{xx} + \dots, \quad \text{for } x \in \mathbb{X}, \quad (2.2)$$

for some effective mean field $U(t, x)$, some macroscale effective material constant K , with some higher order corrections denoted by the ellipsis \dots , and a potentially quantified error estimate (via (23) of [Roberts 2015a](#)). Instead of the one-mode model (2.2), the task here is to argue for, theoretically support, and construct, a multi-continuum, micromorphic, multi-modal homogenisation model. The main aim for such a multi-continuum homogenisation is to improve the space-time resolution over that of (2.2).

For an example, [Section 3](#) develops a three-mode, tri-continuum, homogenisation expressed in terms of three macroscale quantities U_0, U_1, U_2 , defined by the microscale physics, that evolve within \mathbb{X} according to the three

macroscale PDEs

$$\begin{aligned}\partial_t^\alpha U_0 &= kU_{0xx} - \frac{1}{2}aU_{1x} + \dots, & \partial_t^\alpha U_1 &= -U_1 + aU_{0x} + \dots, \\ \partial_t^\alpha U_2 &= -U_2 + 2U_{1x} + \dots.\end{aligned}\tag{2.3}$$

Because our sound modelling is transitive, the classic homogenised one-mode PDE (2.2) may be recovered by the adiabatic quasi-equilibrium approximation of the second mode in (2.3): this adiabatic approximation gives $U_1 \approx aU_{0x}$. Consequently, the first PDE of (2.3) reduces to the usual homogenised macroscale PDE $\partial_t^\alpha U_0 \approx (k - \frac{1}{2}a^2)U_{0xx}$.

Generalisations to any number of multi-continuum modes are straightforward, as coded in the computer algebra of [Appendices A](#) and [B](#) for the respective examples of [Sections 3](#) and [4](#).

[Fish et al. \(2021\)](#) [p.774] identified that a challenge for “a multiscale approach involves a trade-off between increased model fidelity with the added complexity, and corresponding reduction in precision and increase in uncertainty”. Here there is *no* trade-off with increased fidelity: both here and in [Section 5](#) we establish a framework with proven controllable precision and certainty.

The theoretical support for multi-continuum models such as (2.3) depends upon the time evolution operator ∂_t^α . For the attributes of existence and construction, for general ∂_t^α it appears best to appeal to a version of *backwards theory* ([Roberts 2022](#), [Hochs & Roberts 2019](#)), namely that the constructed invariant manifold and homogenised evolution (2.3) thereon is *exact* for a system *close* to the specified multiscale PDE (2.1). The major practical difference among the various ∂_t^α is whether the dimension-reduced, approximate invariant manifold, multi-modal models such as (2.3) are *emergent* in time: for diffusion, $\alpha = 1$, the homogenised models are generally exponentially quickly emergent in time; for elastic waves, $\alpha = 2$, the homogenised models are best viewed as a *guiding centre* for the dynamics about the constructed manifold (e.g., [van Kampen 1985](#)); whereas for other cases the relevance of the modelling depends upon how the spectrum of the right-hand side operator of (2.1) maps into dynamics of the corresponding modes. [Section 5.2](#) discusses these cases in more detail.

Of course, if one only addresses forced equilibrium problems, or Helmholtz-like equations for a specified frequency, then the issue of whether the modelling is relevant under time evolution need not be considered.

2.1 Phase-shift embedding

Our powerful innovative alternative approach to homogenisation is to embed the specific given physical PDE (2.1) into a family of PDE problems formed by all phase-shifts of the periodic microscale (Roberts 2015a). This embedding is a novel and rigorous twist to the concept of a Representative Volume Element.

Let's create the desired embedding for PDEs (2.1) in 1-D space by considering a field $\mathbf{u}(t, x, \theta)$ satisfying the PDE

$$\frac{\partial^\alpha \mathbf{u}}{\partial t^\alpha} = \left(\frac{\partial}{\partial x} + \frac{\partial}{\partial \theta} \right) \left\{ \kappa(\theta) \left(\frac{\partial \mathbf{u}}{\partial x} + \frac{\partial \mathbf{u}}{\partial \theta} \right) \right\}, \quad \mathbf{u} \text{ } \ell\text{-periodic in } \theta, \quad (2.4)$$

in the 'cylindrical' domain $\mathbb{D} := \{(x, \theta) : x \in \mathbb{X}, \theta \in \Theta := [0, \ell]\}$. We assume the lower bound $\kappa(\theta) \geq \kappa_{\min} > 0$, and that the heterogeneity $\kappa(\theta)$ is regular enough that general solutions \mathbf{u} of PDE (2.4) are in $\mathbb{H}_{\mathbb{D}}^N := W^{(N+1, 2), 2}(\mathbb{D})$ for some chosen order N , and where we define the Sobolev space $W^{a, p}(\mathbb{D}) := \{u \in L^p(\mathbb{D}) : \partial_x^{a_1} \partial_\theta^{a_2} u \in L^p(\mathbb{D}), a_i \leq q_i\}$. For example, choose $N = 2$ for the classic (2.2) or tri-continuum (2.3) homogenisations, or choose $N \geq 4$ for higher-order homogenisations (e.g., Sections 3.2, 4.3 and 6.4.2). I emphasise that the domain \mathbb{D} of PDE (2.4) has finite aspect ratio: we do *not* take the usual scale-separation limit involving an aspect ratio tending to zero nor to infinity.

Lemma 1. *For every solution $\mathbf{u}(t, x, \theta) \in \mathbb{H}_{\mathbb{D}}^N$ of the embedding PDE (2.4), and for every phase ϕ , the defined field $u_\phi(t, x) := \mathbf{u}(t, x, x + \phi)$ is in the Sobolev space $\mathbb{H}_{\mathbb{X}}^2 := W^{2, 2}(\mathbb{X})$ and satisfies the heterogeneous diffusion PDE*

$$\frac{\partial^\alpha u_\phi}{\partial t^\alpha} = \frac{\partial}{\partial x} \left\{ \kappa(x + \phi) \frac{\partial u_\phi}{\partial x} \right\}. \quad (2.5)$$

Specifically, for the case of phase $\phi = 0$, the field $u(t, x) := u_0(t, x) = \mathbf{u}(t, x, x)$ satisfies the given heterogeneous PDE (2.1).

Note the implicit distinction among x -derivatives: $\partial/\partial x$ of \mathbf{u} is done keeping θ constant; whereas $\partial/\partial x$ of u and u_ϕ is done keeping phase ϕ constant.

Proof. The proofs for Lemmas 1 and 2 are straightforward, and are encompassed by the proofs given for Lemmas 6 and 7. \square

Here the microscale ℓ -periodic boundary conditions are *not* assumed but arise naturally due to the ensemble of phase-shifts. That is, what previously had to be assumed, here arises naturally.

Lemma 2 (converse). *Suppose we have a set of solutions $u_\phi(t, x)$ of the phase-shifted PDE (2.5)—a set parametrised by the phase vector ϕ —and the set depends smoothly enough upon t, x, ϕ that the following $\mathbf{u} \in \mathbb{H}_{\mathbb{D}}^N$. Then the field $\mathbf{u}(t, x, \theta) := u_{\theta-x}(t, x)$ satisfies the embedding PDE (2.4).*

Consequently, PDEs (2.4) and (2.5) are equivalent, and they may provide us with a set of solutions for an ensemble of materials all with the same heterogeneity structure, but with the structural phase of the material shifted through all possibilities. The critical difference between the PDEs (2.1) and (2.5) and the embedding PDE (2.4) is that although PDEs (2.1) and (2.5) are heterogeneous in space x , the embedding PDE (2.4) is *homogeneous* in x .²

2.2 Invariant manifolds of multi-modal any-order homogenization

We now analyse the embedding PDE (2.4) for useful invariant manifolds via an approach proven for systems homogeneous in the long space, x -direction. The invariant manifolds express and support the relevance of a precise multi-modal homogenization of the original heterogeneous PDE (2.1). Since the PDEs herein are linear, the invariant manifolds are more specifically invariant *subspaces*, but let's use the term *manifold* as the same framework and theory immediately generalises to related nonlinear systems as discussed in Section 5.

Rigorous theory (Roberts 2015a) inspired by earlier more formal arguments (Roberts 1988, 1997) establishes how to support and construct PDE models for the macroscale spatial structure of PDE solutions in cylindrical domains such as \mathbb{D} . The technique is to base analysis on the case where variations in x are approximately negligible, and then treat slow, macroscale, variations in x as a regular perturbation (Roberts 2015b, Part III).³

To establish the basis of an invariant manifold, consider the embedding PDE (2.4) with $\partial/\partial x$ neglected:

$$\frac{\partial^\alpha \mathbf{u}}{\partial t^\alpha} = \frac{\partial}{\partial \theta} \left\{ \kappa(\theta) \left(\frac{\partial \mathbf{u}}{\partial \theta} \right) \right\}, \quad \mathbf{u} \text{ is } \ell\text{-periodic in } \theta. \quad (2.6)$$

²After establishing this embedding, the distinction between space location x and x is largely irrelevant, and as $x = x$ hereafter we just use x .

³Alternatively, in linear problems one could justify the analysis via a Fourier transform in x (Roberts 1988, 2015b, §2 and Ch.7 resp.). However, for nonlinear problems, and also for macroscale varying heterogeneity, it is better to analyse in physical space, so we do so herein.

The basis obtained here applies in a locale around each and every $x \in \mathbb{X}$ (Roberts 2015a, §2). In general, as in some functionally graded materials and as addressed in Section 5, the details of such a basis varies with locale $x \in \mathbb{X}$. But here, because the PDEs (2.4) and (2.6) are translationally invariant in x , the following basis is independent of $x \in \mathbb{X}$.

Equilibria A family of equilibria of PDE (2.6) is, for every C , $\mathbf{u}(t, \theta) = C$ constant in θ . Because the PDE (2.6) is linear, to encompass the entire family it is sufficient to consider just the case of equilibrium $C = 0$, which we do henceforth.

Spectrum at each equilibrium Invariant manifold models (Roberts 2015a) are decided based upon the spectrum of the cell problem (2.6). In general the spectrum depends upon the microscale details of $\kappa(\theta)$.

Assumption 3. Consider the ‘cell’ eigen-problem for \mathbf{u}

$$\lambda \mathbf{u} = \frac{\partial}{\partial \theta} \left\{ \kappa(\theta) \frac{\partial \mathbf{u}}{\partial \theta} \right\}, \quad \mathbf{u} \text{ is } \ell\text{-periodic in } \theta. \quad (2.7)$$

We assume that $\kappa(\theta) \geq \kappa_{\min} > 0$ is regular enough that the eigenvalues λ are countable, real and non-positive, and also that a set of corresponding eigenfunctions in $W^{N+1,2}([0, \ell])$ are complete and orthogonal.

Let’s order the eigenvalues such that $0 = \lambda_0 > \lambda_1 \geq \lambda_2 \geq \lambda_3 \geq \dots$ (including repeats to account for multiplicity). Let $v_m(\theta)$ denote an eigenvector corresponding to the eigenvalue λ_m (suitably orthogonalised in the case of eigenvalues of multiplicity two or more).

From the family of equilibria we know the leading eigenvalue $\lambda_0 = 0$ and the corresponding $v_0(\theta)$ is constant, say normalised to $v_0 = 1$. One may construct a *slow manifold* model based upon this eigenvalue zero. Such a slow invariant manifold modelling leads to the classic homogenised PDE such as (2.2) (and its higher order generalisations). The reason for this connection to classic homogenisation is that the constant eigenvector v_0 both matches the classic *assumption* that the macroscale solutions varies little over a cell, but also matches the classic *assumption* that un-weighted cell averages give usual macroscale quantities. Here, both such properties instead *follow* from the physics-informed nature of the leading microscale eigenfunction $v_0(\theta)$.

In problems with more complicated physics, the correct corresponding properties follow from the physical nature of the leading eigenfunction: an example is modelling the macroscale advection-diffusion in field flow fractionation channels where the leading microscale eigenfunction is an exponential (e.g., Suslov & Roberts 2000, 1999).

2.2.1 Multi-modal, multi-continuum, models exist

A rational multi-modal, invariant manifold, homogenisation may be constructed based upon the M leading eigenvalues and eigenfunctions of the cell-problem (2.7), for any chosen M . The leading approximation to macroscale varying sub-cell structures is then

$$\mathbf{u}(t, x, \theta) \approx U_0 v_0(\theta) + U_1 v_1(\theta) + \cdots + U_{M-1} v_{M-1}(\theta), \quad (2.8)$$

for macroscale ‘variables’, ‘amplitudes’ or ‘order parameters’ $U_0(t, x), U_1(t, x), \dots, U_{M-1}(t, x)$ that vary acceptably slowly over macroscale x . The dynamical systems invariant manifold framework (e.g., Roberts 2015a) empowers systematically deriving corrections to (2.8) and simultaneously determining PDEs, such as (2.2) and (2.3), governing the evolution of the macro-variables U_0, \dots, U_{M-1} .

Importantly, there are only *two* subjective decisions made in this approach. The first subjective decision is where to divide the spectrum into sub-cell modes whose dynamics we model explicitly, namely v_0, \dots, v_{M-1} , and sub-cell modes which are accounted for implicitly, which are ‘slaved’, namely v_m for $m \geq M$. Herein we primarily address this scenario. The second subjective decision is to choose an order N of accuracy for the constructed M -continuum model (e.g., Section 2.2.3).

The gap in the spectrum of eigenvalues between λ_{M-1} and λ_M caters for the perturbing influence of the heterogeneity interacting with macroscale gradients of the macro-variables U_0, \dots, U_{M-1} .

However, in some scenarios other considerations lead to choosing an alternative set of modes for the modelling as Section 5.2 discusses in more detail. For example, if you know that some external forcing excites one particular mode, say numbered m^* , then you may choose to form a multi-mode model from the two sub-cell modes $m = 0, m^*$ so that then the modelling resolves the mean-mode interacting with the excited mode, and treats all other modes as ‘slaved’. One example by Touzé & Vizzaccaro (2021) is the model order reduction of the vibration response of forced nonlinear structures.

2.2.2 Multi-modal, multi-continuum, models are relevant

The argument for the relevance of the modelling founded on (2.8) is the following. However, the argument depends upon the nature of the time evolution operator ∂_t^α (Section 5.2 discusses more broadly and with detailed justification).

- In the diffusive case, $\alpha = 1$, the model is relevant because the slow centre manifold tangent to (2.8) exponentially quickly attracts solutions from all initial conditions⁴. This exponentially quick emergence is because all the slaved sub-cell modes decay roughly like $e^{\lambda_m t}$ for $m = M, M+1, \dots$. The slowest of these is $e^{\lambda_M t}$ and so we expect, and can often prove, that solutions from all initial conditions approach an M -mode invariant manifold (2.8) on times roughly $1/|\lambda_M|$.
- In the wave case, $\alpha = 2$, all sub-cell eigenfunction modes are oscillatory with frequency $\omega_m := \sqrt{-\lambda_m}$. Hence any invariant manifold founded on (2.8) appears not to be emergent. Instead, one may argue its relevance via one of at least three sub-cases:
 - there may be physical processes not represented in the sub-cell dynamics (2.6) that cause sufficient attraction to the chosen M -mode subspace (2.8);
 - or one views the model as a *guiding centre* for the dynamics on timescales longer than $1/\omega_M$ about the constructed manifold (e.g., van Kampen 1985), despite controversies about the existence of such slow manifold models (e.g., Lorenz & Krishnamurthy 1987, Roberts 2015b, §13.5.3), controversies that may be resolved via backwards theory (e.g., Hochs & Roberts 2019);
 - or one is only interested in predicting equilibria in which case attraction and emergence is largely irrelevant.

2.2.3 Construct multi-modal, multi-continuum, homogenisations

The construction of multi-continuum homogenisation relies on theory proven by Roberts (2015a), which in turn rests on general theory by Aulbach & Wanner (2000), Potzsche & Rasmussen (2006), Hochs & Roberts (2019). Corollary 13 of Roberts (2015a) proves that an established procedure (Roberts 1988, 1997) is indeed a rigorous method to construct invariant manifold PDEs such as (2.3). The crucial result is that if a derived approximation satisfies the embedding PDE (2.4) to a residual of $\mathcal{O}(\partial_x^{N+1})$, then the corresponding homogenisation is correct to an error $\mathcal{O}(\partial_x^{N+1})$. Practical procedures to derive approximations to any chosen order of residual were developed for multi-modal models by Watt & Roberts (1995). These procedures and its techniques are further developed herein to homogenisation problems.

We adapt a computer algebra version of a procedure (Roberts 1997), detailed in generality and examples of the book (Roberts 2015b, Part III), and as summarised here. Define the vector of local amplitudes $\mathbf{U}(t, x) :=$

⁴(e.g., Aulbach & Wanner 2000, Prizzi & Rybakowski 2003, Roberts 2015a)

(U_0, \dots, U_{M-1}) . We seek an invariant manifold of the embedding PDE (2.4) in the form $\mathbf{u}(t, x, \theta) = v(\mathbf{U}, \theta)$ such that $\partial_t^\alpha \mathbf{U} = G(\mathbf{U})$ where the right-hand side dependence upon \mathbf{U} implicitly involves its gradients $\mathbf{U}_x, \mathbf{U}_{xx}$, etc. For any given approximations \tilde{v}, \tilde{G} to v, G , define $\text{Res}(\tilde{v}, \tilde{G})$ to be the residual of the embedding PDE (2.4). Compute corrections v', G' to an approximations \tilde{v}, \tilde{G} by solving a variant of the usual linear cell problem forced by the residual, namely

$$\frac{\partial}{\partial \theta} \left\{ \kappa(\theta) \frac{\partial v'}{\partial \theta} \right\} - \sum_{m=0}^{M-1} \lambda_m \frac{\partial v'}{\partial U_m} U_m - \sum_{m=0}^{M-1} v_m G'_m = \text{Res}(\tilde{v}, \tilde{G}), \quad (2.9)$$

often called the *homological equation*⁵. Interpret the factor $(\partial v' / \partial U_m) U_m$ in the Calculus of Variations sense that it represents $v'_{U_m} U_m + v'_{U_{m,x}} U_{m,x} + v'_{U_{m,xx}} U_{m,xx} + \dots$ where these subscript-derivatives of v' are done with respect to the subscript symbol (Roberts 1988). The variation from the usual cell-problem arises in this systematic invariant manifold framework through accounting for physical out-of-equilibrium effects. Then update the approximations, and iterate until the residual $\text{Res}(\tilde{v}, \tilde{G})$ is of the order of the desired error.

2.2.4 Analogy with machine learning

We draw an analogy between this iteration and a machine learning algorithm where an AI learns the generic form of the macroscale evolution from many thousands of simulations, as reviewed by Frank et al. (2020), Sanderse et al. (2024). An example is the machine learning of bi-continuum models for a class of porous media flows by Wanga et al. (2024). Here, in constructing an invariant manifold M -continuum homogenisation, each iteration is analogous to one layer in a deep neural network: evaluating $\text{Res}(\tilde{v}, \tilde{g})$ is a physics-informed analogue to a nonlinear neurone function; and the linear corrections v', g' from the forced cell-problem (2.7) is a physics-informed analogue to using weighted linear combinations of outputs (i.e., activation functions) of one layer as the inputs of the next layer. Being algebraic, the ‘data’ which directs the updates encompasses all points in the state space’s domain, whereas in machine learning only a finite number of simulated data points are available. Consequently, we contend that mathematicians have for many decades been doing smart physics-informed analogues of machine learning. Such algebraic learning empowers the verification, validation, and physical interpretation that is required by modern science (e.g. Brenner & Koumoutsakos 2021).

⁵(e.g., Potzsche & Rasmussen 2006, Roberts 2015b, Siettos & Russo 2021, Martin et al. 2022)

Fish et al. (2021) [p.782] comments that “Approaches that combine machine learning with physics-based multiscale models are anticipated to accelerate materials discovery in the upcoming era of materials informatics.” I contend that with modern developments in mathematical theory combined with practical construction, ‘algebraic learning’ based upon real physics has many benefits over what could be obtained with machine learning.

3 An example three-mode, tri-continuum, homogenization

It is convenient in this first example to consider the heterogeneity κ in a homotopy from the simple case of constant, homogeneous κ . Let’s consider the case of homogenising the embedding PDE (2.1) in the family with heterogeneity $\kappa(x) := \kappa_1 / (1 + a \cos[2\pi x / \ell])$ over non-dimensional parameters a , $|a| < 1$. Let’s also focus on the diffusive case, $\alpha = 1$.

To most easily account for the microscale physics we non-dimensionalise on the microscale heterogeneity length scale ℓ such that $\kappa(x)$ is 2π -periodic in x . The non-dimensional domain length L is to be relatively large compared to the microscale length 2π . We also non-dimensionalise time so that $\kappa_1 = 1$. Hence we address the specific family of heterogeneity

$$\kappa(\theta) := 1 / (1 + a \cos \theta) \quad (3.1)$$

(the computer algebra of [Appendix A](#) works for a wide variety of 2π -periodic heterogeneity provided that $\kappa(\theta) = 1$ when $a = 0$). The key advantage of this parametrised heterogeneity is that we access in straightforward algebra non-trivial heterogeneity, $a \neq 0$, as a regular perturbation from the homogeneous case $a = 0$.

For the base case ($a = 0$) of constant $\kappa = 1$, the spectrum of the cell problem (2.6) is the eigenvalues $-n^2$ for $n = 0, 1, 2, \dots$, that is, the spectrum is $\{0, -1, -4, -9, \dots\}$. Corresponding complete and orthogonal eigenvectors are $\cos n\theta$ for $n \geq 0$ and $\sin n\theta$ for $n \geq 1$. Hence the eigenvalues for $n \geq 1$ are of multiplicity two. By continuity in the self-adjoint cell problem (2.6), for at least a finite range of heterogeneity $a \neq 0$, the spectrum is similar.

Here we choose to form a three-mode tri-continuum homogenisation by choosing to resolve modes corresponding to eigenvalues $\lambda_0 = 0$ and $\lambda_1 = \lambda_2 = -1$. Modes with eigenvalues $\leq \lambda_3 = -4$ are slaved. The spectral gap $(-1, -4)$ between λ_2 and λ_3 caters for the perturbing heterogeneity and perturbing x -gradients of \mathbf{u} .⁶

⁶In nonlinear problems, the spectral gap also caters for the perturbing nonlinearity.

This choice resolves the dynamics of the three sub-cell modes $1, \sin \theta, \cos \theta$ where the latter two correspond to physical sub-cell structures respectively out-of-phase and in-phase with the material heterogeneity. In the diffusive case, $\alpha = 1$, the slowest transient modes decay roughly like e^{-4t} , corresponding to the sub-cell modes $\cos 2\theta, \sin 2\theta$, and hence such a three-mode homogenisation is emergent on times $> 1/4$ (roughly). I use the term ‘roughly’ because the precise rates and times depend smoothly upon heterogeneity parameter a from these values obtained for $a = 0$. The shorter time for emergence is an improvement when compared to the classic homogenised PDE (2.2) which emerges on times > 1 .

3.1 Iteration systematically constructs

To construct approximations systematically, the computer algebra code of [Appendix A](#) repeatedly computes the residual, which then drives corrections, until the residual is zero to the specified order $N + 1$ of error. Theory then assures us the slow manifold is approximated to the same order of error ([Potsche & Rasmussen 2006](#), [Roberts 2015a](#)). The code of [Appendix A](#) constructs multi-continuum, multi-mode, micromorphic homogenisations for any (odd) number of modes M , but here we only discuss the case of $M = 3$ modes.

Iteration begins from the linear invariant subspace description that

$$\mathbf{u} \approx U_0 + U_1 \sin \theta + U_2 \cos \theta, \quad U_{0t} \approx 0, \quad U_{1t} \approx -U_1, \quad U_{2t} \approx -U_2.$$

Then the homological equation (2.9) for corrections, $\mathbf{u} \mapsto \mathbf{u} + v'$ and evolution $G \mapsto G + G'$, becomes

$$\frac{\partial^2 v'}{\partial \theta^2} + \left(\frac{\partial v'}{\partial U_1} U_1 + \frac{\partial v'}{\partial U_2} U_2 \right) - (G'_0 + G'_1 \sin \theta + G'_2 \cos \theta) = \text{Res}. \quad (3.2)$$

Then, in a couple of iterations [Appendix A](#) iteratively constructs the following three-mode invariant manifold to an example low-order of error ($N = 1$),

$$\begin{aligned} \mathbf{u} = & U_0 + U_1 \left[\sin \theta + \frac{1}{3} a \sin 2\theta \right] + U_2 \left[\cos \theta + \frac{1}{3} a \cos 2\theta \right] \\ & - \frac{5}{18} a U_{1x} \cos 2\theta + \frac{5}{18} a U_{2x} \sin 2\theta + \mathcal{O}(\partial_x^2, a^2). \end{aligned} \quad (3.3)$$

I define that $\mathcal{O}(\phi, \psi)$ means $\mathcal{O}(\phi) + \mathcal{O}(\psi)$, and recall that $\mathcal{O}(\partial_x^p)$ is to mean of the order of the corresponding remainder term from theory, such as expression (23) by [Roberts \(2015a\)](#) for $N = p - 1$. The manifold (3.3) illustrates that the invariant manifold framework systematically discovers both that the heterogeneity (3.1) physically modifies the sub-cell mode shapes to $\sin \theta + (a/3) \sin 2\theta + \mathcal{O}(a^2)$ and $\cos \theta + (a/3) \cos 2\theta + \mathcal{O}(a^2)$, and also discovers the effects on the sub-cell physics of macroscale spatial gradients via the terms involving U_{1x}, U_{2x} . Higher-order corrections systematically resolve more multiscale physical effects and interactions.

To the next order of error, $\mathcal{O}(\partial_x^3, a^3)$ ($N = 2$), the methodology discovers that the evolution on this invariant manifold is the coupled set of three macroscale PDEs

$$U_{0t} = -\frac{1}{2}aU_{1x} + \left(1 + \frac{1}{2}a^2\right)U_{0xx} - \frac{1}{2}aU_{2xx} + \mathcal{O}(\partial_x^3, a^3), \quad (3.4a)$$

$$U_{1t} = -\left(1 + \frac{5}{12}a^2\right)U_1 + aU_{0x} - \left(2 + \frac{2}{9}a^2\right)U_{2x} \\ + \left(1 - \frac{17}{54}a^2\right)U_{1xx} + \mathcal{O}(\partial_x^3, a^3), \quad (3.4b)$$

$$U_{2t} = -\left(1 - \frac{1}{12}a^2\right)U_2 + \left(2 + \frac{2}{9}a^2\right)U_{1x} \\ - aU_{0xx} + \left(1 + \frac{5}{27}a^2\right)U_{2xx} + \mathcal{O}(\partial_x^3, a^3). \quad (3.4c)$$

These PDEs form a rigorous second-order tri-continuum, three-mode, homogenised model for the heterogeneous system (2.1) with heterogeneity (3.1). Physically, (3.4b) shows that gradients U_{0x} of the mean mode predominantly create out-of-phase microscale structures, U_1 , that then affect the macroscale effective diffusivity of the mean mode via (3.4a).

This section discusses parametrising the homogenisation directly in terms of the amplitudes U_0, U_1, U_2 of the microscale sub-cell modes, here $1, \sin \theta, \cos \theta$. This parametrisation is straightforward to do because these are the microscale eigenfunctions. However, the invariant manifold framework potentially empowers us to parametrise the modelling almost arbitrarily (Roberts 2015b, §5.3, e.g.). For example, in shear dispersion (see Example 4 in the general theory of Section 5) Roberts & Struin (2004) showed how to transform an invariant manifold analysis *from a two-mode model to two zone model* either via transforming the derived modal equations [§2], or via defining two coupled zones at the outset and deriving the interaction between and within the two zones in terms of the means in each zone [§3]. The same could be done here for homogenisation. Alternatively, one could *adaptively modify* the definition of the amplitudes to simplify the algebraic form (3.4) of the evolution on the invariant manifold—a *normal form* of the model (e.g., Arneodo et al. 1985). But such adaptive modification is often unphysical and usually quite tedious. The crucial point throughout is that although the definition of amplitudes may differ, one preserves the same physical sub-cell modes v_0, \dots, v_{M-1} to detail the microscale structures (the multiscale lifting). Alavi et al. (2023) [p.2166] commented that “proper elaboration of the macroscopic kinematic and static quantities that pertain to the micromorphic continuum is a problematic issue”. In contrast, in our dynamical system framework there is no problematic issue: this paragraph indicates how the precise physical meaning of the variables used to parametrise a multi-modal, multi-continuum, model need be only mildly constrained by the physics of the problem and so is largely a subjective aesthetic decision.

3.2 High-order three-mode homogenization

With the computer algebra of [Appendix A](#) we easily construct multi-modal homogenisations, such as (3.4), to high-order. In this linear class of problems we use the high-order models to quantitatively estimate limits of approximate homogenisations such as (3.4).

3.2.1 Convergence in heterogeneity a

Recall that in this example the heterogeneity (3.1), $\kappa = 1/(1 + a \cos \theta)$, has strength parametrised by a . Let's first explore the series in a .

Let's construct the multi-modal homogenisation to low order in spatial gradient, errors $\mathcal{O}(\partial_x^3)$, but here to high-order error $\mathcal{O}(a^{31})$ in heterogeneity. The code takes less than three minutes to execute. I chose three important coefficients in the extension to model (3.4):

- coefficient of U_{0xx} in U_{0t} that starts $1 + \frac{1}{2}a^2 + \frac{5}{24}a^4 \dots$;
- coefficient of U_1 in U_{1t} that starts $-1 - \frac{5}{12}a^2 - \frac{437}{3456}a^4 + \dots$;
- coefficient of U_2 in U_{2t} that starts $-1 + \frac{1}{12}a^2 - \frac{53}{3456}a^4 + \dots$.

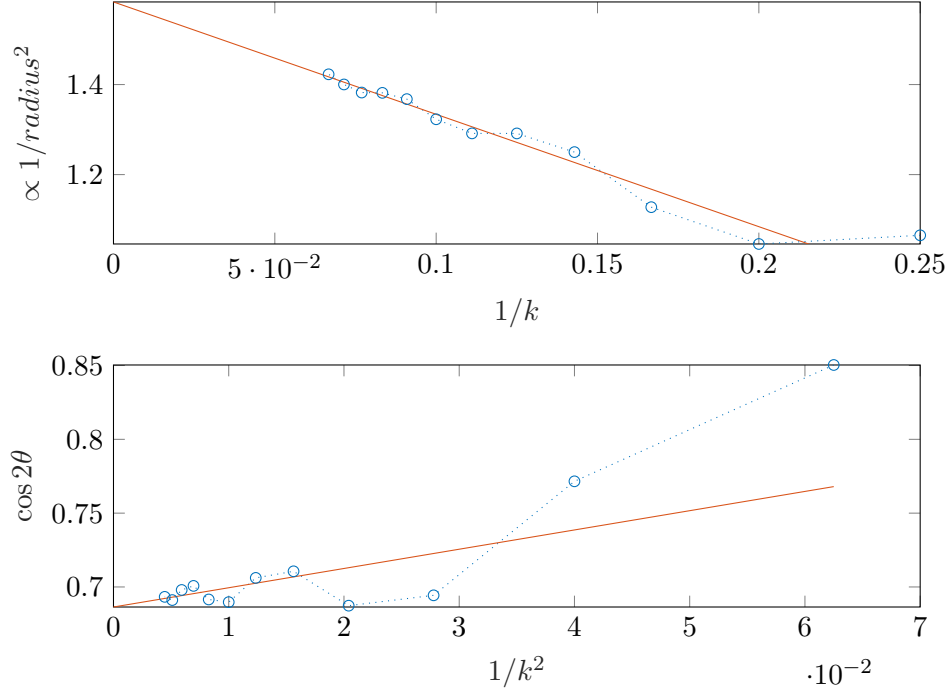
[Figure 2](#) shows a Mercer–Roberts plot for the coefficient of U_1 in U_{1t} , the plot for the coefficient of U_{0xx} in U_{0t} is almost the same. A simpler Domb–Sykes plot suffices for the other series ([Domb & Sykes 1957](#), [Hunter 1987](#), e.g.). Such plots predict the radius of convergence limiting singularity in heterogeneity a as 1.21, 1.21, 1.57, respectively, due to singularities in the complex a -plane at respective angles 23° , 23° , 90° to the real- a axis. Remarkably, the predicted radius of convergence 1.21 indicates that we may use the three-mode homogenisation model even up to the extreme contrast heterogeneity of $a \rightarrow 1$.

Practically, the radius of convergence indicates that via expansion to errors $\mathcal{O}(a^{11})$ one would compute coefficients to four decimal places over the range $|a| < 1/2$. Further exploration indicates that the [6, 6] Padé approximations in a appear to be similarly accurate over the range $|a| \leq 1$.

3.2.2 Convergence in spatial wavenumber

Recall that traditional mathematical proofs of homogenisation require the scale separation limit that the length-scale ratio $\ell/L \rightarrow 0$. In practice, engineers and scientists presume that $\ell/L < 0.1$ or 0.01 is sufficient. For example, [Somnic & Jo \(2022\)](#) comments [p.4] “For a periodic network of lattices to be considered as material, the characteristic length of its cells needs to be at least one or two orders of magnitude below the medium’s

Figure 2: Mercer & Roberts (1990) [Appendix] plot for the series in heterogeneity a of the coefficient of U_1 in a high-order extension of (3.4b) for U_{1t} . The extrapolated intercepts to $1/k = 0$ predict the location of convergence limiting singularities in the complex a -plane.



overall length scale.” By exploring the modal evolution (3.4) to high-order in spatial gradients ∂_x , albeit to low-order in heterogeneity a , we here quantify the range of valid scale ratios ℓ/L .

Choosing errors $\mathcal{O}(a^4)$, amazingly we find the evolution effectively truncates. The computer algebra derives the invariant manifold evolution to $\mathcal{O}(\partial_x^{31}, a^4)$ in just a few seconds. After a spatial Fourier transform to wavenumber k , some Domb–Sykes plots in powers of wavenumber k of the a^2, a^3 terms then shows all are limited by simple pole singularities at wavenumber $k = \pm 3/2$.

A first consequence is that these Domb–Sykes plots show that for small heterogeneity the tri-continuum modelling resolves all wavenumbers $|k| < 3/2$; that is, all wavelengths bigger than $4\pi/3 = 2\ell/3$. That is, potentially the resolved macroscales are all wavelengths bigger than just $2/3$ of the microscale periodicity! However, a practical lower bound may be about twice this. Moreover, be aware that higher orders in heterogeneity a appear to be more restrictive (Roberts 2024).

A second consequence is that the tri-continuum, three-mode, homogenisation algebraically simplifies using the nonlocal operator $\mathcal{D} := (1 + 4/9 \partial_x^2)^{-1}$. [Appendix A](#) finds the following to arbitrarily high order in ∂_x :

$$\begin{aligned} U_{0t} = & (1 + \frac{1}{2}a^2)U_{0xx} - \frac{1}{2}aU_{1x} - \frac{1}{2}aU_{2xx} - \frac{1}{72}a^3\mathcal{D}(15\partial_x + 11\partial_x^3 + 3\partial_x^5)U_1 \\ & - \frac{1}{72}a^3\mathcal{D}(11\partial_x^2 + 5\partial_x^4)U_2 + \mathcal{O}(a^4), \end{aligned} \quad (3.5a)$$

$$\begin{aligned} U_{1t} = & -U_1 - 2U_{2x} + aU_{0x} + U_{1xx} - \frac{1}{36}a^2\mathcal{D}(15 + 18\partial_x^2 + 5\partial_x^4)U_1 \\ & - \frac{1}{18}a^2\mathcal{D}(4\partial_x + 4\partial_x^3 + \partial_x^5)U_2 + \frac{1}{144}a^3\mathcal{D}(60\partial_x + 56\partial_x^3 + 13\partial_x^5)U_0 \\ & + \mathcal{O}(a^4), \end{aligned} \quad (3.5b)$$

$$\begin{aligned} U_{2t} = & -U_2 + 2U_{1x} - aU_{0xx} + U_{2xx} + \frac{1}{36}a^2\mathcal{D}(3 + 8\partial_x^2 + 3\partial_x^4)U_2 \\ & + \frac{1}{18}a^2\mathcal{D}(4\partial_x + 4\partial_x^3 + \partial_x^5)U_1 - \frac{1}{72}a^3\mathcal{D}(22\partial_x^2 + 12\partial_x^4 + \partial_x^6)U_0 \\ & + \mathcal{O}(a^4), \end{aligned} \quad (3.5c)$$

Through the nonlocal \mathcal{D} , such an model is an example of a nonlocal homogenisation (e.g., [Bažant & Jirásek 2002](#)).

Effects of higher order than cubic in a have yet to be explored in detail. However, plots like [Figure 2](#) for terms a^4 in heterogeneity indicate convergence limiting singularities at wavenumber $k = \pm 1/2$. That is, although for small a we can get the above ‘exact’ nonlocal model, at finite heterogeneity a singularities limit the homogenisation to macroscales longer than twice the length ℓ of the microscale period, as also found by [Roberts \(2024\)](#) for one-mode homogenisation. Thus, more generally, the high-order homogenisation is valid for macroscale $L > 2\ell$, equivalently, it is valid for scale ratios $\ell/L < 0.5$ (although a practical bound might be a half of this), which is significantly better than the “one or two orders of magnitude” usually assumed.

3.3 Homogenise heterogeneous nonlinearity

Homogenising nonlinear heterogeneous systems requires just a few straightforward modifications. [Section 5](#) establishes its theoretical support. Here consider constructing a one-mode homogenisation of the heterogeneous diffusion [\(2.1\)](#) with the addition of nonlinear advection, namely

$$\frac{\partial u}{\partial t} = \frac{\partial}{\partial x} \left\{ \kappa(x) \frac{\partial u}{\partial x} - \gamma \eta(x) u^2 / 2 \right\}, \quad 0 < x < L. \quad (3.6)$$

This is a Burgers’ PDE with nonlinearity strength parametrised by γ , and heterogeneous coefficient in both the diffusion and nonlinear advection term, $\kappa(x)$ and $\eta(x)$ respectively. Let’s non-dimensionalise on the microscale length ℓ so that the heterogeneities $\kappa(x)$ and $\eta(x)$ are 2π -periodic: specifically

$$\kappa(\theta) := 1/(1 + a \cos \theta), \quad \eta(\theta) := c_1 \cos \theta + c_2 \sin 2\theta. \quad (3.7)$$

The corresponding phase-shift embedding modifies PDE (2.4) to the nonlinear

$$\frac{\partial \mathbf{u}}{\partial t} = \left(\frac{\partial}{\partial x} + \frac{\partial}{\partial \theta} \right) \left\{ \kappa(\theta) \left(\frac{\partial \mathbf{u}}{\partial x} + \frac{\partial \mathbf{u}}{\partial \theta} \right) - \gamma \eta(\theta) \mathbf{u}^2 / 2 \right\}, \quad (3.8)$$

for fields \mathbf{u} being 2π -periodic in θ . As an example, we construct the one-mode invariant manifold homogenisation ($M = 1$) of this embedding PDE. The accessible class of manifolds is to construct homogenisations as a regular perturbation in nonlinearity parameter γ . There are just three necessary changes in the computer algebra of Appendix A: firstly, truncating to some specified order of error in γ , here choose errors $\mathcal{O}(\gamma^2)$; secondly, specifying the extra heterogeneity $\eta(\theta)$; and thirdly, modifying the computation of the residual by including the additional term $-\gamma \eta(\theta) \mathbf{u}^2 / 2$ in the flux.

Executing the code of Appendix A constructs the one-mode homogenisation and finds that the invariant manifold ensemble field (to low-order)

$$\begin{aligned} \mathbf{u} = & U_0 + a \sin \theta U_{0x} + \gamma c_1 \left(\frac{1}{2} \sin \theta + \frac{1}{8} a \sin 2\theta \right) U_0^2 \\ & - \gamma c_2 \left(\frac{1}{4} a \cos \theta + \frac{1}{4} \cos 2\theta + \frac{1}{12} a \cos 3\theta \right) U_0^2 + \mathcal{O}(\gamma^2 + \partial_x^2, a^2). \end{aligned} \quad (3.9a)$$

Simultaneously the code constructs that the evolution on the invariant manifold obeys the homogenised PDE

$$U_{0t} = U_{0xx} - \frac{1}{4} \gamma \partial_x (c_1 a U_0^2 + c_2 a^2 U_0 U_{0x}) + \mathcal{O}(\gamma^2, \partial_x^3, a^3). \quad (3.9b)$$

Although the microscale nonlinear advection coefficient has coefficient with zero-mean, $\overline{\eta(\theta)} = 0$, nonetheless the interaction of the two heterogeneities (3.7) generates a non-zero effective nonlinear advection $\approx -\frac{1}{2} \gamma c_1 a U_0 U_{0x}$.

4 An example of high-contrast multi-continuum homogenisation

The modelling of materials with so-called *high contrast* is of interest (e.g., Leung 2024, Efendiev & Leung 2023, Chen et al. 2023). This section considers the specific example of the multiscale embedding PDE (2.1) with a *high-contrast*, ℓ -periodic, heterogeneous coefficient $\kappa(x)$. Specifically, in each microscale period, the coefficient $\kappa(x) = \kappa_1$ constant for most x , except in a thin near-insulating layer of width $\eta \ll \ell$ where the coefficient $\kappa(x) = \kappa_0 \ll \kappa_1$. We focus on modelling interesting dynamics in the interior \mathbb{X} of the relatively large 1-D spatial domain $[0, L]$.

This section shows how the novel and powerful invariant manifold framework of Section 2 establishes rigorous multi-mode multi-continuum homogenisations of the high-contrast material. For example, Section 4.3 addresses the bi-continuum case and derives the homogenised model in terms of two

physics-informed macroscale quantities U_0, U_1 that evolve according to two coupled macroscale PDEs of the form, non-dimensionalised,

$$\partial_t^\alpha U_0 = 0.81U_{0xx} + 0.36U_{1x} + \dots, \quad \partial_t^\alpha U_1 = -0.46U_1 - 0.36U_{0x} + \dots, \quad (4.1)$$

where here the numerical coefficients are for a specific high-contrast case in the class defined above, and for both $\alpha = 1, 2$.

Because our sound modelling is transitive, the corresponding classic homogenised one-mode macroscale PDE (2.2) may be recovered by the adiabatic quasi-equilibrium approximation of the second mode in (4.1) that gives $U_1 \approx -0.77U_{0x}$. Thence the first PDE of (4.1) reduces quantitatively to the usual homogenised macroscale PDE $\partial_t^\alpha U_0 \approx 0.54U_{0xx}$.

Extensions to more than two modes are straightforward: for example, Section 4.4 derives a tri-continuum model. Indeed the number M of modes is coded as a parameter in the computer algebra code of Appendix B.

As introduced in Section 2, and detailed in Section 5.2, the theoretical support for such homogenisation depends upon the time operator ∂_t^α . For the diffusive case, $\alpha = 1$, the homogenised models are known to generally be exponentially quickly emergent. For the wave case, $\alpha = 2$, the homogenised models are best viewed as a guiding centre for the dynamics. In all cases, backwards theory (adapted from Roberts 2022, Hochs & Roberts 2019) would assert that there is a system close to the specified PDE (2.1) that has the precise constructed invariant manifold and associated homogenisation, such as (4.1).

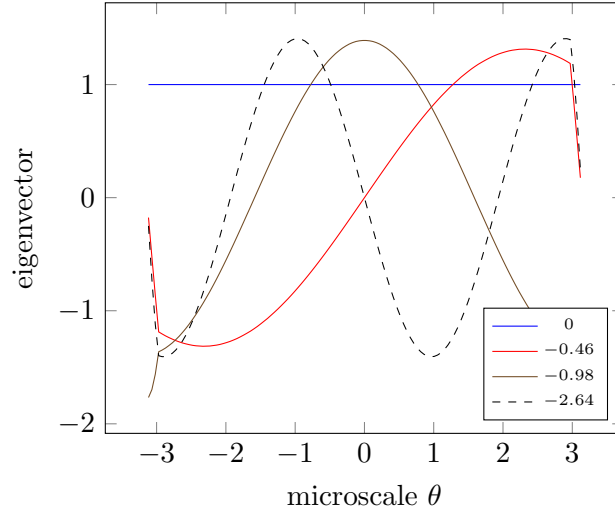
Recall that the approach here makes rigorous progress through considering the ensemble of all phase-shifts by solving the PDE (2.4) in the ‘cylindrical’ domain $\mathbb{D} := \{(x, \theta) : x \in \mathbb{X}, \theta \in [-\ell/2, \ell/2]\}$, and with ℓ -periodic boundary conditions in θ . Section 2.1 established that solutions of (2.4) provide us with solutions to the heterogeneous PDE (2.1).

To establish the basis of an invariant manifold homogenisation, recall that we consider the embedding PDE (2.4) with $\partial/\partial x$ neglected, and solved with ℓ -periodic boundary conditions. This describes the basic physical sub-cell dynamics. Because the PDE is linear, it is sufficient to consider the dynamics about the zero equilibrium, which we do henceforth.

4.1 Spectrum at each equilibrium

The approach is to choose invariant manifold models (Roberts 2015a) based upon the sub-cell physics encoded in the spectrum of the cell problem (2.6), and to choose depending upon required macroscale aspects.

Figure 3: an example of the leading four eigenfunctions of the cell-problem (2.6), and corresponding eigenvalues, for a high-contrast heterogeneity. For the non-dimensional case of $\ell = 2\pi$, $\kappa_1 = 1$, and a thin insulating layer $\eta/\ell = 0.06$ located at $\theta = \pm\pi$ of insulation, $\kappa_0 = 0.06$ ($\chi = 1$).



The spectrum of the cell problem is in turn determined from the eigenvalues of the operator on the right-hand side of the cell-problem (2.6) with its ℓ -periodic boundary conditions. Say the eigenvalues are $\lambda_0 = 0 \geq \lambda_1 \geq \lambda_2 \geq \dots$ with corresponding eigenfunctions $v_0(\theta)$, $v_1(\theta)$, $v_2(\theta)$, \dots , such as the example eigenfunctions drawn in Figure 3. Consequently, the two common cases of the cell problem are the following two:

- for diffusion, $\alpha = 1$, the modal solutions of the cell problem (2.6) are that $u \propto e^{\lambda_m t}$ for eigenvalues $0, \lambda_1, \lambda_2, \dots$;
- whereas for waves, $\alpha = 2$, the modal solutions of the cell problem (2.6) are that $u \propto e^{\pm i\omega_m t}$ for frequencies $\omega_m := \sqrt{-\lambda_m}$;
- and the modal solutions are otherwise for other time evolution operators ∂_t^α (e.g., Section 5.2.4).

Generally we choose to focus on, that is model, the sub-cell modes associated with the small magnitude eigenvalues because these are either the *emergent* sub-cell modes, $\alpha = 1$, or the *guiding centre* sub-cell modes, $\alpha = 2$ (e.g., van Kampen 1985), respectively.

For the specific example leading to the model (4.1), the non-dimensional spectrum for diffusion is $\lambda_m \kappa_1 4\pi^2/\ell^2 \in \{0, -0.46, -0.98, \dots\}$, whereas the non-dimensional frequencies for waves are $\sqrt{\lambda_m \kappa_1} 2\pi/\ell \in \{0, \pm i 0.68, \pm i 0.99, \dots\}$ (the zero frequency has multiplicity two). The model PDE (4.1) is constructed by forming the approximate invariant manifold based upon the two/four slowest modes (blue and red eigenfunctions in the example of Figure 3) corresponding to non-dimensional cell-problem (2.7) diffusive eigenvalues $\{0, -0.46\}$ or wave frequencies $\{0, \pm i 0.68\}$, respectively.

Recall from [Section 2.2.1](#) that a rational approach to forming multi-continuum models is then to decide what time-scales you need to resolve in the problem at hand, and then chose the number of leading modes whose eigenvalues/frequencies match or are slower than that of the needed time-scale. These leading modes then form the multi-continuum, or micromorphic, model.

For these spatio-temporal systems there is additionally the issue of spatial resolution. High-order approximations can indicate a quantitative limit to the spatial resolution as in [Section 3.2.2](#) (e.g., [Mercer & Roberts 1994](#), [Watt & Roberts 1995](#)). A guiding ‘rule-with-exceptions’ is that the more the number of modes forming the invariant manifold then the shorter the resolved length scales of the multi-mode model. This issue was extensively discussed for shear dispersion by [Watt & Roberts \(1995\)](#) [§§2.1, 2.3, 3.4, 4.1]. Nonetheless, such high-order evidence is only a guide: since we mostly use low-order models, the practical issue is primarily whether a chosen low-order has adequate spatial resolution for the purposes at hand. The quantitative error estimate by equation (23) of [Roberts \(2015a\)](#) is potentially more useful for such low-order modelling.

4.1.1 High-contrast thin layer

To homogenise the high contrast problem we need to determine the spectrum of the eigen-problem (2.7). We first analytically approximate the eigenvalue spectrum in cases when a layer of near ‘insulator’ is so thin that we can replace it by a ‘jump’ condition (as suggested by the example eigenfunctions of [Figure 3](#)). These analytic approximations *guide* subsequent numerical-algebraic construction and interpretation. We deduces that eigenvalues are $\lambda_m \approx -m^2 \kappa_1 \pi^2 / \ell^2$ corresponding to eigenfunctions, over the cell $\theta \in (-\ell/2, +\ell/2)$, of $v_m \approx \cos(m\pi\theta/\ell)$ for even $m = 0, 2, 4, \dots$, and, with a ‘jump’ across the layer at $\theta = \pm\ell/2$, of $v_m \approx \sin(m\pi\theta/\ell)$ for odd $m = 1, 3, 5, \dots$.

We seek solutions to the eigen-problem (2.7) for the right-hand side operator. That is, we find ℓ -periodic solutions to

$$\kappa_1 v_{\theta\theta} = \lambda v \text{ on } (-\ell/2, \ell/2), \quad \text{except in a layer where } \kappa_0 v_{\theta\theta} = \lambda v,$$

for an ‘insulating’ layer of small thickness η and where $\kappa_0 = \mathcal{O}(\eta)$. We know all eigenvalues $\lambda \leq 0$.

Thin insulating layer Here derive jump conditions across the thin layer. For algebraic simplicity, *temporarily* set the origin of θ at the centre of the thin layer so the layer is the interval $(-\eta/2, +\eta/2)$.

Within the thin layer an eigenfunction is of the form $v = C \cos(\sqrt{-\lambda/\kappa_0}\theta) + D \sin(\sqrt{-\lambda/\kappa_0}\theta)$. Define

$$\begin{aligned} [v] &:= v_{\eta/2} - v_{-\eta/2} = 2D \sin(\sqrt{-\lambda/\kappa_0}\eta/2) = D\sqrt{-\lambda/\kappa_0}\eta + \mathcal{O}(\eta^{3/2}); \\ \bar{v} &:= \frac{1}{2}(v_{\eta/2} + v_{-\eta/2}) = C \cos(\sqrt{-\lambda/\kappa_0}\eta/2) = C + \mathcal{O}(\eta). \end{aligned}$$

Hence $C \approx \bar{v} = \mathcal{O}(1)$ and $D \approx [v]/(\sqrt{-\lambda/\kappa_0}\eta) = \mathcal{O}(\eta^{-1/2})$. Then within the layer the derivative

$$\begin{aligned} v_\theta &= -\sqrt{-\lambda/\kappa_0}C \sin(\sqrt{-\lambda/\kappa_0}\theta) + \sqrt{-\lambda/\kappa_0}D \cos(\sqrt{-\lambda/\kappa_0}\theta) \\ &\approx -\sqrt{-\lambda/\kappa_0}\bar{v} \sin(\sqrt{-\lambda/\kappa_0}\theta) + ([v]/\eta) \cos(\sqrt{-\lambda/\kappa_0}\theta). \end{aligned}$$

So the jump and the mean of the derivative are

$$\begin{aligned} [v_\theta] &\approx -2\sqrt{-\lambda/\kappa_0}\bar{v} \sin(\sqrt{-\lambda/\kappa_0}\eta/2) \approx (\lambda\eta/\kappa_0)\bar{v}, \\ \bar{v}_\theta &\approx ([v]/\eta) \cos(\sqrt{-\lambda/\kappa_0}\eta/2) \approx [v]/\eta. \end{aligned}$$

Outside the layer The eigenfunctions $v(\theta)$ are to be continuous so the jump $[v]$ and mean \bar{v} are the same inside and outside the layer. And the flux has to be continuous across the layer boundary, that is $\kappa_1 v_\theta^{\text{outside}} = \kappa_0 v_\theta^{\text{inside}}$. Hence outside the layer we have the conditions

$$[v_\theta] = [(\kappa_0/\kappa_1)v_\theta^{\text{inside}}] \approx (\lambda\eta/\kappa_1)\bar{v}, \quad (4.2a)$$

$$\bar{v}_\theta = (\kappa_0/\kappa_1)v_\theta^{\text{inside}} \approx \kappa_0/(\kappa_1\eta)[v] = 1/(\chi\ell)[v] \quad (4.2b)$$

as we choose to scale κ_0 so that $\kappa_0/\kappa_1 = \eta/(\chi\ell)$ for some insulating parameter χ . That is, the layer diffusivity/elasticity $\kappa_0 \propto \eta\kappa_1$ decreases with the relative layer thickness η/ℓ . Thus small η characterises a high-contrast material. Parameter χ characterises the strength of the ‘insulation’ in the thin layer: larger is more insulating, whereas smaller is less so.

For algebraic simplicity we now reset the origin of θ so that the thin layer is at $\theta = \pm\ell/2$, and hence a jump across the thin layer is hereafter $[v] = v_{-\ell/2} - v_{+\ell/2}$.

There are two families of eigenfunctions and eigenvalues.

- The symmetric family is eigenfunctions $v = \cos k\theta$ for eigenvalue $\lambda = -\kappa_1 k^2$ for some wavenumbers k to be determined. For this eigenfunction

$$\bar{v} = \cos(k\ell/2), \quad [v] = 0, \quad \bar{v}_\theta = 0, \quad [v_\theta] = 2k \sin(k\ell/2).\lambda$$

Hence (4.2b) is satisfied, whereas (4.2a) requires that $2k \sin(k\ell/2) = -k^2\eta \cos(k\ell/2)$, that is, $2k \tan(k\ell/2) = -k^2\eta \rightarrow 0$ as $\eta \rightarrow 0$. Hence these eigenfunctions occur for wavenumber $k = m\pi/\ell$ for even integer m . That is, $v_m = \cos(m\pi\theta/\ell)$ and corresponding eigenvalues

Table 1: first two \mathfrak{K} -values that solve $\tan \mathfrak{K} = -\chi \mathfrak{K}$ for four values of insulation strength χ . Below are the leading four eigenvalues for the non-dimensional case of $\kappa_1 = 1$ and $\ell = 2\pi$: these approximate the eigenvalues for small insulation layer width η .

χ	1/3	1	3	9
\mathfrak{K}_1	2.46	2.03	1.74	1.63
\mathfrak{K}_3	5.23	4.91	4.78	4.74
λ_0	0	0	0	0
λ_1	-0.61	-0.42	-0.31	-0.27
λ_2	-1	-1	-1	-1
λ_3	-2.77	-2.45	-2.32	-2.27

$\lambda_m = -\kappa_1 \pi^2 m^2 / \ell^2$ for $m = 0, 2, 4, \dots$. [Table 1](#) list the first two of these eigenvalues, λ_0, λ_2 , for four selected parameters χ of thin insulation layer width η .

- The asymmetric family is eigenfunctions of the form $v = \sin k\theta$ for eigenvalue $\lambda = -\kappa_1 k^2$ for some wavenumbers k to be determined. For this eigenfunction

$$\bar{v} = 0, \quad [v] = -2 \sin(k\ell/2), \quad \bar{v}_\theta = k \cos(k\ell/2), \quad [v_\theta] = 0.$$

Hence [\(4.2a\)](#) is satisfied, whereas [\(4.2b\)](#) requires that $k \cos(k\ell/2) = -2/(\chi\ell) \sin(k\ell/2)$,

$$\text{that is, } \tan(k\ell/2) = -\chi(k\ell/2). \quad (4.3)$$

For *odd* integer m , let \mathfrak{K}_m be the solutions of $\tan \mathfrak{K} = -\chi \mathfrak{K}$ in sequence so that $m\pi/2 < \mathfrak{K}_m \leq (m+1)\pi/2$. Then wavenumber $k = 2\mathfrak{K}_m/\ell$ satisfies [\(4.3\)](#) and so asymmetric eigenfunctions are $v_m = \sin(2\mathfrak{K}_m\theta/\ell)$ corresponding to eigenvalues $\lambda_m = -\kappa_1 4\mathfrak{K}_m^2/\ell^2$ for $m = 1, 3, \dots$ ⁷ [Table 1](#) list the first two of these eigenvalues, λ_1, λ_3 , for four selected parameters χ of thin insulation layer width η .

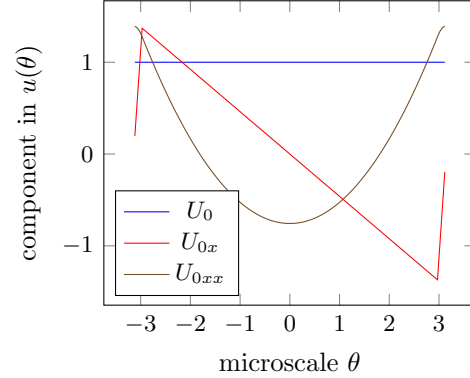
4.2 One-mode slow manifold model

One may construct a *slow manifold* model based upon the eigenvalue zero, here corresponding to the one sub-cell mode $v_0 = \cos 0\theta = 1$. Since v_0 is constant, such slow invariant manifold modelling gives the classic homogenised PDE [\(2.2\)](#), but generalised to higher-order derivatives at finite scale separation ([Roberts 2024](#)). In the diffusion case, $\alpha = 1$, the argument for its emergence as a valid model is that all other sub-cell modes decay exponentially quickly in time, the slowest of which is $\exp(-\kappa_1 4\mathfrak{K}_1^2 t / \ell^2)$.

Let's explore the non-dimensional case of $\kappa_1 = 1$ and $\ell = 2\pi$ ([Table 1](#)) with the specific insulating thin layer $\eta/\ell = \kappa_0 = 0.06$ (i.e., $\chi = 1$). All the cell-problems are solved numerical on a sub-cell grid with 128 points per

⁷Using $\tan \mathfrak{K} \approx 1/(\pi/2 - \mathfrak{K})$, gives $1/(\pi/2 - \mathfrak{K}_1) \approx -\chi \mathfrak{K}_1$ which leads to $\mathfrak{K}_1 \approx \frac{\pi}{2} + \frac{2}{\pi\chi}$. Similarly, $\mathfrak{K}_3 \approx \frac{3\pi}{2} + \frac{2}{3\pi\chi}$. These reproduce [Table 1](#) within errors 0.005–0.2 over $\chi \geq 1$.

Figure 4: the sub-cell structure of the one-mode slow manifold field (4.4a) in the high-contrast thin-layer problem. Specifically, this is the non-dimensional case of $\ell = 2\pi$, $\kappa_1 = 1$, and a thin insulating layer $\eta/\ell = 0.06$ located at $\theta = \pm\pi$ of insulation parameter $\chi = 1$ so $\kappa_0 = 0.06$.



cell. The numerically obtained leading non-zero eigenvalue is $\lambda_1 = -0.4597$, so in the diffusion case the decay to the slow manifold homogenisation is roughly like $e^{-0.46t}$, from any given initial condition. The computer algebra of [Appendix B](#), with modes $M = 1$, then seeks a slow manifold that satisfies the embedding PDE (2.4) (discretised in θ) to any specified order in ∂_x . The result is that the detailed slow manifold field is

$$u(t, x, \theta) = U_0 + u_1(\theta)U_{0x} + u_2(\theta)U_{0xx} + \mathcal{O}(\partial_x^3), \quad (4.4a)$$

in terms of the coefficient functions plotted in [Figure 4](#). For this high-contrast thin layer, the U_{0x} -component of [Figure 4](#) shows that x -gradients of the field lead to a sub-cell field where rapid spatial variation takes place in the thin insulating layer, as expected physically. The corresponding, but higher-order, homogenised evolution is determined to be

$$\frac{\partial^\alpha U_0}{\partial t^\alpha} = 0.5386 U_{0xx} + 0.3379 U_{0xxxx} - 0.9019 U_{0xxxxxx} + \mathcal{O}(\partial_x^7), \quad (4.4b)$$

that is, $K = 0.5386$ in the leading-order homogenised PDE (2.2). Higher-order models such as (4.4b) often need regularisation: for example, upon neglecting the sixth-order derivative, the model (4.4b) may be regularised to $(1 - 0.63\partial_x^2)\partial_t^\alpha U_0 \approx 0.54 U_{0xx}$ (to two decimal places). An alternative form of this regularised PDE is the nonlocal homogenisation $\partial_t^\alpha U_0 \approx 0.54 \mathcal{A} \star U_{0xx}$ in terms of the convolution kernel $\mathcal{A}(x) \propto \exp(-0.79|x|)$, a kernel which decays to zero on the heterogeneity length ℓ , here 2π . [Bažant & Jirásek \(2002\)](#) discussed how such nonlocal models may desirably capture small-scale effects, produce convergent numerical solutions, achieve regularisation, and capture size effects seen in experiments.

4.3 Two-mode, bi-continuum, homogenisations exist and emerge

A two-mode, invariant manifold, homogenisation may be constructed based upon the leading two eigenvalues. For definiteness we non-dimensionalise space-time so that cell-length $\ell = 2\pi$ and the coefficient $\kappa_1 = 1$, and also focus on the case of thin layer parameter $\chi = 1$, the second column of [Table 1](#).

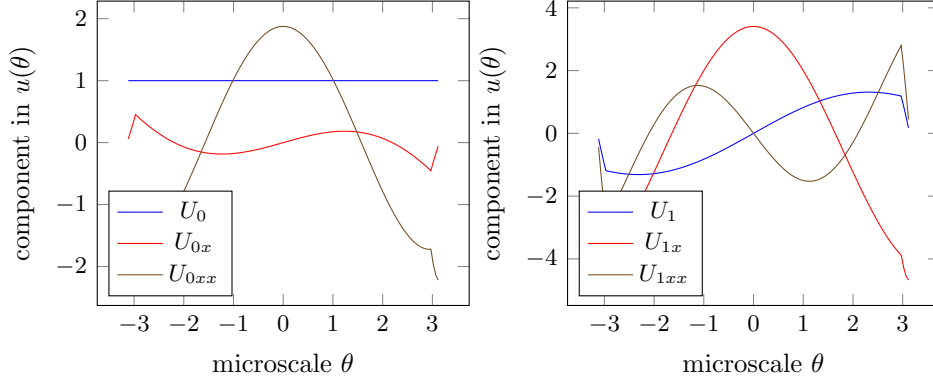
In this case the leading two eigenvalues are $\lambda_0 = 0$ and $\lambda_1 \approx -0.42$ corresponding to the two sub-cell modes $v_0 = 1$ and $v_1 \approx \sin(2.03\theta/\pi)$ (the two blue curves in the two panels of [Figure 5](#) are more precise). In the diffusion case, $\alpha = 1$, and since the next eigenvalue $\lambda_2 = -1$, such a two-mode model is emergent with the slowest transient decaying roughly like e^{-t} . The eigenvalue gap of $(-0.42, -1)$ caters for perturbing macroscale x -gradients.

To construct the invariant manifold homogenisation corresponding to these two modes we employ the algorithm summarised in [Section 2.2.3](#), and starting from the initial approximation that $\mathbf{u} \approx U_0 + U_1 v_1(\theta)$ such that $\partial_t^\alpha U_0 \approx 0$ and $\partial_t^\alpha U_1 \approx -0.42 U_1$. The computer algebra of [Appendix B](#) then iteratively corrects its approximations until the governing embedding PDE [\(2.4\)](#) has residual smaller than a specified order of error.

Here we modify in two ways the procedure that is introduced in [Section 2.2.3](#) and as implemented in the example of [Section 3.1](#). Firstly, previously we had introduced and implemented the procedure as if we could do all steps exactly in algebra. But for this high-contrast media we do not have exact algebraic expressions for the eigenfunctions ([Section 4.1.1](#)). Consequently, we adopt a simple sub-cell θ -space discretisation of the cell eigen-problem [\(2.7\)](#) and the corresponding homological equation [\(2.9\)](#). The computer algebra sets $n = 128$ points per period of sub-cell variable θ , and uses centred differences in θ , which should be fine enough to be faithful to the microscale differentials to about four significant digits. The macroscale variations in x, \mathbf{x} are still represented explicitly in algebra—there is no numerical approximation on the macroscale. [MacKenzie \(2005\)](#) first discussed such fine-grid numerics for constructing invariant manifolds of the macroscale dynamics of the 1-D and 2-D Kuramoto–Sivashinky PDE and the need for numerics in 2-D (see also [Roberts et al. 2014](#)). [Section 6](#) also uses such mixed numerics-algebra for multi-continuum homogenisation of 2-D elasticity.

The second modification is that for generalised multi-continua homogenisation it is awkward to code solutions to the homological equation [\(2.9\)](#) when it involves modes with non-zero eigenvalue/frequency. Instead we more quickly code simpler updates which just take more computer iterations to be accurate. The simplification is to omit the tricky terms $\sum_{m=0}^{M-1} \lambda_m \partial v' / \partial U_m U_m$ on the left-hand side of [\(2.9\)](#). Then the left-hand side operator is a straightforward constant matrix which is efficiently inverted or LU-factored just once

Figure 5: the sub-cell structure of the two-mode, bi-continuum, invariant manifold field (4.5a) in the high-contrast thin-layer problem. Specifically, the non-dimensional case of $\ell = 2\pi$, $\kappa_1 = 1$, and a thin insulating layer $\eta/\ell = 0.06$ located at $\theta = \pm\pi$ of insulation parameter $\chi = 1$ so $\kappa_0 = 0.06$.



(Appendix B.3) and used repeatedly. The updates v' and G' are then not exactly correct, but they are good enough to make progress. The error in the coefficients of v and G decrease each iteration by the ratio of the largest magnitude eigenvalue in the model to the smallest magnitude eigenvalue neglected by the model, here the ratio $|\lambda_{M-1}|/|\lambda_M|$. We simply let the computer do more iterations until the numerical error is small enough: Appendix B sets a maximum relative error of 10^{-8} . The numerical convergence is quicker for a larger spectral gap between λ_{M-1} and λ_M .

We now explore the two-mode bi-continuum homogenisation to second order in macroscale gradients. Upon executing the code of Appendix B, 25 iterations are sufficient to give the following detailed physics-informed sub-cell field to excellent numerical accuracy:

$$\begin{aligned} \mathbf{u}(t, x, \theta) = & U_0 + u_{01}(\theta)U_{0x} + u_{02}(\theta)U_{0xx} \\ & + v_1(\theta)U_1 + u_{11}(\theta)U_{1x} + u_{12}(\theta)U_{1xx} + \mathcal{O}(\partial_x^3), \end{aligned} \quad (4.5a)$$

in terms of five coefficient functions plotted in Figure 5.

The corresponding, but to higher-order, homogenised model for the macroscale variables U_0, U_1 is determined to be, for both $\alpha = 1, 2$,

$$\begin{aligned} \partial_t^\alpha U_0 = & + 0.3552 U_{1x} + 0.8130 U_{0xx} \\ & + 1.063 U_{1xxx} + 0.6146 U_{0xxxx} + \mathcal{O}(\partial_x^5), \end{aligned} \quad (4.5b)$$

$$\begin{aligned} \partial_t^\alpha U_1 = & -0.4597 U_1 - 0.3552 U_{0x} - 2.620 U_{1xx} \\ & - 1.736 U_{0xxx} - 17.11 U_{1xxxx} + \mathcal{O}(\partial_x^5), \end{aligned} \quad (4.5c)$$

These PDEs form the two-mode, bi-continuum, homogenisation for this high-contrast material. As discussed in [Sections 2 and 5](#) this homogenisation is supported by extant rigorous theory. In application, one truncates the PDEs (4.5) to an order of error suitable for the purposes at hand (and possibly with some suitable regularisation). In solutions obtained using a truncated (4.5), one could quantitatively estimate the modelling error via the remainder expression (23) of [Roberts \(2015a\)](#).

Sound modelling is transitive The two-mode bi-continuum homogenisation (4.5) itself has a slow manifold. For example, a low-order adiabatic approximation of (4.5c) gives $0 \approx -0.4597 U_1 - 0.3552 U_{0x}$, which leads to $U_1 \approx -0.7727 U_{0x}$. Substituting this adiabatic approximation into (4.5b) gives $\partial^\alpha U_0 / \partial t^\alpha \approx (-0.3552 \times 0.7727 + 0.8130) U_{0xx} = 0.5385 U_{0xx}$. This adiabatic slow manifold PDE model in just U_0 reproduces the leading order term of the slow manifold homogenisation constructed by the iteration of [Appendix B](#) with one-mode ($M = 1$), see the linear term in (4.9a), and thus verifies the transitivity of our sound approach to homogenisation.

4.4 Three-mode, tri-continuum, homogenisation exist and emerge

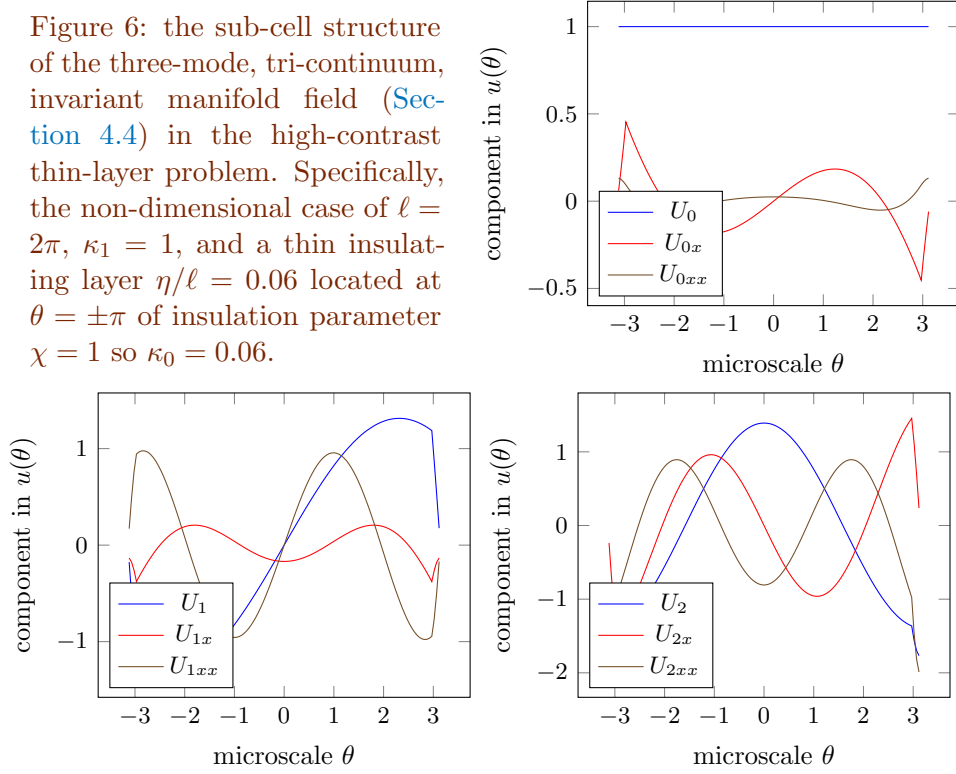
A three-mode, tri-continuum, invariant manifold, homogenisation may be constructed based upon the leading three eigenvalues: for example, $\lambda = 0, -0.42, -1$ in the nondimensional case $\chi = 1, \ell = 2\pi$, and $\kappa_1 = 1$ ([Table 1](#)). The three corresponding sub-cell modes are $v_0 = 1, v_1 \approx \sin 2\theta/\pi$, and $v_2 \approx \cos \theta$ (more precisely, the blue curves in the three panels of [Figure 6](#)). In the diffusive case, $\alpha = 1$, such a three-mode homogenisation emerges with the slowest transient decaying roughly like $e^{-2.5t}$ ([Table 1](#)). That is, this three-mode homogenisation is valid over shorter times than the two-mode, bi-continuum, homogenisation (4.5). The eigenvalue gap $(-1, -2.5)$ caters for the perturbing macroscale x -gradients.

The computer algebra of [Appendix B](#) constructs the corresponding three-mode invariant manifold homogenisation by setting the parameter $M = 3$. The algorithm requires 19 iterations to find the detailed three-mode, tri-continuum, invariant manifold field is, to low-order,

$$\begin{aligned} \mathbf{u}(t, x, \theta) = & U_0 + u_{01}(\theta)U_{0x} + u_{02}(\theta)U_{0xx} \\ & + v_1(\theta)U_1 + u_{11}(\theta)U_{1x} + u_{12}(\theta)U_{1xx} \\ & + v_2(\theta)U_2 + u_{21}(\theta)U_{2x} + u_{22}(\theta)U_{2xx} + \mathcal{O}(\partial_x^3), \end{aligned} \quad (4.6a)$$

in terms of eight coefficient functions plotted in [Figure 6](#). To higher-order, the

Figure 6: the sub-cell structure of the three-mode, tri-continuum, invariant manifold field (Section 4.4) in the high-contrast thin-layer problem. Specifically, the non-dimensional case of $\ell = 2\pi$, $\kappa_1 = 1$, and a thin insulating layer $\eta/\ell = 0.06$ located at $\theta = \pm\pi$ of insulation parameter $\chi = 1$ so $\kappa_0 = 0.06$.



corresponding evolution the of macroscale variables U_0, U_1, U_2 is determined to be, for both $\alpha = 1, 2$,

$$\begin{aligned} \partial_t^\alpha U_0 = & + 0.3552 U_{1x} + 0.8130 U_{0xx} + 0.5191 U_{2xx} \\ & - 0.2714 U_{1xxx} - 0.07643 U_{0xxxx} - 0.3184 U_{2xxxx} + \mathcal{O}(\partial_x^5), \end{aligned} \quad (4.6b)$$

$$\begin{aligned} \partial_t^\alpha U_1 = & -0.4597 U_1 - 0.3552 U_{0x} - 1.339 U_{2x} + 0.8218 U_{1xx} \\ & + 0.04649 U_{0xxx} - 0.4531 U_{2xxx} + 0.5182 U_{1xxxx} + \mathcal{O}(\partial_x^5), \end{aligned} \quad (4.6c)$$

$$\begin{aligned} \partial_t^\alpha U_2 = & -0.9804 U_2 + 1.339 U_{1x} + 0.3918 U_{0xx} - 0.2717 U_{2xx} \\ & + 0.8358 U_{1xxx} + 0.2165 U_{0xxxx} + 1.201 U_{2xxxx} + \mathcal{O}(\partial_x^5), \end{aligned} \quad (4.6d)$$

These three coupled PDEs form the three-mode, tri-continuum, homogenisation for this high-contrast material, supported by extant rigorous theory (Sections 2 and 5). In practice, one truncates and regularises this homogenisation as needed for the purposes at hand in any given scenario.

4.5 Homogenise nonlinear high-contrast heterogeneity

This methodology readily adapts to homogenising nonlinear heterogeneous systems as shown in this subsection, with its theoretical support established in the next Section 5. Here consider the high-contrast heterogeneous

problem (2.1) with the addition of nonlinear advection, namely

$$\frac{\partial^\alpha u}{\partial t^\alpha} = \frac{\partial}{\partial x} \left\{ \kappa(x) \frac{\partial u}{\partial x} \right\} - \gamma u \frac{\partial u}{\partial x}, \quad 0 < x < L. \quad (4.7)$$

In the diffusive case, $\alpha = 1$, this is a heterogeneous Burgers' PDE with nonlinearity strength parametrised by γ .

The corresponding phase-shift embedding modifies PDE (2.4) to the nonlinear

$$\frac{\partial^\alpha \mathbf{u}}{\partial t^\alpha} = \left(\frac{\partial}{\partial x} + \frac{\partial}{\partial \theta} \right) \left\{ \kappa(\theta) \left(\frac{\partial \mathbf{u}}{\partial x} + \frac{\partial \mathbf{u}}{\partial \theta} \right) \right\} - \gamma \mathbf{u} \left(\frac{\partial \mathbf{u}}{\partial x} + \frac{\partial \mathbf{u}}{\partial \theta} \right), \quad (4.8)$$

for \mathbf{u} ℓ -periodic in θ . We construct invariant manifold homogenisations of this PDE. The accessible class of manifolds is to construct homogenisations as a regular perturbation in nonlinearity parameter γ . The necessary code in the computer algebra is just two modifications: firstly, truncating to some specified order of error in γ ; and secondly, modifying the computation of the residual by including the code for the additional $+\gamma \mathbf{u}(\mathbf{u}_x + \mathbf{u}_\theta)$.

For example, first seek a one-mode homogenisation, $M = 1$, in the diffusive case, $\alpha = 1$, and to leading order effects in nonlinearity, errors $\mathcal{O}(\gamma^2)$. Executing the code of [Appendix B](#) gives in five iterations the homogenisation

$$U_{0t} = 0.5386 U_{0xx} - \gamma (U_0 U_{0x} + 1.250 U_0 U_{0xxx} + 3.106 U_{0x} U_{0xx}) + \mathcal{O}(\gamma^2, \partial_x^4) \quad (4.9a)$$

The nonlinear wave case, $\alpha = 2$, has a more complicated homogenisation. In five iterations the code of [Appendix B](#) gives the following homogenisation: in terms of $V_0(t, x) := U_{0t}$,

$$V_{0t} = 0.5386 U_{0xx} - \gamma (U_0 U_{0x} + 1.250 U_0 U_{0xxx} + 3.106 U_{0x} U_{0xx}) + \gamma (7.402 V_0 V_{0xxx} + 17.53 V_{0x} V_{0xx}) + \mathcal{O}(\gamma^2, \partial_x^4) \quad (4.9b)$$

It is only for linear systems that the nature of the time evolution operator ∂_t^α makes no difference to the algebraic expression of the right-hand side of the homogenisation. *In nonlinear systems the nature of ∂_t^α significantly affects the homogenisation algebra.*

One may also use the code of [Appendix B](#) to construct *multi-mode multi-continuum* homogenisations of the nonlinear PDE (4.7). But a multi-modes case takes many more iterations (e.g., a tri-continuum homogenisation takes 75 iterations). The reason for needing so many more iterations is primarily the smallness of the spectral gap (see [Table 1](#)). Theory for constructing nonlinear invariant manifolds indicates the bound that the spectral gap ratio *must* be larger than the order of constructed nonlinearity. Here $\mathcal{O}(\gamma)$ terms are quadratic, which means we seek second order nonlinear models. But the spectral gap ratio ([Table 1](#)) for bi-continuum or tri-continuum models is only

about 2.4. The theoretical bound is satisfied, but only by a little, and an effect of this near failure is that many more iterations are required in construction. If we here seek a cubic nonlinear multi-mode homogenisation, then the iteration diverges, reflecting a failure to meet the bound. The iteration converges for a one-mode, cubic nonlinear, homogenisation because then the spectral gap ratio is infinite. *The modelling or homogenisation of nonlinear systems requires a bigger spectral gap than that needed for linear systems.*

5 General multi-continuum, multi-mode, homogenisation of heterogeneity

Generalising the previous [Sections 2 to 4](#), this section develops in general this innovative approach to the rigorous multi-continuum, multi-mode, homogenisation of the dynamics of *nonlinear, nonautonomous, multi-physics problems in multiple large space dimensions with quasi-periodic heterogeneity*. The approach does *not* invoke any variational principle and so applies to a much wider variety of systems than many homogenisation methods. Instead, this general approach is supported by the rigorous dynamical system framework of invariant manifolds.⁸

Consider quite general multiscale materials with complicated microstructure. Suppose that the spatial domain has d dimensions of large extent, the macroscale, and possibly some thin spatial dimensions: examples include elastic beams and plates, or thin fluid films and shallow water, but also include in scope extensive 3-D materials with no thin dimension. Denote time by t , and consider times in a physically relevant interval $\mathbb{T} \subseteq \mathbb{R}$. Let position in the large dimensions be denoted by \boldsymbol{x} , and when relevant let position in the thin dimensions be denoted by z .⁹ Here we model the dynamics away from boundaries of the macroscale dimensions so we consider $\boldsymbol{x} \in \mathbb{X} \subset \mathbb{R}^d$ for some spatial domain \mathbb{X} of interest that does not include boundary layers. Let the thin domain of z be denoted by \mathbb{Z} . Let the field of interest be a function of t, \boldsymbol{x} such that $u(t, \boldsymbol{x}) \in \mathbb{H}_{\mathbb{Z}}$ for some Hilbert space $\mathbb{H}_{\mathbb{Z}}$ that contains the z -dependence. For most of the following, the z -structure is implicit via this Hilbert space of u : this implicit dependence empowers us to focus on the multiscale character of the \boldsymbol{x} -dependence in the large domain \mathbb{X} . The class

⁸(e.g., [Carr 1981](#), [Muncaster 1983a](#), [Bates et al. 1998](#), [Aulbach & Wanner 2000](#), [Prizzi & Rybakowski 2003](#), [Haragus & Iooss 2011](#), [Roberts 2015b](#), [Chekroun et al. 2015](#), [Hochs & Roberts 2019](#))

⁹The z -dimensions need not necessarily be physically thin. Instead we just need the dynamics in the z -directions to be like those we usually associate with ‘thin’ domains. For example, in reduced-order modelling of the evolution of quasi-stationary, marginal, probability distributions via multiscale Fokker–Planck PDEs one typically finds the quasi-stationary distribution is ‘effectively thin’ albeit in some ‘infinitely’ large z -directions (e.g., [van Kampen 1985](#), [Roberts 2015b](#), §18 and §21.2 respectively).

of heterogeneous problems we address is then of the general form

$$\partial_t^\alpha u = \mathcal{L}(\mathbf{x}, \boldsymbol{\theta})u - \nabla^T \mathbf{f}(\mathbf{x}, \boldsymbol{\theta}, u, u_{\mathbf{x}}) + \gamma g(t, \mathbf{x}, \boldsymbol{\theta}, u, u_{\mathbf{x}}) \quad \text{for } \boldsymbol{\theta} = \mathcal{E}^+ \mathbf{x}, \quad (5.1)$$

where ∂_t^α denotes a time evolution operator as introduced by Section 2 for PDE (2.1), and where the right-hand side is 1-periodic in $\boldsymbol{\theta}$. The linear operator $\mathcal{L}(\mathbf{x}, \boldsymbol{\theta}) : \mathbb{H}_{\mathbb{Z}} \rightarrow \mathbb{H}_{\mathbb{Z}}$ encapsulates many purely z -direction processes, and may depend upon $\mathbf{x}, \boldsymbol{\theta}$ as indicated. The unadorned gradient operator $\nabla := (\partial/\partial x_1, \dots, \partial/\partial x_d)$, whereas ∇^T is the corresponding divergence. The ‘flux’ function \mathbf{f} and the ‘forcing’ function γg may both be nonlinear functions of the field u and its gradient $u_{\mathbf{x}} := \nabla u$. We assume that the form of \mathcal{L} , \mathbf{f} , g are such that there exist general solutions $u(t)$ in the Sobolev space $W^{2,2}(\mathbb{X}) \times \mathbb{H}_{\mathbb{Z}}$ for every $t \in \mathbb{T}$.

Fish et al. (2021) [p.775] commented that the “engineering counterpart [homogenisation] based on the so-called Hill–Mandel macrohomogeneity condition assumes equivalency between the internal virtual work at an RVE level and that of the overall coarse-scale fields.” Our approach here makes *no* such assumption and so applies to a much wider range of systems such as the class (5.1).

Example 4. In addition to the heterogeneous PDEs (2.1) and (4.7), a straightforward example of (5.1) is the shear dispersion in a 2-D channel, long in the x -direction and narrow in the z -direction (say $|z| < 1$ non-dimensionally), and with heterogeneous advection-diffusion. The concentration $u(t, x, z)$ of the material is governed by the following (non-dimensional) PDE in the form of (5.1):

$$\partial_t u = \underbrace{\partial_z[\kappa(z)u_z]}_{\mathcal{L}u} - \partial_x \underbrace{[v(z)u - \kappa(z)u_x]}_{\mathbf{f}} + \underbrace{0}_{\gamma g},$$

where the diffusive mixing $\kappa(z)$ may depend upon z , and the advection velocity $v(z)$ has shear in z , such as the classic parabolic profiles $\kappa, v \propto (1-z^2)$. For this shear dispersion, Watt & Roberts (1995) showed how to develop multi-mode, multi-continuum models for the emergent macroscale dynamics. A derived low-order bi-continuum model was found to be that the concentration $u \approx U_0(t, x) + (3z^2 - 1)U_2(t, x)$ for the homogenised PDEs

$$\partial_t U_0 \approx -\bar{v}U_{0x} + \frac{2}{5}\bar{v}U_{2x}, \quad \partial_t U_2 \approx -6U_2 + \frac{1}{2}\bar{v}U_{0x},$$

in terms of the average advection $\bar{v} := \overline{v(z)}$ (their (2.22)–(2.24)). Further, Roberts & Struin (2004) discussed interpreting such two-mode bi-continuum models as physical zonal models. \square

Another example application in the class (5.1) is the one-mode modelling of Taylor dispersion in a channel with wavy walls, see Fig. 2.1 by Rosencrans (1997). A nonlinear example of (5.1) with forcing is the accurate two-mode

bi-continuum modelling of the inertial dynamics of thin fluid flow over a substrate which is arbitrarily curved over 2D macroscale space (Roberts & Li 2006).

Multiscale nature The appearance of the repeated dependence upon space \mathbf{x} in PDE (5.1), both directly via \mathbf{x} , and indirectly via $\boldsymbol{\theta} = \mathcal{E}^+\mathbf{x} \pmod{1}$, is a consequence of the multiscale spatial structure of the material. To reflect multiscale structure, the PDE (5.1) poses that the spatial variations of the coefficients $\mathcal{L}, \mathbf{f}, \gamma g$ may occur on both a macroscale directly via \mathbf{x} and on microscales using $\boldsymbol{\theta} = \mathcal{E}^+\mathbf{x}$, where \mathcal{E}^+ is defined via (5.3). The macroscale spatial variations cater for functionally graded materials¹⁰ or in the nonlinear modulation of spatial patterns¹¹. Whereas spatial variations, due to the microscale heterogeneity to be homogenised, occur via the phase variable $\boldsymbol{\theta} := \mathcal{E}^+\mathbf{x} \pmod{1}$ corresponding to the phase variable in Sections 2 to 4. We aim to prove the existence and construction of *closed and accurate* models of the macroscale dynamics of PDE (5.1) via a purely-macroscale varying, system-level, multi-modal, field $\mathbf{U}(t, \mathbf{x}) \in \mathbb{R}^M$ satisfying a homogenized macroscale PDE system of the form

$$\partial_t^\alpha \mathbf{U} = \mathbf{G}_\gamma(t, \mathbf{x}, \mathbf{U}, \mathbf{U}_\mathbf{x}, \mathbf{U}_{\mathbf{x}\mathbf{x}}, \dots), \quad (5.2)$$

for some effective purely-macroscale functional \mathbf{G}_γ .

Assumption 5 (smoothness). *The operator \mathcal{L} and functions \mathbf{f} and g on the right-hand side of PDE (5.1) are to be smooth functions of their arguments $t, \mathbf{x}, u, u_\mathbf{x}$, and if g is non-autonomous, then g varies relatively slowly in time t .¹² We define smooth to mean continuously differentiable to an order q sufficient for the purposes at hand, uniformly C^q for some q , possibly infinitely differentiable, C^∞ .*

The $\boldsymbol{\theta}$ -dependence in PDE (5.1) need not be so smooth. An example being the piecewise constant coefficient $\kappa(x)$ in the high-contrast example of Section 4. The crucial constraint on the $\boldsymbol{\theta}$ -dependence is that Assumption 8 on a general eigenfunction decomposition needs to be met.

Microscale heterogeneity We suppose that the microscale heterogeneity in $\mathbf{x} \in \mathbb{R}^d$, represented via the variable $\boldsymbol{\theta} = \mathcal{E}^+\mathbf{x}$, is possibly quasi-periodic with some number P of incommensurable vector periods $\boldsymbol{\ell}_p \in \mathbb{R}^d$ for $p = 1, \dots, P$. For example, a 3-D bulk material with microscale heterogeneity

¹⁰(e.g., Chen et al. 2024, Anthoine 2010, Roberts 2024, §6.1)

¹¹(e.g., Cross & Hohenberg 1993, Roberts 2015a, §3.3)

¹²Rapid fluctuations in time could be accommodated by also homogenising over such fluctuations but let's not include this within scope here.

varying ℓ -periodically in each direction (a cubic cell) has periods $\boldsymbol{\ell}_1 := (\ell, 0, 0)$, $\boldsymbol{\ell}_2 := (0, \ell, 0)$, and $\boldsymbol{\ell}_3 := (0, 0, \ell)$; whereas if the x_1 -direction was instead quasi-periodic with periods ℓ and $\ell/\sqrt{2}$, then include the additional fourth vector period $\boldsymbol{\ell}_4 := (\ell/\sqrt{2}, 0, 0)$. Define both the $d \times P$ matrix¹³

$$\mathcal{E} := [\boldsymbol{\ell}_1 \ \cdots \ \boldsymbol{\ell}_P], \quad \text{and } \mathcal{E}^+ \text{ is its Moore–Penrose pseudo-inverse} \quad (5.3)$$

(e.g., Golub & van Loan 2013). This pseudo-inverse \mathcal{E}^+ appears in the general system (5.1). In the approach here, the appearance of \mathcal{E} often parallels that of the asymptotically small parameter ϵ in asymptotic homogenisation methods. The pseudo-inverse \mathcal{E}^+ correspondingly parallels that of $1/\epsilon$. However, in contrast to other methods, we do *not* invoke limits $\ell_p \rightarrow 0$: all the vector periods $\boldsymbol{\ell}_p$ are some fixed physical microscale displacements in \mathbb{R}^d that happen to be relatively small compared to the length L of the macroscales of interest. Our approach and results here apply to the physically relevant cases of finite scale separation ratios ℓ_p/L . The results are *not* restricted to the mathematical limits $\ell_p/L \rightarrow 0$.

5.1 Phase-shift embedding

Generalising Section 2.1, and in a novel, rigorous and efficient twist to the concept of a Representative Volume Element, let’s embed any specific given physical PDE (5.1) into a family of PDE problems formed by all phase-shifts of the (quasi-)periodic microscale. This embedding is cognate to that used for quasicrystals in multi-D space by Jiang et al. (2024), Jiang & Zhang (2014). But their approach and methods are in a global Fourier space and so do not appear to cater for macroscale spatial modulation of the microscale heterogeneity, nor in the solution, nor for the general class of problems (5.1) considered here. Rokoš et al. (2019) used a cognate family of phase-shifts of the material shown in Figure 1 in order to compute its deformed equilibria.

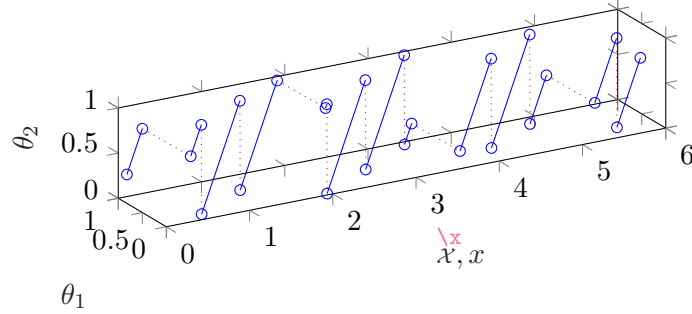
As indicated by the schematic case illustrated in Figure 7, let’s create the desired phase-shift embedding by considering a field $\mathbf{u}(t, \boldsymbol{x}, \boldsymbol{\theta})$, implicitly depending on z , and satisfying the PDE¹⁴

$$\begin{aligned} \partial_t^\alpha \mathbf{u} &= \mathcal{L}(\boldsymbol{x}, \boldsymbol{\theta})\mathbf{u} - (\nabla_{\boldsymbol{x}}^T + \nabla_{\boldsymbol{\theta}}^T \mathcal{E}^+) \mathbf{f}(\boldsymbol{x}, \boldsymbol{\theta}, \mathbf{u}, \mathbf{u}_{\boldsymbol{x}} + \mathcal{E}^{+T} \mathbf{u}_{\boldsymbol{\theta}}) \\ &\quad + \gamma g(t, \boldsymbol{x}, \boldsymbol{\theta}, \mathbf{u}, \mathbf{u}_{\boldsymbol{x}} + \mathcal{E}^{+T} \mathbf{u}_{\boldsymbol{\theta}}), \end{aligned} \quad (5.4)$$

¹³For the given four-vector quasi-periodic example, the matrix \mathcal{E} and its Moore–Penrose pseudo-inverse are $\mathcal{E} = \ell \begin{bmatrix} 1 & 0 & 0 & 1/\sqrt{2} \\ 0 & 1 & 0 & 0 \\ 0 & 0 & 1 & 0 \end{bmatrix}$ and $\mathcal{E}^+ = \frac{1}{\ell} \begin{bmatrix} 2/3 & 0 & 0 \\ 0 & 1 & 0 \\ 0 & 0 & 1 \\ \sqrt{2}/3 & 0 & 0 \end{bmatrix}$, for which $\mathcal{E}\mathcal{E}^+ = I_3$.

¹⁴I conjecture that systems in forms other than the general form (5.1) may be similarly embedded. The rule for derivatives is that a gradient $\nabla \mapsto \nabla_{\boldsymbol{x}} + \mathcal{E}^{+T} \nabla_{\boldsymbol{\theta}}$ whereas a divergence $\nabla^T \mapsto \nabla_{\boldsymbol{x}}^T + \nabla_{\boldsymbol{\theta}}^T \mathcal{E}^+$.

Figure 7: schematic domain of the multiscale embedding PDE (5.4) for a field $u(t, \boldsymbol{x}, \boldsymbol{\theta})$, for $\boldsymbol{x} \in \mathbb{X} \subset \mathbb{R}$ and for $\boldsymbol{\theta} \in \Theta := [0, 1]^2$. Here the periodicities $l_1 = 1.62$ and $l_2 = 0.72$ so $\mathcal{E} = [1.62 \ 0.72]$. We obtain solutions of the heterogeneous PDE (5.1) on such blue lines as $u_\phi(t, x) := u(t, x, \phi + \mathcal{E}^+x)$ for every constant phase $\phi \in \mathbb{R}^2$, here $\phi = (0.82, 0.32)$, and where the third argument of u has components modulo 1.



in the domain $\mathbb{D} := \mathbb{X} \times \Theta \times \mathbb{Z}$ for the unit P -cube $\Theta := [0, 1]^P$, and with boundary conditions of 1-periodicity in θ_p . The subscripts \boldsymbol{x} and $\boldsymbol{\theta}$ denote the respective gradient operator, that is, $u_{\boldsymbol{x}} := \nabla_{\boldsymbol{x}} u$ and $u_{\boldsymbol{\theta}} := \nabla_{\boldsymbol{\theta}} u$. We assume that the heterogeneous explicit dependence upon $\boldsymbol{x}, \boldsymbol{\theta}$ in $\mathcal{L}, \boldsymbol{f}, g$ are regular enough that general solutions u of PDE (5.4) are in $\mathbb{H}_{\mathbb{D}}^N := W^{(N+1, 2), p}(\mathbb{X} \times \Theta) \times \mathbb{H}_{\mathbb{Z}}$ for some chosen order N . The domain \mathbb{D} (Figure 7) is multiscale as it is large in \boldsymbol{x} , and relatively thin in both z and $\boldsymbol{\theta}$. I emphasise that this domain has finite aspect ratio: we do *not* take any limit involving an aspect ratio tending to zero nor to infinity.

Figure 7 indicates that we regard $\boldsymbol{x} = \boldsymbol{x}$. The distinction between \boldsymbol{x} and \boldsymbol{x} is that partial derivatives in \boldsymbol{x} are done keeping $\boldsymbol{\theta}$ constant (e.g., parallel to the \boldsymbol{x} -axis in Figure 7), whereas partial derivatives in \boldsymbol{x} are done keeping the phase-shift ϕ constant (e.g., along the (blue) diagonal lines in Figure 7).

Lemma 6. For every smooth solution $\mathbf{u}(t, \mathbf{x}, \boldsymbol{\theta}) \in \mathbb{H}_{\mathbb{D}}^N$ of the embedding PDE (5.4), and for every vector of phases $\boldsymbol{\phi}$, the field $u_{\boldsymbol{\phi}}(t, \mathbf{x}) := \mathbf{u}(t, \mathbf{x}, \boldsymbol{\phi} + \mathcal{E}^+ \mathbf{x})$ (for example, the field \mathbf{u} evaluated on the solid-blue lines in Figure 7) is in the Sobolov space $W^{2,2}(\mathbb{X}) \times \mathbb{H}_{\mathbb{Z}}$, and satisfies the heterogeneous, phase-shifted, PDE

$$\begin{aligned} \partial_t^\alpha u_{\boldsymbol{\phi}} &= \mathcal{L}(\mathbf{x}, \boldsymbol{\phi} + \mathcal{E}^+ \mathbf{x}) u_{\boldsymbol{\phi}} - \nabla^T \mathbf{f}(\mathbf{x}, \boldsymbol{\phi} + \mathcal{E}^+ \mathbf{x}, u_{\boldsymbol{\phi}}, \nabla u_{\boldsymbol{\phi}}) \\ &\quad + \gamma g(t, \mathbf{x}, \boldsymbol{\phi} + \mathcal{E}^+ \mathbf{x}, u_{\boldsymbol{\phi}}, \nabla u_{\boldsymbol{\phi}}). \end{aligned} \quad (5.5)$$

Hence $u_{\mathbf{0}}(t, \mathbf{x}) := \mathbf{u}(t, \mathbf{x}, \mathcal{E}^+ \mathbf{x})$ satisfies the given heterogeneous PDE (5.1).

Recall that the most common boundary conditions *assumed* for RVEs are periodic, although in the usual homogenization arguments other boundary conditions appear equally as valid despite giving slightly different results (e.g., Mercer et al. 2015). In contrast, here the boundary conditions of 1-periodicity in microscale $\boldsymbol{\theta}$ are *not* assumed but instead arise naturally due to the ensemble of phase-shifts. That is, what in other approaches has to be assumed, in this approach arises naturally.

Proof. Start by considering the left-hand side of PDE (5.5), namely the time evolution operator

$$\begin{aligned} \partial_t^\alpha u_{\boldsymbol{\phi}} &= \partial_t^\alpha \mathbf{u}(t, \mathbf{x}, \boldsymbol{\phi} + \mathcal{E}^+ \mathbf{x}) \\ &= [\partial_t^\alpha \mathbf{u}]_{(t, \mathbf{x}, \boldsymbol{\phi} + \mathcal{E}^+ \mathbf{x})} \quad (\text{which by PDE (5.4) becomes}) \\ &= [\mathcal{L} \mathbf{u} - (\nabla_{\boldsymbol{\chi}}^T + \nabla_{\boldsymbol{\theta}}^T \mathcal{E}^+) \mathbf{f}(\boldsymbol{\chi}, \boldsymbol{\theta}, \mathbf{u}, \mathbf{u}_{\boldsymbol{\chi}} + \mathcal{E}^{+T} \mathbf{u}_{\boldsymbol{\theta}}) \\ &\quad + \gamma g(t, \boldsymbol{\chi}, \boldsymbol{\theta}, \mathbf{u}, \mathbf{u}_{\boldsymbol{\chi}} + \mathcal{E}^{+T} \mathbf{u}_{\boldsymbol{\theta}})]_{(t, \mathbf{x}, \boldsymbol{\phi} + \mathcal{E}^+ \mathbf{x})} \\ &= [\mathcal{L}(\boldsymbol{\chi}, \boldsymbol{\theta}) \mathbf{u}]_{(t, \mathbf{x}, \boldsymbol{\phi} + \mathcal{E}^+ \mathbf{x})} - \nabla^T \left\{ [\mathbf{f}(\boldsymbol{\chi}, \boldsymbol{\theta}, \mathbf{u}, \mathbf{u}_{\boldsymbol{\chi}} + \mathcal{E}^{+T} \mathbf{u}_{\boldsymbol{\theta}})]_{(t, \mathbf{x}, \boldsymbol{\phi} + \mathcal{E}^+ \mathbf{x})} \right\} \\ &\quad + \gamma g(t, \mathbf{x}, \boldsymbol{\phi} + \mathcal{E}^+ \mathbf{x}, u_{\boldsymbol{\phi}}, \nabla u_{\boldsymbol{\phi}}) \\ &= \mathcal{L}(\mathbf{x}, \boldsymbol{\phi} + \mathcal{E}^+ \mathbf{x}) u_{\boldsymbol{\phi}} - \nabla^T \mathbf{f}(\mathbf{x}, \boldsymbol{\phi} + \mathcal{E}^+ \mathbf{x}, u_{\boldsymbol{\phi}}, \nabla u_{\boldsymbol{\phi}}) \\ &\quad + \gamma g(t, \mathbf{x}, \boldsymbol{\phi} + \mathcal{E}^+ \mathbf{x}, u_{\boldsymbol{\phi}}, \nabla u_{\boldsymbol{\phi}}), \end{aligned}$$

namely the right-hand side of (5.5). Hence, provided PDE (5.4) has boundary conditions of 1-periodicity in θ_p , every solution of the embedding PDE (5.4) gives a solution of the original PDE (5.1) for every P -dimensional phase-shift $\boldsymbol{\phi}$ of the heterogeneity.

In particular, the field $u_{\mathbf{0}}(t, \mathbf{x})$, of phase-shift $\boldsymbol{\phi} = \mathbf{0}$, satisfies the given heterogeneous PDE (5.1). \square

Lemma 7 (converse). *Suppose we have a family of solutions $u_\phi(t, \mathbf{x})$ of the phase-shifted PDE (5.5)—a family parametrised by the phase vector $\phi \in \mathbb{R}^p$ —and the family depends smoothly enough upon t, \mathbf{x}, ϕ that the following $\mathbf{u} \in \mathbb{H}_{\mathbb{D}}^N$. Then the field $\mathbf{u}(t, \mathbf{x}, \boldsymbol{\theta}) := u_{\boldsymbol{\theta} - \mathcal{E}^+ \mathbf{x}}(t, \mathbf{x})$ satisfies the embedding PDE (5.4).*

Proof. First, from the PDE (5.4), consider

$$\begin{aligned} \mathbf{u}_{\mathbf{x}} + \mathcal{E}^{+T} \mathbf{u}_{\boldsymbol{\theta}} &= \left[(-\mathcal{E}^+)^T \frac{\partial u_\phi}{\partial \phi} + \frac{\partial u_\phi}{\partial \mathbf{x}} + \mathcal{E}^{+T} \frac{\partial u_\phi}{\partial \phi} \right]_{\phi = \boldsymbol{\theta} - \mathcal{E}^+ \mathbf{x}, \mathbf{x} = \mathbf{x}} \\ &= [\nabla u_\phi]_{\phi = \boldsymbol{\theta} - \mathcal{E}^+ \mathbf{x}, \mathbf{x} = \mathbf{x}}. \end{aligned}$$

Second, since $\phi = \boldsymbol{\theta} - \mathcal{E}^+ \mathbf{x} = \boldsymbol{\theta} - \mathcal{E}^+ \mathbf{x}$, that is $\boldsymbol{\theta} = \phi + \mathcal{E}^+ \mathbf{x}$, then for every smooth $\mathbf{f}(\mathbf{x}, \boldsymbol{\theta})$, $(\nabla_{\mathbf{x}}^T + \nabla_{\boldsymbol{\theta}}^T \mathcal{E}^+) \mathbf{f} = \nabla^T \{ \mathbf{f} |_{\mathbf{x} = \mathbf{x}, \boldsymbol{\theta} = \phi + \mathcal{E}^+ \mathbf{x}} \}$. Thirdly, hence the right-hand-side of PDE (5.4) becomes

$$\begin{aligned} &\mathcal{L}(\mathbf{x}, \boldsymbol{\theta}) \mathbf{u} - (\nabla_{\mathbf{x}}^T + \nabla_{\boldsymbol{\theta}}^T \mathcal{E}^+) \mathbf{f}(\mathbf{x}, \boldsymbol{\theta}, \mathbf{u}, \mathbf{u}_{\mathbf{x}} + \mathcal{E}^{+T} \mathbf{u}_{\boldsymbol{\theta}}) \\ &\quad + \gamma g(t, \mathbf{x}, \boldsymbol{\theta}, \mathbf{u}, \mathbf{u}_{\mathbf{x}} + \mathcal{E}^{+T} \mathbf{u}_{\boldsymbol{\theta}}) \\ &= [\mathcal{L}(\mathbf{x}, \boldsymbol{\theta}) \mathbf{u}]_{\mathbf{x} = \mathbf{x}, \boldsymbol{\theta} = \phi + \mathcal{E}^+ \mathbf{x}} - \nabla^T \{ \mathbf{f}(\mathbf{x}, \boldsymbol{\theta}, \mathbf{u}, \mathbf{u}_{\mathbf{x}} + \mathcal{E}^{+T} \mathbf{u}_{\boldsymbol{\theta}}) |_{\mathbf{x} = \mathbf{x}, \boldsymbol{\theta} = \phi + \mathcal{E}^+ \mathbf{x}} \} \\ &\quad + \gamma g(t, \mathbf{x}, \boldsymbol{\theta}, \mathbf{u}, \mathbf{u}_{\mathbf{x}} + \mathcal{E}^{+T} \mathbf{u}_{\boldsymbol{\theta}}) |_{\mathbf{x} = \mathbf{x}, \boldsymbol{\theta} = \phi + \mathcal{E}^+ \mathbf{x}} \\ &= \mathcal{L}(\mathbf{x}, \phi + \mathcal{E}^+ \mathbf{x}) u_\phi - \nabla^T \mathbf{f}(\mathbf{x}, \phi + \mathcal{E}^+ \mathbf{x}, u_\phi, \nabla u_\phi) \\ &\quad + \gamma g(t, \mathbf{x}, \phi + \mathcal{E}^+ \mathbf{x}, u_\phi, \nabla u_\phi), \end{aligned}$$

the right-hand side of PDE (5.5). Lastly, since $\partial_t^\alpha \mathbf{u}(t, \mathbf{x}, \boldsymbol{\theta}) = \partial_t^\alpha u_{\boldsymbol{\theta} - \mathcal{E}^+ \mathbf{x}}$ it follows that $\mathbf{u} := u_{\boldsymbol{\theta} - \mathcal{E}^+ \mathbf{x}}(t, \mathbf{x})$ satisfies the embedding PDE (5.4). \square

Consequently, PDEs (5.1) and (5.4) are equivalent, and they may provide us with an ensemble of solutions for an ensemble of materials all with the same heterogeneity structure, but with the structural phase of the material shifted through all possible phases. The key difference between PDEs (5.1) and (5.4) is that although PDE (5.1) is heterogeneous in space \mathbf{x} , the embedding PDE (5.4) is *homogeneous* in space \mathbf{x} . Because of this homogeneity, Section 5.2 is empowered to apply an existing rigorous theory for slow variations in space that leads to desired multi-continuum homogenisations of the PDE (5.4), and hence to that of (5.1).

5.2 Invariant manifolds of multi-continuum, micromorphic, any-order homogenization

Generalising Section 2.2, let's analyse the embedding PDE (5.4) for useful 'homogenized' invariant manifolds. Such invariant manifolds are to express and support the relevance of a potential hierarchy of accurate homogenizations

for the original heterogeneous PDE (5.1). The systematic approach developed simplifies considerably much of the “difficulty to choose a priori an appropriate model for a given microstructure” discussed by Alavi et al. (2023) [p.2164].

Developments in dynamical systems theory¹⁵ inspired by earlier more formal arguments¹⁶ establishes how to construct a PDE model for the macroscale spatial structure of PDE solutions in multiscale domains \mathbb{D} such as Figure 7. The technique is to base analysis on the case where variations in \boldsymbol{x} are over a large enough scale that they are approximately negligible—the variations are both directly in the parametric \boldsymbol{x} dependence of \mathcal{L} , \boldsymbol{f} , g and indirectly via the field \boldsymbol{u} . Then we treat finite, macroscale, variations in \boldsymbol{x} as a regular perturbation. Despite the derivative $\partial_{\boldsymbol{x}}$ being an unbounded operator, the theoretical developments justify being able to treat such derivatives as ‘small’ (e.g., Roberts & Bunder 2017, p.987). Hence the perturbation analysis proceeds to any chosen order N in the ‘small’ derivatives $\partial_{\boldsymbol{x}}$ with quantifiable remainder error (Roberts & Bunder 2017, (52)).

For two examples in linear elasticity systems, the usual leading order homogenizations are the case $N = 2$, and the so-called second-order homogenizations¹⁷ correspond to the higher-order $N = 4$. Because of the power of the established dynamical system framework, here we allow arbitrary order N .

5.2.1 Linear basis of invariant manifolds

Invariant manifolds are mostly constructed from the base of an equilibrium or a family of equilibria, as we do here to generalise Section 2.2. In the vicinity of each and every equilibria we characterise all solutions in terms of spectral properties of the system’s linearisation. Consequently, we then construct relevant invariant manifolds that pass through the base equilibria and extend into the state space. The correspondingly constructed evolution then forms a closed accurate macroscale homogenization.

Equilibria Following Bunder & Roberts (2021) we consider the dynamics of the embedding PDE (5.4) in a mesoscale locale of each and every ‘cross-section’ position $\boldsymbol{x} = \boldsymbol{X} \in \mathbb{X}$ of interest in the physical problem at hand. In such a mesoscale locale the variations in macroscale variable \boldsymbol{x} are small enough so that for *linearisation* purposes we consider the macroscale gradients negligible, $\nabla_{\boldsymbol{x}} \equiv 0$. Many secondary physical nonlinearities or forcing effects are gathered into $g(t, \boldsymbol{x}, \boldsymbol{\theta}, \boldsymbol{u}, \boldsymbol{u}_{\boldsymbol{x}} + \boldsymbol{u}_{\boldsymbol{\theta}})$, multiplied by perturbation parameter γ , so we seek equilibria that requires the coefficient $\gamma = 0$.

¹⁵(Bunder & Roberts 2021, Roberts & Bunder 2017, Roberts 2015a)

¹⁶(Roberts 1988, 1997)

¹⁷(e.g., Anthoine 2010, Cornaggia & Guzina 2020, Hii & El Said 2022)

That invariant manifold theory supports modelling in the vicinity of each equilibria¹⁸ empowers us to systematically and accurately model effects with non-zero gradients $\nabla_{\mathbf{x}}$, non-zero γ , and from nonlinearities.

With effectively zero $\nabla_{\mathbf{x}}$ and zero γ the dynamics of the embedding PDE (5.4) in the locale near \mathbf{X} reduces to the cross-sectional, *cell-problem*

$$\partial_t^\alpha \mathbf{u} = \mathcal{L}(\mathbf{X}, \boldsymbol{\theta})\mathbf{u} - \nabla_{\boldsymbol{\theta}}^T \mathbf{f}(\mathbf{X}, \boldsymbol{\theta}, \mathbf{u}, \mathcal{E}^{+T} \mathbf{u}_{\boldsymbol{\theta}}), \quad (5.6)$$

for 1-periodicity in θ_p , and at every cross-section $\mathbf{X} \in \mathbb{X}$ of interest. For each \mathbf{X} , the cross-sectional PDE (5.6) is a *cell-problem* in that it only contains dependence upon $\boldsymbol{\theta}$ and implicitly z . The following treatment of PDE (5.6) is parametrised by the macroscale locale \mathbf{X} , and so many of the quantities identified may depend upon \mathbf{X} , as in functionally graded materials¹⁹, although often not. For brevity, any such \mathbf{X} -dependence is mostly implicit in the following.

We assume that the cell-problem (5.6) has one or more chosen equilibria $\mathbf{u} = \mathbf{u}^*(\boldsymbol{\theta}) \in \mathbb{H}_{\Theta} \times \mathbb{H}_{\mathbb{Z}}$. Often these equilibria will zero the flux \mathbf{f} . Often the equilibria \mathbf{u}^* are constant in $\boldsymbol{\theta}$ and in z : but, they need not be constant. Often the chosen equilibria form a subspace such as $\mathbf{u}^* \propto v_0(\boldsymbol{\theta})$ for some v_0 . Define $\mathbb{E} := \{\text{chosen equilibria } \mathbf{u}^*\} \subset \mathbb{H}_{\Theta} \times \mathbb{H}_{\mathbb{Z}}$. That is, $\mathcal{L}\mathbf{u}^* - \nabla_{\boldsymbol{\theta}}^T \mathbf{f}(\mathbf{X}, \boldsymbol{\theta}, \mathbf{u}^*, \mathcal{E}^{+T} \mathbf{u}_{\boldsymbol{\theta}}^*) = 0$ for every $\mathbf{u}^* \in \mathbb{E}$.

In application, one often has useful physical intuition about a suitable base set of equilibria \mathbb{E} for the scenarios of interest. One then introduces the artificial ordering parameter γ into the governing equations so that $\mathcal{L}\mathbf{u} + \nabla_{\boldsymbol{\theta}}^T \mathbf{f}$ has the desired equilibria \mathbb{E} , and all other terms are gathered into γg (e.g., Roberts 2015b, §9.1 and Part V). The systematic framework here empowers arbitrary order construction in such an artificial γ (Section 5.3) to enable reasonable prediction at the physically relevant γ (usually at $\gamma = 1$).

Characterise nearby dynamics via linearisation For each $\mathbf{u}^* \in \mathbb{E}$, explore the nearby dynamics by seeking solutions to the cell-problem (5.6) in the form $\mathbf{u} = \mathbf{u}^*(\boldsymbol{\theta}) + \hat{\mathbf{u}}(t, \boldsymbol{\theta})$ for small $\hat{\mathbf{u}}$. Then, invoking Frechet derivatives, the flux becomes

$$\begin{aligned} \mathbf{f} &= \mathbf{f}(\mathbf{X}, \boldsymbol{\theta}, \mathbf{u}^* + \hat{\mathbf{u}}, \mathbf{u}_{\boldsymbol{\theta}}^* + \hat{\mathbf{u}}_{\boldsymbol{\theta}}) \\ &\approx \mathbf{f}(\mathbf{X}, \boldsymbol{\theta}, \mathbf{u}^*, \mathbf{u}_{\boldsymbol{\theta}}^*) + \underbrace{\frac{\partial \mathbf{f}}{\partial \mathbf{u}}(\mathbf{X}, \boldsymbol{\theta}, \mathbf{u}^*, \mathbf{u}_{\boldsymbol{\theta}}^*)}_{=: \mathcal{J}^*(\mathbf{X}, \mathbf{y})} \hat{\mathbf{u}} + \underbrace{\frac{\partial \mathbf{f}}{\partial \mathbf{u}_{\boldsymbol{\theta}}}(\mathbf{X}, \boldsymbol{\theta}, \mathbf{u}^*, \mathbf{u}_{\boldsymbol{\theta}}^*)}_{=: \mathcal{J}^*(\mathbf{X}, \boldsymbol{\theta})} \hat{\mathbf{u}}_{\boldsymbol{\theta}}. \end{aligned}$$

¹⁸(Aulbach & Wanner 2000, Prizzi & Rybakowski 2003, Hochs & Roberts 2019, Bunder & Roberts 2021)

¹⁹(e.g., Chen et al. 2024, Anthoine 2010, Roberts 2024, §6.1)

To characterise general solutions to the nearby dynamics we thus address the cell eigen-problem

$$\lambda v = \mathfrak{L}v, \quad \text{where } \mathfrak{L}v := \mathcal{L}v - \nabla_{\boldsymbol{\theta}}^T (J^*v + J^*v_{\boldsymbol{\theta}}), \quad \text{1-periodic in } \theta_p, \quad (5.7)$$

for cell eigenvalues λ and cell eigenfunctions $v(\boldsymbol{\theta})$. Often the set \mathbb{E} is chosen so that the cell-problem is independent of the equilibria $\mathbf{u}^* \in \mathbb{E}$.

Assumption 8 (eigenfunction decomposition). *Firstly, assume that non-empty \mathbb{X}, \mathbb{E} exist where for every cross-section $\mathbf{X} \in \mathbb{X}$ and every equilibrium $\mathbf{u}^* \in \mathbb{E}$, there exists for the cell eigen-problem (5.7) a complete countable set of (generalised) eigenfunctions $v_m(\boldsymbol{\theta})$ for corresponding eigenvalues λ_m (sometimes complex valued), for index $m = 0, 1, 2, \dots$ (ordered so that $\Re\lambda_{m+1} \leq \Re\lambda_m$, and if $\Re\lambda_{m+1} = \Re\lambda_m$ then $\Im\lambda_{m+1} \leq \Im\lambda_m$). Secondly, assume that there exists a countable set of corresponding (generalised) adjoint eigenfunctions $w_m(\boldsymbol{\theta})$ normalised so that $\langle w_m, v_m \rangle = \delta_{m,n}$, such that the linear operator $\mathfrak{L} = \sum_{m=1}^{\infty} \lambda_m v_m \langle w_m, \cdot \rangle + \zeta_m v_m \langle w_{m+1}, \cdot \rangle$ in the space $\mathbb{H}_{\Theta \times \mathbb{Z}}$ (where $\zeta_m = 0$ when $\lambda_m \neq \lambda_{m+1}$), and that $\mathbb{H}_{\Theta \times \mathbb{Z}}$ is the closure of absolutely convergent series for this decomposition of $\mathfrak{L}u$. Thirdly, assume these eigenfunctions and eigenvalues vary smoothly with macroscale $\mathbf{X} \in \mathbb{X}$.*

Often the cell eigen-problem (5.7) is independent of macroscale \mathbf{X} . However, functionally graded materials that have graduations in a large space dimension are examples of \mathbf{X} -dependence. If such a graded material has a sudden/step change in material properties, then such a change generates physical ‘boundary’ layers that have to be excised from the spatial domain \mathbb{X} . Such physical ‘boundary’ layers about a material change are instead resolved in the homogenisation via an argument akin to that for boundary conditions (e.g., [Roberts 1992](#), [Chen et al. 2018](#)).

For each in \mathbb{X} and \mathbb{E} , since the eigenfunctions are complete, a general solution to the *linearised* cell-problem (5.6) is thus²⁰

$$\mathbf{u} = \mathbf{u}^* + \sum_{m=1}^{\infty} a_m(t) v_m(\boldsymbol{\theta}), \quad (5.8a)$$

where $a_m(t)$ is a general solution to the m th-mode ODE

$$\partial_t^\alpha a_m = \lambda_m a_m. \quad (5.8b)$$

²⁰In cases where generalised eigenfunctions occur for the same eigenvalue ($\zeta_m \neq 0$ in [Assumption 8](#)), then the evolution of those corresponding a_m is more complicated. Typically there are a finite number of generalised eigenvectors for a given eigenvalues, and the evolution then includes some multiplicative factors that grow algebraically in time. For brevity we do not detail such cases here.

Now the developing argument splits depending upon the nature of ∂_t^α , the spectrum of eigenvalues $\{\lambda_m : m = 0, 1, 2, \dots\}$, and also upon external knowledge about the physical problem and its context. It is not feasible to address all the myriad of possibilities for the time evolution operator ∂_t^α . Instead we focus mainly on the two main cases of first- and second-order time derivatives, $\alpha = 1, 2$, and discuss briefly other cases.

Perhaps use cells twice the minimum size But before we leave the cell-problem, recall the material and deformation shown by [Figure 1](#). In the un-deformed state, such as the left and right ends of the material as shown, the periodic heterogeneous cell is clearly a square, say with side length ℓ , each microscale square with one circular inclusion. However, choosing such a cell results in homogenisations that are almost certainly unable to predict the checkerboard pattern in the middle of [Figure 1](#)—the macroscale variations would be too short for validity of the homogenisation. To encompass this checkerboard deformation one should instead aim for a square cell of size $2\ell \times 2\ell$ containing four inclusions; that is, embed the physical problem using heterogeneity period 2ℓ in both directions. Then a local checkerboard pattern can be one of the sub-cell modes $v_m(\boldsymbol{\theta})$ in a multi-continuum micromorphic homogenisation (e.g., [Rokoš et al. 2019](#)).

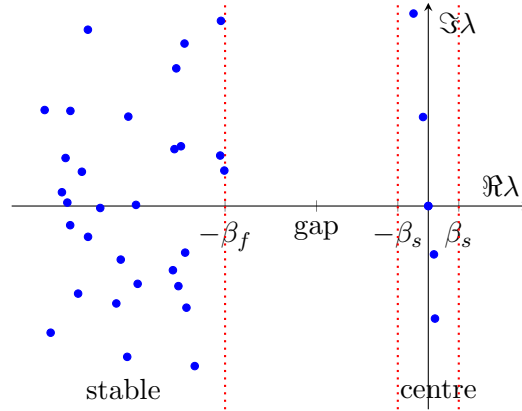
[Combescure \(2022\)](#) used cognate 1-D examples in discussing selecting generalized continuum models for materials displaying microstructure instabilities. Indeed, recall Mathieu’s equation for oscillations in $u(t)$ with parametric forcing, $u_{tt} + (\omega^2 + \epsilon \cos t)u = 0$ (e.g., [Roberts 2015b](#), §3.7.1). This system has instabilities when the natural frequency $\omega = k/2$ for integer k . The strongest instability is when $\omega = 1/2$, that is, at twice the period of the forcing. The spatial analogue for homogenisation is that a likely candidate for a mode in a micromorphic homogenisation is one with twice the wavelength of the underlying heterogeneity, as in [Figure 1](#), and captured in our systematic homogenisation via an embedding with cells of twice the minimal size.

5.2.2 Systems with significant dissipation

The case $\alpha = 1$ is the case of first-order in time PDE [\(5.1\)](#). This case usually has the cleanest argument and most rigorous support. General solutions to the m th-mode ODE [\(5.8b\)](#) are exponentials in time: $a_m = A_m e^{\lambda_m t}$.²¹ Typically most of these cell eigenvalues λ_m have large negative real-part (see the schematic example of [Figure 8](#)), and so the corresponding cell modes decay to zero very quickly. It is the relatively few cell eigenvalues λ_m with small real-part that determine the long-time macroscale evolution.

²¹Albeit possibly multiplied by a polynomial in t in the case of generalised eigenfunctions.

Figure 8: schematic picture of the complex plane of eigenvalues λ_m (blue dots) forming two separate sets characterised by bounding parameters β_s and β_f of the ‘slow’ centre modes and fast stable modes, respectively.



As indicated in [Figure 8](#) (and also [Figure 9](#)) we suppose that there are no eigenvalues with significantly positive real-part as then the linear dynamics would predict cell mode(s) with rapid exponential growth. Such ‘exploding’ modes ruin the usefulness of the equilibrium as a base from which to form a model. Hence we restrict attention to equilibria \mathbb{E} whose spectrum has no eigenvalues with significantly positive real-part.

A rational multi-continuum model is formed by identifying a significant *gap* in the spectrum of cell-eigenvalues, such as that shown in [Figure 8](#), that holds for all $\mathbf{X} \in \mathbb{X}$. In a physical application one aims to resolve macroscale time variations longer than some minimum timescale of interest t_s : in such a case one seeks a spectral gap with bounds $\beta_s < 1/t_s < \beta_f$ (preferably $\beta_s \ll 1/t_s \ll \beta_f$). Identifying such a gap identifies M *centre* cell-eigenvalues, as in [Figure 8](#), and for convenience suppose we have indexed the eigenvalues so that these are $\lambda_0, \dots, \lambda_{M-1}$. Commonly there is one or two conserved cell modes (cell-eigenvalues zero) and all other eigenvalues have negative real-part, whence we may choose to identify $\beta_s = 0$, and the argument here then leads to the common homogenised models. But if appropriate for the physical scenarios of interest, then one may alternatively choose to include more sub-cell modes in the modelling as we allow here. The corresponding M cell-eigenfunctions v_0, \dots, v_{M-1} are M -microscale modes that form the basis of an M -D subspace $\mathbb{M}_{\mathbf{X}}$ of $\mathbb{H}_{\Theta \times \mathbb{Z}}$ that is invariant to the linearised cell-dynamics [\(5.6\)](#). All the other cell-modes v_m , for $m \geq M$, called *stable* modes, decay faster than $e^{-\beta_f t}$. Hence, within the linearised dynamics the invariant subspace $\mathbb{M}_{\mathbf{X}}$ of the centre modes is exponentially quickly *emergent* on the chosen macroscale times t_s of interest. Since the eigenvalue bounds hold for all $\mathbf{X} \in \mathbb{X}$, the union $\mathbb{M} := \cup_{\mathbf{X} \in \mathbb{X}} \mathbb{M}_{\mathbf{X}}$ is an emergent global centre subspace for the collection of cell-problems over the physical domain \mathbb{X} . Hence \mathbb{M} forms a centre subspace for the embedding PDE system [\(5.4\)](#) on \mathbb{X} .

In *linear* problems with *homogeneous macroscale* the ‘significant’ spectral gap may be small (e.g., [Section 6](#)): one may choose a sharp distinction between the so-called centre and stable modes. The reason is that in linear, macroscale-homogeneous, problems the macroscale modes do not interact and hence do not ‘fillin’ the gap. But in problems with *either nonlinear or macroscale-inhomogeneous* effects (e.g., [Section 4.5](#)), that we encompass here, the macroscale modes and/or variations interact to generate effects ‘within’ the gap. At high enough order these effects ‘cross’ the gap and cause troublesome small divisors, divisors that limit the order of approximation and the validity of the modelling. To avoid such small divisors one needs a gap big enough for the desired order of approximation.

The nonlinear theory of invariant manifolds for non-autonomous systems ²², subject to various caveats, asserts that under perturbation by nonlinearity and macroscale spatial modulation ($\nabla_{\mathbf{x}} \neq 0$) the qualitative nature of this linear picture is preserved throughout \mathbb{X} and \mathbb{E} . The theoretical support is summarised in the following [Propositions 9](#) and [10](#).

Proposition 9 (Forward Theory). *Under [Assumptions 5](#) and [8](#), and cell-eigenvalues as in [Figure 8](#), and when the cell-operator \mathfrak{L} generates a strongly continuous semigroup, then theorems apply, such as those of [Haragus & Iooss \(2011\)](#) [Ch. 2], [Aulbach & Wanner \(2000\)](#), and [Potzsche & Rasmussen \(2006\)](#), to underpin the application of the spatially slowly varying analysis and results of [Roberts \(2015a\)](#), [Bunder & Roberts \(2021\)](#) to autonomous cases of the embedding system (5.4). Further, if \mathfrak{L} is also bounded, then the extant theorems apply to non-autonomous cases of (5.4). Briefly, the results for the nonlinear embedding system (5.4) are the following.*

1. *There exists an M -mode centre manifold \mathcal{M} in some neighbourhood of the equilibria \mathbb{E} .*
2. *All solutions in the neighbourhood of \mathbb{E} are exponentially quickly attracted to solutions on \mathcal{M} (approximately like $e^{-\beta_f t}$).*
3. *If an approximation to \mathcal{M} and the evolution thereon (the homogenisation (5.2)) satisfies (5.4) to a residual of order $N+1$ in spatial gradients, nonlinearity, and γ , and provided N is constrained by the smoothness of $\mathcal{L}, \mathbf{f}, g$ and for nonlinear systems by the spectral gap $N+1 < \beta_f/\beta_s$, then the approximations have errors of the same order $N+1$.*

The three examples of [Sections 3](#), [4](#) and [6](#) all have self-adjoint linear operators for \mathfrak{L} that generate the required strongly continuous semigroup. Since they are also autonomous, the above properties hold for the constructed

²²(e.g., [Aulbach & Wanner 2000](#), [Potzsche & Rasmussen 2006](#), [Haragus & Iooss 2011](#), [Roberts 2015a](#), [Hochs & Roberts 2019](#), [Bunder & Roberts 2021](#))

approximations to their M -mode, M -continuum, homogenisations. Further, the example of [Section 6](#) is coded on a microscale lattice, has its cell-problem in a finite dimensional space, so \mathcal{L} is bounded, and consequently the above cited extant theory would also rigorously apply to time-dependent variations in the system. However, there are also many physical systems that do not satisfy the required preconditions for [Proposition 9](#) but do satisfy the less stringent preconditions of the following backward proposition.

Proposition 10 (alternate Backward Theory). *Under [Assumptions 5 and 8](#), and cell-eigenvalues as in [Figure 8](#), and when $\mathbb{H}_{\mathbb{D}}^N$ is a graded Frechet space and \mathcal{L} is a continuous linear operator on $\mathbb{H}_{\mathbb{D}}^N$ in the sense of [Hochs & Roberts \(2019\)](#), then the theory therein underpins the application of the spatially slowly varying analysis and results of [Roberts \(2015a\)](#), [Bunder & Roberts \(2021\)](#) to the embedding system [\(5.4\)](#). Briefly, the results are the following:*

1. *there exists a constructable smooth system close to the embedding system [\(5.4\)](#), close to within errors of order $N + 1$, an order constrained as in [Proposition 9](#);*
2. *which in a finite domain of state space containing \mathbb{E} exactly possesses the constructed M -mode centre manifold homogenisation [\(5.2\)](#); and*
3. *where the centre manifold homogenisation is exponentially quickly emergent (approximately like $e^{-\beta_f t}$).*

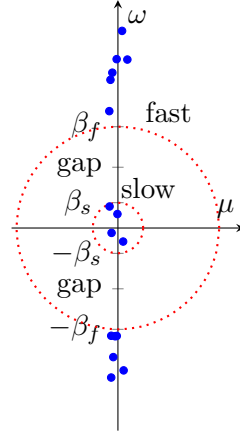
In these two propositions, the statements of order $N + 1$ errors and residuals justify the iterative construction algorithm described in the examples of [Sections 3, 4 and 6](#) and as implemented in the computer algebra code of [Appendices A to C](#).

In their review, [Fish et al. \(2021\)](#) [p.774] commented that in “providing a link between fine and coarse scales . . . the undertaking becomes challenging for heterogeneous systems, particularly for describing large deformation and failure of materials, which often involve history-dependent mechanisms.” Here we establish a framework and systematic construction whose proven supporting theory, such as these two propositions, encompasses nonlinear out-of-equilibrium modelling. Moreover, the approach often avoids the need for history-dependent mechanisms through a systematic approach to the extra kinematic variables of a multi-continuum micromorphic model.

5.2.3 Wave-like systems

Typical wave-like systems, like the elasticity homogenisation of [Section 6](#), have modal eigenvalues which are nearly pure-imaginary as illustrated schematically in [Figure 9](#). Two usual scenarios occur: firstly, first-order systems

Figure 9: schematic complex plane of cell-eigenvalues $\mu + i\omega$ (blue discs) in the case of wave-like dynamics when within each cell there are slow modes among fast oscillations. For small real-part μ : either $\lambda_m = \mu_m + i\omega_m$ when $\alpha = 1$; or alternatively $\pm\sqrt{\lambda_m} = \mu_m + i\omega_m$ when $\alpha = 2$. The cell-eigenvalues form two separate sets characterised by bounding parameters β_s and β_f of the slow and fast modes, respectively.



($\alpha = 1$) are dominantly wave-like when the cell-eigenvalues are themselves all nearly pure-imaginary; and secondly, [Figure 9](#) typically arises in the case of second-order wave systems ($\alpha = 2$). In the second-order case, the eigenvalues λ_m of the cell-problem [\(5.7\)](#) give rise to two linearly independent solutions of the modal ODE [\(5.8b\)](#), namely $a_m(t) = A_m e^{(\mu_m + i\omega_m)t} + B_m e^{-(\mu_m + i\omega_m)t}$ for $\mu_m + i\omega_m := \sqrt{\lambda_m}$. Commonly, for $\alpha = 2$, the cell-eigenvalues λ_m are all (nearly) real and negative and then dynamics corresponding to [Figure 9](#) arises for the mode solutions of [\(5.8b\)](#).

In these scenarios, the usual physical argument is that it is the relatively few cell-eigenvalues with small frequency ω_m that determine the long-time macroscale evolution. If so, then a rational multi-continuum model is formed by identifying a significant *gap* in the frequencies, such as that shown in [Figure 9](#). Physically, one would usually be aiming to resolve macroscale time variations longer than some minimum timescale of interest t_s , and so seek a gap with bounds $\beta_s < 1/t_s < \beta_f$. Identifying such a frequency gap identifies M *slow* cell-eigenvalues, as in [Figure 9](#), and for convenience suppose these eigenvalues correspond to $\lambda_0, \dots, \lambda_{M-1}$. But if appropriate for the physical application, then one may choose to include more sub-cell modes into the modelling as we allow here. The corresponding M cell-eigenfunctions v_0, \dots, v_{M-1} are M -microscale modes that form the basis of an M -D subspace $\mathbb{M}_{\mathbf{X}}$ of $\mathbb{H}_{\Theta \times \mathbb{Z}}$. The subspace $\mathbb{M}_{\mathbf{X}}$ is invariant for the linearisation of the cell-dynamics [\(5.6\)](#). Because the other cell-modes v_M, v_{M+1}, \dots , all oscillate faster than $e^{\pm i\beta_f t}$, within the linearised dynamics the invariant subspace $\mathbb{M}_{\mathbf{X}}$, called a *slow subspace*, is expected to act as a *guiding centre* for the nearby dynamics of the cell problem [\(5.6\)](#).²³ Since the eigenvalue bounds hold for all $\mathbf{X} \in \mathbb{X}$,

²³(e.g., [Munaster 1983b](#), [Lorenz 1986](#), [van Kampen 1985](#))

the union $\mathbb{M} := \cup_{\mathbf{X} \in \mathbb{X}} \mathbb{M}_{\mathbf{X}}$ is a global slow subspace for the collection of cell-problems over the physical domain \mathbb{X} . We expect \mathbb{M} to be a guiding centre for the embedding PDE system (5.4) (e.g., van Kampen 1985, §11).

For *linear* systems (5.4) the idea of a useful ‘guiding-centre’ slow subspace is usually sound (because of the simplicity of linear superposition of solutions).

However, for *nonlinear* systems (5.4) a corresponding ‘guiding-centre’ slow invariant manifold is very delicate. Sijbrand (1985) established some criteria for the existence of some subcentre manifolds. But there is a long running controversy in geophysics about the non-existence of slow manifolds.²⁴ Perhaps the most useful rigorous result²⁵ is the following corresponding version of the backwards theory Proposition 10 with some simple changes.

Proposition 11 (slow manifold). *Under Assumptions 5 and 8, and cell-eigenvalues as in Figure 9, and when $\mathbb{H}_{\mathbb{D}}^N$ is a graded Frechet space and \mathfrak{L} is a continuous linear operator on $\mathbb{H}_{\mathbb{D}}^N$ in the sense of Hochs & Roberts (2019), then the theory therein underpins the application of the spatially slowly varying analysis and results of Roberts (2015a), Bunder & Roberts (2021) to the embedding system (5.4). Briefly:*

1. *there exists a constructable smooth system close to the embedding system (5.4), close to within errors of order $N + 1$, an order constrained as in Proposition 9; and*
2. *which in a finite domain of state space containing \mathbb{E} exactly possesses the constructed M -mode slow manifold homogenisation (5.2).*

Moreover, a “guiding centre” is not the only justification for an M -mode, M -continuum model. Another justification for a slow manifold model is that it may be physically observable due to physical effects not encoded in the mathematics or computation. For example, one such physical mechanism is weak viscoelastic effects that damp out fast elastic waves. Another physical mechanism is that the fast waves may radiate out of the spatial domain \mathbb{X} of interest to leave the slow subspace within \mathbb{X} : for example, sound may radiate energy from a vibrating beam; and in the atmosphere fast inertial waves propagate up into the upper atmosphere and break there leaving the bulk of the atmosphere in a quasi-geostrophic slow manifold.

Two further scenarios within this case may be invoked. The first scenario is when the perturbation γg forces the system near some ‘fast’ natural frequency of the cell problem, and when the forcing overcomes (weak) dissipation or radiation out of \mathbb{X} of the corresponding ‘fast’ cell modes, then those fast

²⁴(e.g., Lorenz & Krishnamurthy 1987, Lorenz 1992, Boyd 1995, Bokhove & Shepherd 1996, Vanneste & Yavneh 2004)

²⁵(Introduced in §13.5 of the book by Roberts 2015b)

modes may be needed in a macroscale model (e.g., [Touze & Amabili 2006](#), [Touzé & Vizzaccaro 2021](#)). Two significant macroscale features are: firstly, the modulation of the fast mode; and secondly, the potential for nonlinear wave-wave resonance of the fast mode to drive mean ‘flow’ in the slow modes: an example is the large scale Stokes drift driven by relatively small scale ocean surface waves. However, existence and smoothness of such a model for nonlinear systems is highly problematic due to the likely plethora of nonlinear wave-wave (near) resonances with other cell-modes.

A second further scenario is either when the initial conditions are that of a near uniform small-wavelength wave, or when a localised physical initial condition together with wave dispersion combine to cause a near uniform small-wavelength in the spatial domain of interest. Then one wishes to focus purely on the one fast mode of the particular small wavelength mode, under the convenient but questionable assumption that other modes remain small. Here one would construct an invariant manifold describing the large-scale modulation of the wave from a linear base of the one mode, and via embedding the system in the ensemble of all phase-shifts of the wave ([Roberts 2015a](#), §2.5). Generally, the resulting models are variants of the so-called nonlinear Schrödinger PDE. The existence and smoothness of such a model is highly problematic due to potential nonlinear (near) resonances, but again backwards theory could assert there is a system close to that specified which exactly possesses the constructed invariant manifold. When the initial conditions possess multiple identifiable waves, then like the quasi-periodic cases herein, embedding the system in the ensemble of all phase-shifts independently should systematically lead to a model expressed in interacting nonlinear Schrödinger PDEs.

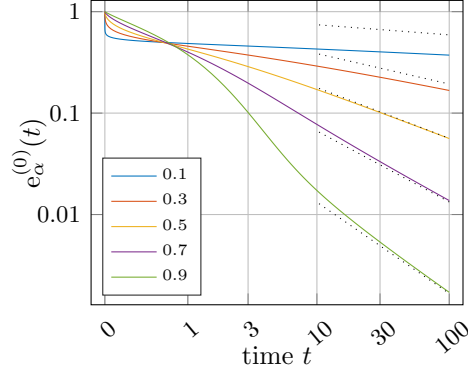
5.2.4 Fractional differential evolution

In this case let the time differential operator ∂_t^α for real fractional $\alpha \in (0, 2)$, $\alpha \neq 1$, be interpreted in the Caputo sense and implicitly from initial time $t = 0$. Let’s reconsider the general solution (5.8) for the linearised cell-problem (5.6). From the general solution (5.9) derived in [Appendix D](#), the general solution to the m th-mode fractional differential equation (FDE) (5.8b), $\partial_t^\alpha a_m = \lambda_m a_m$, is, in terms of parameter $\mu_m := (-\lambda_m)^{1/\alpha}$,

$$a_m(t) = C_{m0} e_\alpha^{(0)}(\mu_m t) + \begin{cases} 0, & 0 < \alpha < 1, \\ C_{m1} e_\alpha^{(-1)}(\mu_m t), & 1 < \alpha < 2. \end{cases} \quad (5.9)$$

The free constants C_{m0}, C_{m1} happen to be proportional to the derivatives at time zero: $C_{mk} \propto a_m^{(k)}(0^+)$. The functions $e_\alpha^{(0)}(t) := E_{\alpha,1}(-t^\alpha)$ and $e_\alpha^{(-1)}(t) := tE_{\alpha,2}(-t^\alpha)$ ([Appendix D](#)) in terms of the Mittag–Leffler function $E_{\alpha,\beta}(z) := \sum_{k=0}^{\infty} \frac{z^k}{\Gamma(\alpha k + \beta)}$ (e.g., [Gorenflo & Mainardi 1997](#), (A.1)).

Figure 10: For the FDE (5.8b), plot the general solution (5.9) component $e_\alpha^{(0)}(t)$ for five $\alpha \in (0, 1)$ (as in legend). The time axis is quasi-log via an asinh scaling of the axis, and so clearly shows the long-time algebraic decay of this component in the general solution. The dotted lines are the large time asymptotics (5.10).



Arguably, the most important aspect of the general solution (5.9) is its behaviour for large time in the most common case of real negative eigenvalues λ_m . In this case $\mu_m = (-\lambda_m)^{1/\alpha}$ is real and positive and we need only consider the general solution for real positive arguments to $e_\alpha^{(k)}$. Since $E_{\alpha,\beta}(z) \sim (-z)^{-1}/\Gamma(\beta - \alpha)$ as $|z| \rightarrow \infty$ with $|\arg(-z)| < \pi(1 - \alpha/2)$, Appendix D derives that $e_\alpha^{(k)}$ generically decay algebraically to zero:

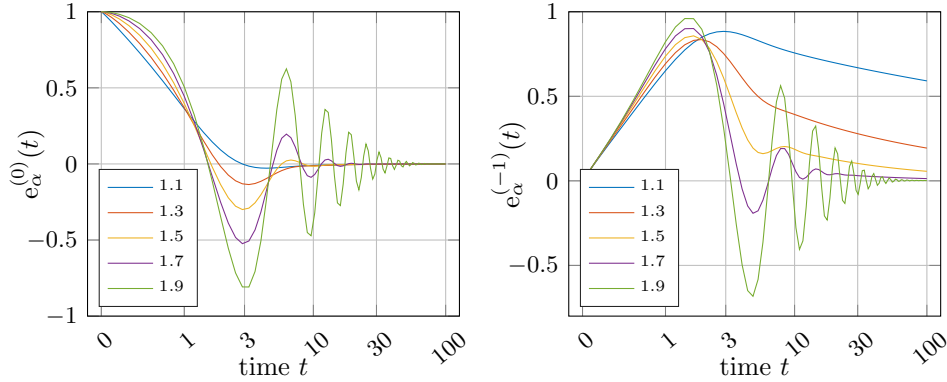
$$e_\alpha^{(0)}(t) \sim \frac{t^{-\alpha}}{\Gamma(1 - \alpha)}, \quad e_\alpha^{(-1)}(t) \sim \frac{t^{1-\alpha}}{\Gamma(2 - \alpha)}, \quad \text{as } t \rightarrow +\infty. \quad (5.10)$$

Figure 10 plots the numerically computed solution component $e_\alpha^{(0)}(t)$ for various $0 < \alpha < 1$ with the large-time approximations (5.10). The log-log nature of the plot clearly exhibits the long-time algebraic decay of this component of the general solution (5.9), with the decay and the approach to the asymptotes very slow for small α . For the larger case of $\alpha = 0.9$, $e_\alpha^{(0)}(t)$ exhibits exponential-like decay for small time, $t < 5$ —characteristic of the exponential decay for the ODE case of $\alpha = 1$ —before morphing to algebraic decay for larger times, $t > 10$.

For the higher range $1 < \alpha < 2$, Figure 11 plots the two solution components $e_\alpha^{(0)}(t)$ and $e_\alpha^{(-1)}(t)$. These components oscillate some number of times—the number of oscillations increase as $\alpha \rightarrow 2$ (the wave case)—before eventually morphing into the large time algebraic decay of the asymptotic (5.10).

Now let's address what the above means for modelling and/or homogenisation of general systems (5.1). The clearest case is for linear autonomous systems (5.1) and when the cell eigen-problem (5.7) has a robust spectrum, such as obtained from a self-adjoint cell-operator \mathfrak{L} . Then the modal FDEs (5.8b) are robust under perturbations by macroscale spatial gradients. Consequently, under such perturbations we expect each mode to still evolve roughly like $(-\lambda_m t)^{-\alpha-1+\hat{\alpha}}$ for large time, where $\hat{\alpha} := \lceil \alpha \rceil =$ nearest integer $\geq \alpha$, and provided $|\arg(-\lambda_m)| \leq \vartheta_{\max} < \pi(1 - \alpha/2)$ for some angle bound ϑ_{\max} . Because of the eigenvalue factor λ_m , the modes with large $|\lambda_m|$ decay the quickest,

Figure 11: For the FDE (5.8b), plots the two general solution (5.9) components for five $\alpha \in (1, 2)$ (see legend): (left) $e_\alpha^{(0)}(t)$; (right) $e_\alpha^{(-1)}(t)$. The time axis is quasi-log via an asinh scaling of the axis.



albeit with the same exponent. The result is that we reasonably expect that the large time evolution is dominated by the modes with small $|\lambda_m|$. Then, as in the exponential case of Section 5.2.2, we may reasonably construct and use a multi-modal, multi-continuum, homogenisation based upon choosing the M -modes with smallest $|\lambda_m|$.

The above argument reasonably justifies homogenisations such as (4.1), (4.5) and (4.6) for general fractional α .

However, nonlinearities and non-autonomous forcing complicates the situation. There is some extant theory of invariant manifolds for fractional differential systems (e.g., Cong et al. 2016, Ma & Li 2015), but none appears suitable to invoke for general systems (5.1). I conjecture that adapting proposed backwards theory (Roberts 2022, Hochs & Roberts 2019) would provide the most accessible route for supporting invariant manifold homogenisation of non-linear non-autonomous FDE systems. However, it remains to be established whether or not a given FDE system is generally ‘close’ to a diffeomorphism of a constructible FDE system which is in the separated canonical form.

5.2.5 Improving spatial resolution

Sections 5.2.2 to 5.2.4 focussed upon the scenario when one choose multi-modal multi-continua homogenisations based upon selecting those modes with the longest lifetime. But there is significant interest in scenarios where the prime motivation is to better resolve spatial structures. For two examples: Alavi et al. (2023) [p.2164] comment that “Enriched continuum theories are required in such situations to capture the effect of spatially rapid fluctuations at the mesoscopic and macroscopic levels”; and Somnic & Jo (2022) [p.8] wrote

“Classical continuum theory is not suitable when . . . high strain gradients are observed in the domain”. Hence this section discusses possibilities for choosing invariant manifold modes based upon the criterion of improving the spatial resolution irrespective of the time resolution.

Often the two criteria, spatial resolution and time resolution, are essentially equivalent. In that common case the previous discussions apply. This equivalence is generally the case for nonlinear systems because nonlinearity typically has mode interactions which spread the dynamical energy among all modes, and so all modes are generally excited. It is only in the special circumstance when the nonlinear system and the initial conditions preserve some symmetry that space and time resolutions are not necessarily equivalent. For example, in the nonlinear Burgers’ PDE $u_t = -uu_x + u_{xx}$ odd functions are preserved, so that if the initial conditions are odd, then cosine modes need not be included in a model, only sines.

However, in linear systems (most of [Sections 3, 4 and 6](#)) symmetries are more likely to be preserved. For example, in the multi-modal multi-continua modelling of shear dispersion along a channel [Watt & Roberts \(1995\)](#) found even modes across the channel interacted with the leading mean mode, but the odd modes did not. Consequently the two-mode bi-continua model based upon the leading two even modes has much improved spatial resolution, when compared to that of the leading order model, but no improvement of the temporal resolution because the two-even-mode model neglects the gravest odd-mode (which has the slowest decay rate). Quantitative estimates of the spatial resolution may be made for linear systems, [Section 3.2.2](#) for example, by constructing to 20th order or more in ∂_x , taking the Fourier transform which converts macroscale spatial derivatives to multiplication by the macroscale wavenumber k , that is, $\partial_x \equiv ik$. Then a Domb–Sykes plot ([Domb & Sykes 1957](#), [Hunter 1987](#), e.g.) or Mercer–Roberts plot ([Mercer & Roberts 1990](#), Appendix) for series’ in the wavenumber k predict the convergence limiting singularity in the complex k -plane, and hence the radius of convergence, say k_* . The minimum resolved wavelength by the model is then deduced to be $2\pi/k_*$.

One way to view an invariant manifold for linear systems is as a perturbation from the cell-problem [\(5.6\)](#) in small macroscale wavenumber k . A crucial characteristic of the modelling are the eigenvalues $\lambda(k)$ as a perturbative function of the wavenumber k . Let’s explore fascinating aspects of such a multi-mode, multi-continuum, homogenisation via the mathematical structure of perturbative eigenvalue problems (e.g., [Bender & Orszag 1981](#), §7.5).

The crucial property of eigenproblems for a given $n \times n$ matrix that is a function of a parameter k is that its eigenvalue function $\lambda(k)$ generally forms a single n -sheeted (Riemann) surface in complex k (e.g., [Bender & Orszag](#)

1981, p.350). Such an n -sheeted surface possesses various branch points at complex k that are necessary to connect the sheets together into a unified whole. Although, in some cases, often due to symmetries, the n -sheeted surface partitions into several disjoint sheeted surfaces. These properties also generalises to many PDE operators of interest in applications.

The branch points in the Riemann sheets are singularities that limit the convergence of the perturbative expansion for $\lambda(k)$ in wavenumber k , and hence limit the spatial resolution of the macroscale homogenisation. For example, the tri-continuum high-order homogenisation of Section 3.2.2 shows the eigenvalue sheet of the homogenisation, for small heterogeneity a , has pole singularities at real wavenumbers $k = \pm 3/2$, pole singularities that limit the resolution of the homogenisation in physical space. But the question is: which branch-points become limiting?

Using the developed rigorous framework and systematic procedure we may construct multi-modal multi-continua homogenisations to any chosen order. For linear systems, such an M -mode, M -continua homogenisation constructs a homogenisation whose eigenvalues λ form an M -sheeted Riemann surface as an analytic function, say $\lambda^M(k)$, of wavenumber k in the complex k -plane. The original system also has a many-sheeted analytic eigenvalue function $\lambda(k)$. The M -mode homogenisation approximates $\lambda(k)$ by analysing effects and interactions of the M chosen modes of the cell-problem—modes chosen from the eigenvalue spectrum at zero wavenumber (Section 5.2.1). The systematic construction guarantees that the perturbation series of $\lambda^M(k)$ is identical with that of the M chosen Riemann sheets of the original $\lambda(k)$. Consequently, we expect an M -mode homogenisation to encompass smoothly all branch-point singularities in the original $\lambda(k)$ that arise through interactions among the chosen M -modes (whether physical singularities at real k , or unphysical at complex valued k). Branch-point singularities in $\lambda(k)$ that occur, physically or not, due to interactions between the M -chosen modes and all the other unchosen modes cannot be captured in the M -mode homogenisation, and so it is these singularities that generally limit the radius of convergence of the M -continuum homogenisation. It is this limit in wavenumber k that then translates to a limit on the spatial macroscales accurately resolvable in a chosen M -mode, M -continuum homogenisation.

Consequently, to obtain the best macroscale spatial resolution in a multi-mode multi-continua homogenisation, without considering temporal resolution, one needs to select the M -modes that interact and form the *nearest* branch-points of the eigenvalue $\lambda(k)$ Riemann surface. However, such selection is usually difficult because commonly the near branch-point singularities are at unphysical complex-valued wavenumbers for no known physical reason.

Unless there are known physical symmetries, the best practical general guide to improve macroscale spatial resolution appears to be to select those modes with the longest time scale, as discussed in [Sections 5.2.2 to 5.2.4](#).

5.3 Construct a chosen invariant manifold multi-continuum homogenisation

The construction of multi-continuum homogenisation in multiple large spatial dimensions relies on theory proven by [Bunder & Roberts \(2021\)](#), which in turn rests on general theory by [Aulbach & Wanner \(2000\)](#), [Potzsche & Rasmussen \(2006\)](#), [Hochs & Roberts \(2019\)](#). One of the crucial theoretical results is that if a derived approximation satisfies the embedding PDE [\(5.4\)](#) to a residual of $\mathcal{O}(\partial_{\mathbf{x}}^{N+1})$, then the corresponding homogenisation is correct to an error $\mathcal{O}(\partial_{\mathbf{x}}^{N+1})$ ([Bunder & Roberts 2021](#), §3). This direct connection between residual and error follows on from earlier theory by [Potzsche & Rasmussen \(2006\)](#) on approximating inertial manifolds. In multi-D space, practical procedures to derive approximations to any chosen order of residual are in this section generalised from those of [Section 2.2.3](#) for 1-D space and from earlier developments ([Roberts 2015b](#), Part III).

For linear problems, the following may apply for a wide variety of time evolution operators ∂_t^α . However, to encompass nonlinear problems this section addresses the case of first-order time derivatives, $\alpha = 1$. For nonlinear systems with second-order time derivatives ($\alpha = 2$), introduce ‘velocity’ variables to rewrite the system as a larger system of first-order.

The general procedure is especially suitable for computer algebra ([Appendix C](#)) as applied for example to the homogenisation of 2-D heterogeneous elasticity ([Section 6](#)). For M selected modes ([Section 5.2](#)), define the vector of local amplitudes $\mathbf{U}(t, \mathbf{x}) := (U_0, \dots, U_{M-1})$. We seek an invariant manifold of the embedding PDE [\(5.4\)](#) in the form $\mathbf{u} = v(\mathbf{U}, t, \mathbf{x}, \boldsymbol{\theta})$ such that $\partial_t^\alpha \mathbf{U} = G(\mathbf{U}, t, \mathbf{x})$ where the right-hand side dependence upon \mathbf{U} implicitly involves its general gradients $\mathbf{U}_{x_i}, \mathbf{U}_{x_i x_j}, \dots$, and the explicit (t, \mathbf{x}) dependence are the slow, macroscale, variations arising from macroscale functional graduations in the problem. For any given approximations \tilde{v}, \tilde{G} to v, G , compute the residual of the embedding PDE [\(5.4\)](#), call it $\text{Res}(\tilde{v}, \tilde{G})$. Compute corrections v', G' to the approximations \tilde{v}, \tilde{G} by solving a variant of the cell problem [\(5.6\)](#), linearised and forced by the residual, called the *homological equation*²⁶,

$$\mathfrak{L}v' - \sum_{m=0}^{M-1} \frac{\partial v'}{\partial U_m} (\lambda_m U_m + \zeta_m U_{m+1}) - \sum_{m=0}^{M-1} v_m G'_m = \text{Res}(\tilde{v}, \tilde{G}). \quad (5.11)$$

²⁶(e.g., [Potzsche & Rasmussen 2006](#), [Roberts 2015b](#), [Siettos & Russo 2021](#), [Martin et al. 2022](#))

As in [Section 2.2.3](#), the factors $(\partial v' / \partial U_m) U_n$ have to be interpreted in the Calculus of Variations sense such that here it represents $v'_{U_m} U_n + \sum_i v'_{U_m x_i} U_{n x_i} + \sum_{i,j} v'_{U_m x_i x_j} U_{n x_i x_j} + \dots$ where these subscript-derivatives of v' are done with respect to the subscript symbol ([Roberts 1988](#)). Recall that ζ_m arises with generalised eigenmodes ([Assumption 8](#)). Differences in [\(5.11\)](#) from the usually used cell-problems arise in this systematic invariant manifold framework through accounting for the physical out-of-equilibrium effects. After solving [\(5.11\)](#) for v', G' , then update the approximations \tilde{v}, \tilde{G} , and iterate until the residual is of the order of the desired error.

Two practical simplifications are often feasible for solving the homological equation [\(5.11\)](#). Firstly, neglect the term in ζ_m arising from generalised eigenmodes. This neglect increases the number of required iterations by no more than a factor equal to the multiplicity of the eigenvalues. Secondly, when constructing nonlinear models to errors of order p in nonlinearity, provided the spectral gap (β_s, β_f) (see [Figures 8](#) and [9](#)) is big enough so that the ratio $\beta_f / \beta_s > p$ then one can neglect the term in λ_m as well. Thus, in practice one often determines updates by solving the simpler common homological equation²⁷

$$\mathfrak{L}v' - \sum_{m=0}^{M-1} v_m G'_m = \text{Res}(\tilde{v}, \tilde{G}). \quad (5.12)$$

The iterative updates are then not exact (unless $\beta_s = 0$), but the residual generally improves each iteration. One terminates the iteration when the coefficients in the residual are all smaller than some small numerical threshold such as 10^{-7} . The elasticity homogenisation code of [Appendix C](#) generally invokes both of these simplifications, and so solves [\(5.12\)](#) for updates.

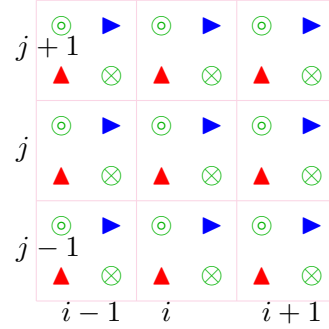
6 Example in 2D elasticity homogenisation

This section applies the approach of [Section 5](#) to rigorously construct and support a second-order in time, tri-continuum, three-mode, homogenisation of 2D elasticity for an example heterogeneous Young's modulus.

We adopt simple robust microscale equations for the heterogeneous 2-D elasticity. On the staggered microscale xy -grid of [Figure 12](#), of spacing δx and δy , define the displacements: \blacktriangleright , horizontal $u_{ij}(t)$; \blacktriangle , vertical $v_{ij}(t)$. The adopted

²⁷In essence, such neglect of $\sum_{m=0}^{M-1} (\partial v' / \partial U_m) \lambda_m U_m$ is equivalent to modifying the embedding PDE by adding to the right-hand side the term $(\epsilon - 1) \sum_{m=0}^{M-1} \lambda_m v_m \langle w_m, \cdot \rangle$. When this new parameter $\epsilon = 1$ we recover the original problem, but when $\epsilon = 0$ the corresponding homological equation is precisely the simpler [\(5.12\)](#). Then construct the invariant manifold as a high-order series in ϵ , terminating the order in ϵ whenever evaluation at $\epsilon = 1$ is accurate enough. In this type of context, such explicit modification was first done in modelling the nonlinear inertial dynamics of thin fluid flow ([Roberts 1996](#)).

Figure 12: a small part of the microscale grid, of spacing δx and δy , used to code 2-D elasticity. The grid is staggered on the microscale: \blacktriangleright , horizontal displacements and velocities; \blacktriangle , vertical displacements and velocities; \odot , \otimes , components of strain and stress tensor (6.1).



microgrid elasticity uses centred finite differences, δ_i and δ_j , to compute stresses at the shown microscale grid-points (Figure 12):

$$\otimes \quad \sigma_{ij}^{xy} := \mu_{ij} [\delta_i v_{ij} / \delta x + \delta_j u_{ij} / \delta y]; \quad (6.1a)$$

$$\odot \quad \sigma_{ij}^{xx} := (\lambda_{ij} + 2\mu_{ij}) \delta_i u_{ij} / \delta x + \lambda_{ij} \delta_j v_{ij} / \delta y; \quad (6.1b)$$

$$\odot \quad \sigma_{ij}^{yy} := \lambda_{ij} \delta_i u_{ij} / \delta x + (\lambda_{ij} + 2\mu_{ij}) \delta_j v_{ij} / \delta y, \quad (6.1c)$$

where λ_{ij}, μ_{ij} denote the heterogeneous Lamé parameters. Then centred finite differences compute the following (non-dimensional) acceleration ODEs

$$\blacktriangleright \quad \partial_t^2 u_{ij} = \delta_i \sigma_{ij}^{xx} / \delta x + \delta_j \sigma_{ij}^{xy} / \delta y, \quad (6.2a)$$

$$\blacktriangle \quad \partial_t^2 v_{ij} = \delta_i \sigma_{ij}^{xy} / \delta x + \delta_j \sigma_{ij}^{yy} / \delta y. \quad (6.2b)$$

The Lamé parameters which appear in the stresses (6.1) are defined as

$$\lambda_{ij} := \frac{\nu_{ij} E_{ij}}{(1 + \nu_{ij})(1 - 2\nu_{ij})}, \quad \mu_{ij} := \frac{E_{ij}}{2(1 + \nu_{ij})}, \quad (6.3)$$

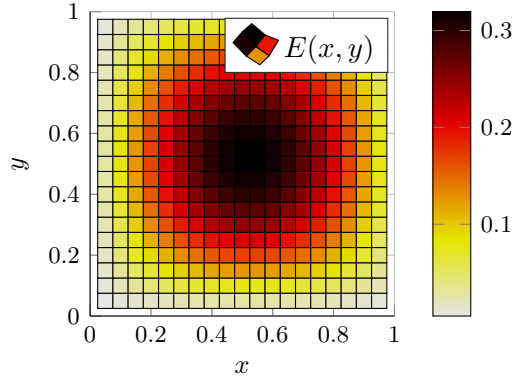
in terms of Young's modulus E_{ij} and Poisson ratio ν_{ij} .

6.1 Example cell problem

Suppose the microscale heterogeneity is reflected in the Lamé parameters λ_{ij} and μ_{ij} being n_x -periodic in i and n_y -periodic in j . That is, the material is $\ell_x := n_x \delta x$ periodic in the x -direction and $\ell_y := n_y \delta y$ periodic in the y -direction.

We choose to non-dimensionalise on the microscale cell size, choosing the length scale so that each cell is 1-periodic in x, y . Figure 13 plots one such non-dimensional microscale cell of the example Young's modulus used herein for the case reported here with $n_x = n_y = 10$. The material is made up of these cells repeating indefinitely in the xy -plane. This microscale heterogeneity is similar to the §§3–5 example of Sarhil et al. (2024) (diagrams phase-shifted in each cell). The homogenisation model then describes the

Figure 13: example of one period, one cell, of the 2-D microscale heterogeneity in the Young's modulus $E = [0.01 + |\sin(\pi x) \sin(\pi y)|]/\pi$. The non-dimensionalised microscale periods are $\ell_x = \ell_y = 1$.



evolution of elastic waves which have wavelengths significantly larger than one; that is, in this non-dimensionalisation the macroscale wavenumbers are those significantly less than 2π .

The general basic cell-problem (5.6) is here to solve the heterogeneous system (6.1) and (6.2) on a cell with periodic boundary conditions as justified by Section 6.2. But we obtain a preliminary physical understanding of general cell solutions by exploring the eigenvalues and eigenvectors of the cell eigenproblem (5.7) corresponding to the physical (6.1) and (6.2).

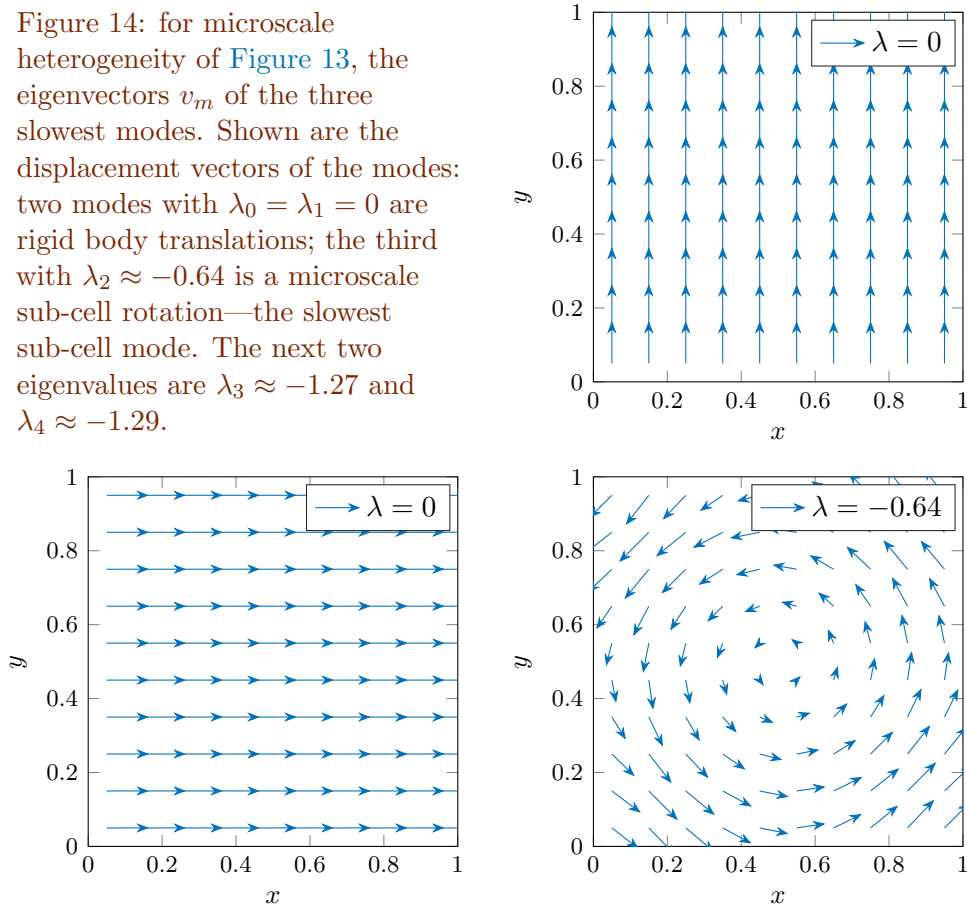
For the particular example of Figure 13, with microgrid $n_x = n_y = 10$ in each cell, Appendix C computes the 128×128 Jacobian matrix J of the right-hand side of the elasticity equations (6.2), and then computes its eigenvalues and eigenvectors. The smallest five eigenvalues are $\lambda_0 = \lambda_1 = 0$, $\lambda_2 = -0.6431$, $\lambda_3 = -1.2653$, $\lambda_4 = -1.2886$, \dots Figure 14 plots the displacement fields of the eigenvectors corresponding to the three smallest eigenvalues.

To form a macroscale model to be valid all times-scales longer than some threshold, in this problem with second-order derivatives in time, we must resolve all waves with corresponding period longer than the threshold, that is, with frequencies smaller than some threshold. In this non-dimensional example, the frequencies of the waves, $\omega_m = \sqrt{-\lambda_m}$, corresponding to the computed spectral modes (Figure 14) are $\omega_0 = \omega_1 = 0$, $\omega_2 = 0.8019$, $\omega_3 = 1.1248$, $\omega_4 = 1.1352$, \dots

- The usual homogenisation model is based upon averaging over a cell, and these averages are usually done with a *constant* weight function. Such constant weights implicitly correspond to the two sub-cell uniform displacement eigenvectors of Figure 14.

In the multi-continuum framework proposed and developed herein, we arrive at the same basis as the usual homogenisation, but by a different rationale (Section 5.2.3). The rationale is to choose to resolve all dynamics with a timescale longer than some threshold, say we choose a

Figure 14: for microscale heterogeneity of Figure 13, the eigenvectors v_m of the three slowest modes. Shown are the displacement vectors of the modes: two modes with $\lambda_0 = \lambda_1 = 0$ are rigid body translations; the third with $\lambda_2 \approx -0.64$ is a microscale sub-cell rotation—the slowest sub-cell mode. The next two eigenvalues are $\lambda_3 \approx -1.27$ and $\lambda_4 \approx -1.29$.



threshold approximately 5. Then we base our modelling on all sub-cell modes with frequencies smaller than $1/5 = 0.2$ (roughly). Here the two ‘rigid body’ cell-modes of Figure 14 corresponding to $\omega_0 = \omega_1 = 0$ are the only modes with frequency $\omega_m < 0.2$. Hence we would choose a bi-continuum two-mode model. In such a macroscale model, these two sub-cell modes are modulated over the macroscale of many cells. The homogenisation describes such macroscale modulation.

- However, observe that here the third frequency $\omega_2 \approx 0.8$ is separated by a gap from the higher frequencies $\omega_3, \omega_4, \dots \geq 1.1$ (albeit only a small gap). Hence, if we choose to want to resolve dynamics on a timescale longer than the smaller threshold of 1.0 say, then we should choose a homogenisation based upon the *three* sub-cell modes of smallest frequency. The third mode, plotted in Figure 14, corresponds to rotations of the ‘hard’ core in the centre of each cell (Figure 13). In the

macroscale modelling, this third mode represents the relatively slow vibration of such sub-cell rotations and how they interact and evolve over a large spatial domain.

This three-mode tri-continuum homogenisation is the example choice that we develop here, and the result is a rigorous homogenisation for the macroscale wave dynamics.

- We could choose more ‘slowest’ modes to form a multi-continuum homogenisation with more modes characterising the dynamics of more microscale physics.

6.2 Phase-shift embedding of the 2D heterogeneity

As in previous sections, a multi-continuum homogenisation is rigorously achieved via embedding the physical system in the ensemble of all phase-shifts of the heterogeneity. The embedding of (6.1) and (6.2) is done by considering horizontal displacement field $\mathbf{u}_{ijkl}(t)$ on a 4-D ‘spatial’ lattice in $xy\theta\phi$ -space, and similarly for the other fields $\mathbf{v}, \sigma^{xx}, \sigma^{xy}, \sigma^{yy}$. For simplicity, let the sub-cell lattice spacings $\delta\theta = \delta x$ and $\delta\phi = \delta y$. Then the spatial domain for the 4-D lattice is $\mathbb{R}^2 \times [0, \ell_x) \times [0, \ell_y)$, with all fields ℓ_x, ℓ_y -periodic in θ, ϕ respectively. In terms of the shift operator E_i defined so that $E_i^r \mathbf{u}_{ijkl} := \mathbf{u}_{i+r,jkl}$ and similarly for j, k, l , define the centred difference operator

$$\bar{\delta}_{pq} := E_p^{\frac{1}{2}} E_q^{\frac{1}{2}} - E_p^{-\frac{1}{2}} E_q^{-\frac{1}{2}}, \quad \text{for } p, q \in \{i, j, k, l\}, \quad (6.4)$$

which is a centred difference along diagonals in the $ijkl$ -lattice. Then consider the following system that embeds (6.1) and (6.2):

$$\otimes \quad \sigma_{ijkl}^{xy} := \mu_{kl} [\bar{\delta}_{jl} \mathbf{u}_{ijkl} / \delta y + \bar{\delta}_{ik} \mathbf{v}_{ijkl} / \delta x]; \quad (6.5a)$$

$$\odot \quad \sigma_{ijkl}^{xx} := (\lambda_{kl} + 2\mu_{kl}) \bar{\delta}_{ik} \mathbf{u}_{ijkl} / \delta x + \lambda_{kl} \bar{\delta}_{jl} \mathbf{v}_{ijkl} / \delta y; \quad (6.5b)$$

$$\odot \quad \sigma_{ijkl}^{yy} := \lambda_{kl} \bar{\delta}_{ik} \mathbf{u}_{ijkl} / \delta x + (\lambda_{kl} + 2\mu_{kl}) \bar{\delta}_{jl} \mathbf{v}_{ijkl} / \delta y; \quad (6.5c)$$

$$\blacktriangleright \quad \partial_t^2 \mathbf{u}_{ijkl} = \bar{\delta}_{ik} \sigma_{ijkl}^{xx} / \delta x + \bar{\delta}_{jl} \sigma_{ijkl}^{xy} / \delta y; \quad (6.5d)$$

$$\blacktriangle \quad \partial_t^2 \mathbf{v}_{ijkl} = \bar{\delta}_{ik} \sigma_{ijkl}^{xy} / \delta x + \bar{\delta}_{jl} \sigma_{ijkl}^{yy} / \delta y. \quad (6.5e)$$

By the form of the embedding (6.5) every solution $\mathbf{u}_{ijkl}(t), \mathbf{v}_{ijkl}(t)$ to (6.5) gives rise to solutions of the original physical system (6.1) and (6.2), for every phase-shift of the elasticity parameters. To see this, for every k', l' define $u'_{ij} := \mathbf{u}_{ij, i+k', j+l'}$ and similarly for the other fields. Then (6.5), satisfied by $\mathbf{u}_{ijkl}(t), \mathbf{v}_{ijkl}(t)$, reduces to the original (6.1) and (6.2) for u'_{ij} with Lamé parameters λ_{ij}, μ_{ij} replaced by their phase shifts $\lambda_{i+k', j+l'}, \mu_{i+k', j+l'}$. In particular, for $k' = l' = 0$ this defined u'_{ij} , with corresponding other fields, satisfies the original (6.1) and (6.2).

Similarly, an ensemble of all solutions to the ensemble of phase-shifted problems (6.1) and (6.2) forms a solution to the embedding (6.5). That is, the embedding system (6.5), homogeneous in x, y , is equivalent to the ensemble of phase-shifts of the given heterogeneous system (6.1) and (6.2).

6.3 Basis of invariant manifolds

The invariant manifold, multi-continuum, micromorphic, framework wraps around whatever microscale code a user supplies—here it is the embedded microscale system (6.5). The 4-D lattice system (6.5) is not a PDE, nonetheless the same framework (5.6) of Section 5.2.1 applies. The reason is that the operators and functions in the general form (5.6) may be microscale-nonlocal in space (Roberts 2021). Indeed, extant forward theory of invariant manifolds²⁸ is easier to apply to such spatially discrete systems as, crucially, the difference operators are *bounded*, whereas the usual alternative of spatial derivatives are troublesome because derivatives are unbounded operators.

In the practical construction of invariant manifold models (Appendix C), the spatial differences may be written in terms of shift operators when convenient (as in (6.5)), or equivalent differential operators when that is convenient.

For macroscale modelling of homogenised dynamics, the valid scenarios are that variations in x, y are slow in some useful sense. The *basis* of the modelling is the case where there are effectively no variations in x, y , hence the microscale shifts $E_i \mathbf{u}_{ijkl} \approx \mathbf{u}_{ijkl}$ and similarly for all fields, that is, $E_i, E_j \mapsto 1$. In this base case, the centred difference operators $\bar{\delta}_{ik} \mapsto \delta_k$ and $\bar{\delta}_{jl} \mapsto \delta_l$. Consequently, in this base case, at each and every cross section, parametrised by x, y or equivalently indexed by i, j which I omit for brevity, the embedding system (6.5) reduces to the cell-problem

$$\otimes \sigma_{kl}^{xy} := \mu_{kl} [\delta_k \mathbf{v}_{kl} / \delta x + \delta_l \mathbf{u}_{kl} / \delta y]; \quad (6.6a)$$

$$\odot \sigma_{kl}^{xx} := (\lambda_{kl} + 2\mu_{kl}) \delta_k \mathbf{u}_{kl} / \delta x + \lambda_{kl} \delta_l \mathbf{v}_{kl} / \delta y; \quad (6.6b)$$

$$\odot \sigma_{kl}^{yy} := \lambda_{kl} \delta_k \mathbf{u}_{kl} / \delta x + (\lambda_{kl} + 2\mu_{kl}) \delta_l \mathbf{v}_{kl} / \delta y; \quad (6.6c)$$

$$\blacktriangleright \partial_t^2 \mathbf{u}_{kl} = \delta_k \sigma_{kl}^{xx} / \delta x + \delta_l \sigma_{kl}^{xy} / \delta y; \quad (6.6d)$$

$$\blacktriangle \partial_t^2 \mathbf{v}_{kl} = \delta_k \sigma_{kl}^{xy} / \delta x + \delta_l \sigma_{kl}^{yy} / \delta y. \quad (6.6e)$$

All fields are to be n_x, n_y -periodic in k, l , respectively. Section 6.1 discusses this cell problem. In summary, we know a general solution of (6.6) is a linear combination of modes with frequencies $\omega_0 \leq \omega_1 \leq \omega_2 \leq \dots$. For a homogenised model we choose to focus on the dynamics of the longest time-scales, that is the dynamics with the smallest frequencies. Here we make the *multi-continuum* choice of focussing upon the *three* modes of lowest frequency. As plotted in Figure 14, here these are two simple translation

²⁸(e.g., Carr 1981, Bates et al. 1998, Aulbach & Wanner 2000, Chekroun et al. 2015)

modes and one sub-cell rotational mode. The corresponding tri-continuum homogenisation is constructed as the invariant manifold of (6.5) that is a regular perturbation from this base, a regular perturbation that accounts for large length-scale modulation across the cells in the x, y variables.

6.4 Construct multi-continuum homogenisations

The computer algebra of Appendix C constructs multi-modal, multi-continuum homogenisations for this example of 2-D elasticity. One chooses and sets the desired number of modes M , and the desired order of error in macroscale gradients N . We discuss three cases all constructed by the one code.

6.4.1 Classic 2-D homogenisation

Here base the homogenisation upon the two zero frequencies $\omega_1 = \omega_2 = 0$ of the two eigenvalues $\lambda_0 = \lambda_1 = 0$. One correspondingly sets the choice $M = 2$ in the construction code of Appendix C. The two amplitudes, order-parameters, macroscale variables U_0, U_1 are here defined to be the average over a cell of the x, y -direction displacements, respectively. These variables are *not* defined like this because cell-averaging is assumed in the modelling because here there is no such assumption. Instead, we *choose* U_0, U_1 to measure cell-averages because the physics of macroscale conservation laws are often best expressed via *unweighted* spatial integrals, and so the effects of such conservation laws are best seen with macroscale amplitudes which are themselves unweighted integrals/sums over the material cells.²⁹

With $M = 2$ modes, Appendix C constructs a slow invariant manifold here to be $(\mathbf{u}, \mathbf{v}) = v_0(\theta, \phi)U_0(t, x, y) + v_1(\theta, \phi)U_1(t, x, y) + \dots$ in terms of the two leading eigenvectors v_0, v_1 plotted in Figure 14, and where the ellipsis represents some computed corrections in gradients of U_0, U_1 which for simplicity are not recorded here. As in Section 5.1, such an invariant manifold of the phase-shifted embedding problems leads to the spatial displacement fields of the original problem as $(u, v) = v_0(x, y)U_0(t, x, y) + v_1(x, y)U_1(t, x, y) + \dots$. The evolution of the amplitudes U_0, U_1 then give the homogenisation: to three decimal places it is

$$\frac{\partial^2 U_0}{\partial t^2} = 0.144 \frac{\partial^2 U_0}{\partial x^2} + 0.020 \frac{\partial^2 U_0}{\partial y^2} + 0.092 \frac{\partial^2 U_1}{\partial x \partial y} + \mathcal{O}(\partial_x^3 + \partial_y^3), \quad (6.7a)$$

$$\frac{\partial^2 U_1}{\partial t^2} = 0.020 \frac{\partial^2 U_1}{\partial x^2} + 0.144 \frac{\partial^2 U_1}{\partial y^2} + 0.092 \frac{\partial^2 U_0}{\partial x \partial y} + \mathcal{O}(\partial_x^3 + \partial_y^3). \quad (6.7b)$$

²⁹Although strictly, in this framework, the two macroscale variables U_0, U_1 are averages of \mathbf{u} across all phase-shifts θ, ϕ of the heterogeneity.

The symmetry of the heterogeneous cells in the x, y -directions (e.g., [Figure 13](#)) results in the symmetry in coefficients apparent in the homogenisation (6.7). However, the coupled macroscale wave-PDEs (6.7) are anisotropic due to the square cells distinguishing the various directions. This anisotropic effective material is evident when we write (6.7) in stress-divergence form:

$$\begin{aligned} \partial_t^2(U_0, U_1) &\approx \nabla^T \bar{\sigma}, \quad \text{for} & \bar{\sigma}^{xx} &= (\bar{\lambda}_1 + 2\bar{\mu})U_{0x} + \bar{\lambda}_2 U_{1y}, \\ \bar{\sigma}^{xy} &= \bar{\mu}(U_{1x} + U_{0y}), & \bar{\sigma}^{yy} &= \bar{\lambda}_2 U_{0x} + (\bar{\lambda}_1 + 2\bar{\mu})U_{1y}, \end{aligned}$$

for effective material constants $\bar{\mu} = 0.020$, $\bar{\lambda}_1 = 0.105$, $\bar{\lambda}_2 = 0.072$. That $\bar{\lambda}_1 \neq \bar{\lambda}_2$ reflects the anisotropy of the square cells.

Our dynamical systems approach empowers us to improve such a basic homogenisation by accounting for more sub-cell physics. The next [Sections 6.4.2](#) and [6.4.3](#) describe two different analytic ways to do so.

Quantitatively estimate errors The asymptotic errors $\mathcal{O}(\partial_x^3 + \partial_y^3)$ in PDEs (6.7), as also for the errors in (6.8) and (6.9), could be quantitatively estimated. [Roberts & Bunder \(2017\)](#) developed a general mathematical theory for reduced-order multiscale modelling and homogenisation in multiple spatial dimensions, and their expression (52) is an explicit novel general formula for the remainder error that applies to (6.7). However, the expression is sufficiently complicated that we leave this aspect for further research.

6.4.2 Higher-order homogenisation

It is straightforward in this framework to proceed to higher-order in macroscale spatial derivatives—a more rigorous route to the second-gradient homogenisation heuristics of [Forest & Trinh \(2011\)](#) [§2]. Such higher-orders account for more physical interactions in the sub-cell dynamics and how these affect the evolution over the macroscale. Physically, higher-order wave PDEs accurately predict the dispersion in the macroscale waves.

For example, [Appendix C](#) readily constructs the fourth-order model, here reported to two significant digits, and neglecting terms with numerically small coefficients < 0.001 :

$$\begin{aligned} \frac{\partial^2 U_0}{\partial t^2} &= 0.144 \frac{\partial^2 U_0}{\partial x^2} + 0.020 \frac{\partial^2 U_0}{\partial y^2} + 0.092 \frac{\partial^2 U_1}{\partial x \partial y} \\ &\quad + 0.0037 \frac{\partial^4 U_0}{\partial x^4} + 0.0042 \frac{\partial^4 U_0}{\partial x^2 \partial y^2} + 0.0042 \frac{\partial^4 U_1}{\partial x \partial y^3} + \mathcal{O}(\partial_x^5 + \partial_y^5) \\ &\hspace{15em} (6.8a) \\ \frac{\partial^2 U_1}{\partial t^2} &= 0.020 \frac{\partial^2 U_1}{\partial x^2} + 0.144 \frac{\partial^2 U_1}{\partial y^2} + 0.092 \frac{\partial^2 U_0}{\partial x \partial y} \end{aligned}$$

$$+ 0.0037 \frac{\partial^4 U_1}{\partial y^4} + 0.0042 \frac{\partial^4 U_1}{\partial x^2 \partial y^2} + 0.0042 \frac{\partial^4 U_0}{\partial x^3 \partial y} + \mathcal{O}(\partial_x^5 + \partial_y^5) \quad (6.8b)$$

The fourth-order derivative terms on the second lines in (6.8a) and (6.8b) characterise the physics of macroscale wave dispersion in the homogenised model of this heterogeneous material.

6.4.3 Tri-continuum homogenised model

The alternative way to account for more physical interactions in the sub-cell dynamics is to retain more sub-cell modes to form a multi-continuum model. For this example, we choose to retain the gravest three modes.

Here the three modes correspond to eigenvalues $\lambda_0 = \lambda_1 = 0$ and $\lambda_2 = -0.3132$, separated from all the other eigenvalues headed by $\lambda_3 = -0.5601$. Figure 14 plots the physical structure of the three eigenmodes corresponding to these three gravest eigenvalues. The three eigenmodes are two of displacement in x, y -directions, and a sub-cell mode representing rotation of the ‘hard’-centre of each cell. Importantly, these modes are *not* assumptions we enforce onto the physics, instead these are modes that the sub-cell physics informs us *are the appropriate* sub-cell structures.

With $M = 3$, Appendix C constructs a slow invariant manifold here to be $(\mathbf{u}, \mathbf{v}) = v_0(\theta, \phi)U_0(t, x, y) + v_1(\theta, \phi)U_1(t, x, y) + v_2(\theta, \phi)U_2(t, x, y) + \dots$ in terms of the three leading eigenvectors v_0, v_1, v_2 plotted in Figure 14, and where the ellipsis represents some computed corrections in gradients of U_0, U_1, U_2 which for simplicity are not recorded here. To two significant digits, and neglecting terms with numerically small coefficients < 0.001 , the correspondingly constructed three-mode, tri-continuum, second-order homogenised evolution is governed by the following PDEs:

$$\begin{aligned} \frac{\partial^2 U_0}{\partial t^2} &= 0.144 \frac{\partial^2 U_0}{\partial x^2} + 0.020 \frac{\partial^2 U_0}{\partial y^2} + 0.092 \frac{\partial^2 U_1}{\partial x \partial y} \\ &\quad + 0.0021 \frac{\partial^2 U_2}{\partial x^2} - 0.0024 \frac{\partial^2 U_2}{\partial x \partial y} + \mathcal{O}(\partial_x^3 + \partial_y^3), \end{aligned} \quad (6.9a)$$

$$\begin{aligned} \frac{\partial^2 U_1}{\partial t^2} &= 0.020 \frac{\partial^2 U_1}{\partial x^2} + 0.144 \frac{\partial^2 U_1}{\partial y^2} + 0.092 \frac{\partial^2 U_0}{\partial x \partial y} \\ &\quad + 0.0021 \frac{\partial^2 U_2}{\partial y^2} - 0.0024 \frac{\partial^2 U_2}{\partial x \partial y} + \mathcal{O}(\partial_x^3 + \partial_y^3), \end{aligned} \quad (6.9b)$$

$$\begin{aligned} \frac{\partial^2 U_2}{\partial t^2} &= -0.643 U_2 + 0.0032 \left(\frac{\partial^2 U_0}{\partial x^2} + \frac{\partial^2 U_1}{\partial y^2} \right) - 0.0023 \frac{\partial^2 (U_0 + U_1)}{\partial x \partial y} \\ &\quad - 0.031 \left(\frac{\partial^2 U_2}{\partial x^2} + \frac{\partial^2 U_2}{\partial y^2} \right) + \mathcal{O}(\partial_x^3 + \partial_y^3). \end{aligned} \quad (6.9c)$$

The above is a mathematically and physically rigorous tri-continuum model for the homogenised dynamics.

As well as resolving shorter time scales than (6.7) and (6.8), this three-mode tri-continuum homogenisation contributes to the wave dispersion resolved by the fourth-order model (6.8). Use a quasi-adiabatic, quasi-static, approximation to the rotational mode (6.9c), that $0 \approx -0.64 U_2 + 0.0032(U_{0xx} + U_{1yy}) - 0.0023(U_{0xy} + U_{1xy})$, to thence deduce the sub-cell rotational amplitude $U_2 \approx +0.0049(U_{0xx} + U_{1yy}) - 0.0035(U_{0xy} + U_{1xy})$, in terms of the local curvatures of the macroscale mean displacements U_0, U_1 . Substituting this into (6.9a) and (6.9b) leads to fourth-order terms in the form of (6.8). This contribution does not complete the fourth-order terms in (6.8) because, to be consistent, the PDEs (6.9a) and (6.9b) should also have their fourth-order terms constructed as in Section 6.4.2. Physically, that this quasi-adiabatic approximation does not generate any second-order effects in the displacements thus indicates that here there is a relatively weak interaction from sub-cell rotation back into the two principal displacement modes. The significance of this tri-continuum homogenisation is that it is valid on shorter timescales than the bi-continuum (6.7) and (6.8), and potentially on shorter length-scales.

7 Conclusion

This article develops a novel, systematic, rigorous and practical approach of creating multi-continuum, micromorphic, macroscale homogenisations of microscale heterogeneity in mechanics. Sections 2 to 4 develops the basics of the approach in 1-D space, whereas Sections 5 and 6 addresses the complexities of general nonlinear systems in multi-D space underpinned by nonlinear dynamical systems theory.

An outstanding issue for multi-continua homogenisation is to decide on a suitable set of microscale structures. Here the proposed rationale (Sections 2.2.1, 5.2.2 and 5.2.3) is to choose to retain modes slower than a chosen threshold—a threshold selected according to the time-scales required for the intended application. An alternative is to choose modes according to the required space-scales of the application (Section 5.2.5). In many cases these two rationale are more-or-less equivalent. But sometimes, due to physical or geometric symmetries, the two rationale are different enough to justify a different set of modes for each scenario. The systematic approach developed here simplifies considerably much of the previous difficulty in choosing an appropriate model for a given microstructure.

The approach encompasses the homogenisation of nonlinear systems because it uses nonlinear dynamical systems theory. Sections 3.3 and 4.5 discuss two examples.

Section 4.5 illustrates two important aspects in modelling or homogenising nonlinear systems: the nature of the time evolution operator ∂_t^α significantly affects the homogenisation through significant changes in the algebra; and one requires a bigger spectral gap than that needed for linear systems.

The theory and results are *not* limited to the scale separation that the macro:macro scale ratios $\ell/L \rightarrow 0$ (Sections 2 and 5). The theory and results apply at finite scale separation of real physics and engineering applications (e.g., Section 6). Indeed our systematic dynamical systems framework, coupled with high-order computer algebra, may predict a sharp quantitative limit to the spatial resolution of an homogenisation (e.g., Section 3.2.2).

Section 4.3 verifies that our sound approach to modelling is transitive: the slow manifold homogenisation of a two-mode bi-continuum homogenisation of some physical system is the same as the slow manifold homogenisation of the physical system.

A further advantage of this nonlinear dynamical systems approach to homogenisation is that the associated theory and methods provides a sound rationale for correctly modelling initial conditions and boundary conditions for the homogenisation. The issue of initial conditions and boundary conditions is trivialised by the mathematical scale separation limit “ $\ell/L \rightarrow 0$ ”, but is nontrivial at the finite scale separation of real applications. Methodology to construct the correct initial conditions for a reduced order models are based upon solving a dual problem (Roberts 2000, 1989). These methods then generalise to potentially provide correct boundary conditions for the homogenisation variables (Roberts 1992), as explored for some elasticity examples (Roberts 1993, Chen et al. 2018). Future research is needed to develop these techniques to encompass the scenarios addressed in this article, and thus to complete the homogenisation task.

The projection of initial conditions will also inform a user of how to project forcing and uncertainty into an homogenisation (e.g., Roberts 2015b, §12.4).

Acknowledgements I thank colleagues Judy Bunder, Pavel Bedrikovetsky, Yannis Kevrekidis, and Thien Tran-Duc for their encouragement, and Arthur Norman and colleagues who maintain and develop the computer algebra software Reduce. The Australian Research Council Discovery Project grant DP220103156 helped support this research.

A Computer algebra construction

This Reduce-algebra code constructs any chosen multi-continuum, micro-morphic, invariant manifold homogenisation of heterogeneous diffusion (2.1) discussed by Section 3. Define main parameters:

```
15 mm:=3;      % modes M in the multi-continuum model, must be odd
16 theCase:=1;% selects error  $\mathcal{O}(d/dx^N, a^P)$  from following  $\{N,P\}$ 
17 cases:={ {3,3},{5,5},{3,21},{21,4},{3,31},{31,4} }$
```

Non-dimensionalise the problem so the heterogeneity is 2π -periodic—a variety of nonlinear trigonometric dependence is possible, but here code (3.1). The ‘strength’ of the heterogeneity must be parametrised by variable a . Throughout, let q denote θ .

```
25 kappa:=1/(1+a*cos(q));
```

Optionally, introduce heterogeneous nonlinearity (3.6) and (3.7) and set order of nonlinear error: here $\mathcal{O}(\gamma^2)$ would resolve quadratic terms.

```
32 let gamma^2=>0;
33 eta:=c1*cos(q)+c2*sin(2*q);
34 if gamma neq 0 then factor gamma;
```

Example high-order computation times are the following ($\gamma = 0$): case 3, {3,21}, uses 23 iterations in 20 secs; case 5, {3,31}, uses 33 iterations in 155 secs; case 4, {21,4}, uses 24 iterations in 2 secs; case 6, {31,4}, uses 34 iterations in 3 secs. That is, it terminates in $N + P - 1$ iterations.

Extract the orders of error from the case.

```
46 ordd:=part(cases,theCase,1); % order error in d/dx
47 orda:=part(cases,theCase,2); % order error in heterogeneity a
```

Improve formatting of written output:

```
51 on div; off allfac; on revpri;
52 factor d,df,uu;
```

Write approximations to the slow manifold homogenisation of the embedding PDE (2.4), such as (3.3) and (3.9), in terms of ‘modal’ fields $U_i(t, x)$, denoted by $uu(i)$, that evolves according to $\partial U_i / \partial t = dudt(i)$ for whatever approximation $dudt(i)$ contains.

```
62 array dudt(mm-1);
63 operator uu; depend uu,x,t;
64 let { df(uu(~i),t)=>dudt(i)
65      , df(uu(~i),t,x)=>df(dudt(i),x)
66      , df(uu(~i),t,x,2)=>df(dudt(i),x,2)
67      };
```

A.1 Iteration systematically constructs multi-modal model

We iteratively construct the improved homogenizations (3.4), (3.5) and (3.9). Recall that parameters `ordd` and `orda` specify the orders of error.

```

80 write "
81 Second, Iteratively Construct
82 -----";
83 maxit:=99;

Expand diffusivity  $\kappa$  as Taylor series in heterogeneity parameter  $a$ .

89 if sub(a=0,kappa) neq 1
90 then rederr("kappa for a=0 must be scaled to one");
91 kappa:=taylor(kappa,a,0,orda);
92 kappa:=trigsimp( taylorstandard(kappa) ,combine)$

Start the iteration from the base multi-modal approximation for the field
and its evolution, given the eigenmodes  $v_m(\theta)$  are  $1, \sin \theta, \cos \theta, \sin 2\theta, \dots$ .
Store the corresponding eigenvalues  $\lambda_m$  of the modes in array lams.

104 u:=(for k:=0:mm-1 sum uu(k)
105     *(if evenp(k) then cos(k/2*q) else sin((k+1)/2*q)));
106 array lams(mm);
107 for k:=0:mm-1 do lams(k) :=
108     -(if evenp(k) then k/2 else (k+1)/2 )^2;
109 for k:=0:mm-1 do write dudt(k) := lams(k)*uu(k);

Iteratively seek solution to the specified orders of errors.

113 for it:=1:maxit do begin write "
114 **** ITERATION ",it;

Progressively truncate the order of the order parameter so that we control
the residuals better: the bounds in these if-statement are the aimed for
ultimate order of errors.

121 if it<ordd then let d^(it+1)=>0;
122 if it<orda then let a^(it+1)=>0;

Compute the PDE residual via the flux, optionally including heterogeneous
nonlinear advection.

128 flux:=-kappa*(d*df(u,x)+df(u,q));
129 if gamma neq 0 then flux:=flux+gamma*eta*u^2/2;
130 pde:=df(u,t)+d*df(flux,x)+df(flux,q);
131 pde:=trigsimp(pde,combine);

Trace print either the residual expression or its length.

```

```

135   if length(pde)<20 then write pde:=pde
136   else write lengthpde:=length(pde);

```

Update the evolution via the solvability conditions over θ , simultaneously removing the ‘resonant’ terms from the right-hand side of the homological equation (5.11).

```

144   rhs:=pde+( gd:=(pde where {sin(~a)=>0,cos(~a)=>0}) );
145   dudt(0):=dudt(0)+gd;
146   for k:=1:mm-1 do begin
147     vk:=(if evenp(k) then cos(k/2*q) else sin((k+1)/2*q));
148     dudt(k):=dudt(k)+( gd:=-coeffn(rhs,vk,1) );
149     rhs:=rhs+gd*vk;
150   end;

```

For solving for corrections to the invariant manifold field from the residual we first need an operator `homolog` to account for all factors of amplitude U_k in the homological equation (5.11). Define these once only in the first iteration.

```

158   if it=1 then begin
159     operator homolog; linear homolog;
160     depend q,qu; depend uu,qu;
161     let { homolog(~~a*uu(~m)^^~p,qu,~l)
162           => uu(m)^p*homolog(a,qu,l+p*lams(m))
163           , homolog(~~a*df(uu(~m),x)^^~p,qu,~l)
164           => df(uu(m),x)^p*homolog(a,qu,l+p*lams(m))
165           , homolog(~~a*df(uu(~m),x,~n)^^~p,qu,~l)
166           => df(uu(m),x,n)^p*homolog(a,qu,l+p*lams(m))
167     };

```

Also setup these `intq` transformations to solve the components of the homological equation (5.11).

```

172     intq:={ homolog(sin(~~n*q),qu,~lam)=>sin(n*q)/(lam+n^2)
173             , homolog(cos(~~n*q),qu,~lam)=>cos(n*q)/(lam+n^2)
174           };
175   end;%if it

```

With the above solvable right-hand side, now update the multi-continuum, multi-modal, invariant manifold field.

```

180   rhs:=homolog(rhs,qu,0);
181   u:=u-(rhs where intq);

```

Finish the loop when the residual of the PDE is zero to the specified order of error,

```

187   if pde=0 then write "Success: ",it:=it+100000;
188   end;%for it

```

```

189 showtime;
190 if pde neq 0 then rederr("Iteration Failed to Converge");

```

A.2 Post-process

Post-process writes out the multi-continuum, multi-modal, evolution, and the corresponding invariant manifold, to one order lower, if not too long.

```

202 uLow:=(u*a*d)/a/d$
203 if length(uLow)<20 then write uLow:=uLow;
204 for i:=0:mm-1 do write "dU",i,"/dt = ",dudt(i);

```

Optional high-order in heterogeneity Optionally output selected coefficients for power series analysis.

```

211 if orda>10 then begin
212     c0:=coeffn(dudt(0),df(uu(0),x,2),1)/d^2$
213     c1:=coeffn(dudt(1),uu(1),1)$
214     c2:=coeffn(dudt(2),uu(2),1)$
215     on rounded;
216     out "cas1dCs.m";
217     write "
218     cs0 = ",coeff(c0,a),"
219     cs1 = ",coeff(c1,a),"
220     cs2 = ",coeff(c2,a),"
221     for i=1:3, figure(i)
222     figname=['Figs/' mfilename num2str(i)]
223     clf, set(gca,'position',[.2 .2 .54 .54])
224     switch i
225     case 1, radiusConverge(cs0)
226     case 2, radiusConverge(cs1)
227     case 3, radiusConverge(cs2)
228     end
229     exportgraphics(gcf,[figname '.pdf'] , 'ContentType','vector')
230     matlab2tikz([figname '.tex']...
231     , 'showInfo',false, 'showWarnings',false, 'parseStrings',false ...
232     , 'extraCode', ['\tikzsetnextfilename{' figname '}'] ...
233     , 'extraAxisOptions','max space between ticks={50}' )
234     end%for
235     "$
236     shut "cas1dCs.m";
237     off rounded;
238 end;%if orda

```

Optional high-order spatial structure Optionally apply discovered operator that simplifies evolution of most a^2, a^3 terms. Define $\text{dinv} := (1 + 4/9\partial_x^2)^{-1}$.

```

246 if ordd>10 and orda=4 then begin
247     write "Multiply a^2,a^3 by operator D = 1+4/9*df(,x,x)";
248     procedure dop(f); f+4/9*d^2*df(f,x,2);
249     operator dinv; linear dinv;
250     for i:=0:mm-1 do write "dU",i,"/dt = ", coeffn(dudt(i),a,0)
251         +a*coeffn(dudt(i),a,1)
252         +a^2*dinv(dop(coeffn(dudt(i),a,2)),x)
253         +a^3*dinv(dop(coeffn(dudt(i),a,3)),x);
254 end;%if orda

```

Computer algebra fin.

```

259 end;

```

B Computer algebra construction of high contrast example

This Reduce-algebra code constructs any chosen multi-continuum, micromorphic, invariant manifold homogenisation of the high-contrast example of (2.1) discussed by Section 4. Write approximations, such as (4.6) and (4.9), to the slow manifold homogenisation of the embedding PDE (2.4) in terms of ‘modal’ macro-scale fields $U_i(t, x)$, denoted by $\text{uu}(i)$, that evolves according to $\partial^\alpha U_i / \partial t^\alpha = \text{dudt}(i)$ for whatever $\text{dudt}(i)$ happens to be constructed, and for either $\alpha = 1$ for diffusive case or $\alpha = 2$ for wave case.

In principle, for linear systems and whenever the time evolution operator ∂_t^α commutes with spatial derivatives, then the construction is also valid and gives the dynamic homogenisation $\partial_t^\alpha U_i = \text{dudt}(i)$.

Set the desired derivative parameter α , the required dimensionality M of the invariant manifold multi-modal multi-continuum model, and the order of error in spatial gradients, $\text{orrd} = N + 1$. Optionally include nonlinear advection $-\gamma uu_x$, Section 4.5, by setting appropriate truncation in gamma .

```

36 alpha:=1;
37 mm:=2;
38 orrd:=5;
39 let gamma=>0;

```

The series approximations are only computed approximately, so set a desired relative error for the numerical coefficients. And use `zeroSmall` to eliminate negligible terms.


```
46 relTolerance:=1e-8;
```

The macroscale amplitudes, order parameters, depend upon time (depending upon α) and space.

```
52 array dudt(mm-1);
53 operator uu; depend uu,x,t;
54 if alpha=1
55 then let { df(uu(~i),t)=>dudt(i)
56           , df(uu(~i),t,x)=>df(dudt(i),x)
57           , df(uu(~i),t,x,~n)=>df(dudt(i),x,n)
58           }
59 else let { df(uu(~i),t,2)=>dudt(i)
60           , df(uu(~i),t,2,x)=>df(dudt(i),x)
61           , df(uu(~i),t,2,x,~n)=>df(dudt(i),x,n)
62           };
```

Improve printed output, and use numerical, floating-point, coefficients.

```
68 on div; off allfac; on revpri;
69 on rounded; print_precision 4$
70 factor d,df,uu;
71 in "zeroSmall.txt"$
72 tolerance:=relTolerance$
```

B.1 Parametrise a non-dimensional case

For simplicity, non-dimensionalise space and time so that $\kappa_1 = 1$ and micro-scale periodicity is $\ell = 2\pi$. Choose a layer that is say 6% of the microscale so there are a reasonable nine sub-microscale points across the layer.

```
83 ell:=2*pi;
84 eta:=0.06*ell; % width of thin layer
85 chi:=1; % strength of insulation
86 kappa0:=eta/chi/ell; % relative to kappa1=1
```

Choose to discretise the θ -structure across a cell in terms of values at n equi-spaced points, use q to denote θ . Set the microscale grid on the interval $[-\ell/2, +\ell/2] = [-\pi, \pi]$, and periodic:

```
93 n:=128;
94 procedure q(j); ((j-1/2)/n-1/2)*ell;
95 dq:=q(2)-q(1);
```

Define a procedure to write out the parameters as a comment: used to label various output files.

```

100 procedure writeTheCase; write "%"
101     , " alpha=", alpha , " , Nmodes=", mm , " , n=", n
102     , " , ell=", ell , " , eta/ell=", eta/ell , " , chi=", chi;

```

Set some elementary matrices, and then define the discrete operator of heterogeneous interaction across a cell.

```

107 matrix zeros(n,1), ones(n,1), Id(n,n), ee(n,n);
108 for j:=1:n do ones(j,1):=1; % vector of ones
109 for j:=1:n do Id(j,j):=1; % identity matrix

```

Matrix to shift vector up, circularly: $Eu_j := u_{j+1}$; and $E^T = E^{-1}$ is shift vector down, $E^T u_j := u_{j-1}$.

```

115 for j:=1:n do ee(j,if j<n then j+1 else 1):=1;

```

Set the cell coefficient matrix, and compute its norm (max column sum of abs). The matrix

$$\mathcal{K} := \begin{bmatrix} -\kappa_{1/2} - \kappa_{3/2} & \kappa_{3/2} & \cdots & \kappa_{1/2} \\ \kappa_{3/2} & -\kappa_{3/2} - \kappa_{5/2} & \cdots & 0 \\ 0 & \ddots & \ddots & \vdots \\ \kappa_{1/2} & \cdots & \kappa_{n-1/2} & -\kappa_{n-1/2} - \kappa_{1/2} \end{bmatrix}$$

where $\kappa_{j-1/2}$ is the diffusivity/elasticity at $\theta_{j-1/2} = \theta_j - d\theta/2$. So diagonal of matrix `emkapep` is the coefficients ‘shifted’ down a half, that is $E^{-1/2} \kappa E^{1/2}$. Set the heterogeneous matrix accordingly, $\mathcal{K} := \delta \kappa \delta / d\theta^2$.

```

134 matrix kk(n,n), emkapep(n,n);
135 for j:=1:n do emkapep(j,j) :=
136     (if abs(cos(q(j-1/2)/2)*2)<eta/2 then kappa0 else 1);
137 kk := (ee-Id)*emkapep*(Id-tp ee)/dq^2$
138 normkk := max(for i:=1:n collect (for j:=1:n sum abs(kk(i,j))));

```

B.2 Spectrum of cell problem

Find the gravest eigenvalues and eigenvectors. The first is the constant eigenvector corresponding to zero eigenvalue. All eigenvectors are found as unit vectors, and then normalised to have unit mean-square in the integral norm.

```

149 write "Finding leading eigenvalues and eigenvectors";
150 array evecs(mm), evals(mm);
151 evecs(0):=ones$
152 evals(0):=0;

```

The k th eigenvector and eigenvalue are found by numerical iteration, starting from approximations that assume a thin low-diffusive layer is around $\theta = \pm\ell/2 = \pm\pi$.

```

159 matrix evec(n,1);
160 for k:=1:mm do begin
    Initialise rough approximate eigenvectors.
164     for j:=1:n do evec(j,1):=
165         (if evenp(k) then cos(k/2*q(j)) else sin(k/2*q(j)));
    This iteration should quadratically converge to an eigenvalue-eigenvector
    pair, and should not miss any grave modes.
171     for it:=1:9 do begin
172         if it>1 then evec:=1/(kk-eval*Id)*evec; % update eigenvector
173         evec:=evec/sqrt(part(tp evec*evec,1,0)); % normalise eigenvector
174         eval:=(tp evec)*kk*evec; % update eigenvalue
175         res:=(kk-eval*Id)*evec; % check residual
176         write normres:=for j:=1:n sum abs(res(j,1));
177         if normres<1e-8*normkk
178             then write "success: ",it:=it+1000;
179         end;%for it
180         if normres>1e-8*normkk then rederr("failed eigenvalue iteration");
181         evecs(k):=evec*sqrt(2*pi/dq); % normalise so mean-square is one
182         write evals(k):=eval(1,1);
183         for l:=k step -1 until 1 do % sort ensures eigenvalues decrease
184             if evals(l)>evals(l-1) then begin
185                 tmp:=evals(l); evals(l):=evals(l-1); evals(l-1):=tmp;
186                 tmp:=evecs(l); evecs(l):=evecs(l-1); evecs(l-1):=tmp;
187             end;%if
188     end;%for k

```

Optionally plot the eigenvectors. Also check that the pattern of signs in the eigenvectors is as expected.

```

194 array xv(mm);
195 for k:=0:mm do xv(k):=
196     for j:=1:n collect {q(j),part(evecs(k),j,0)};
197 %if mm=1 then plot(xv(0),xv(1));
198 %if mm=2 then plot(xv(0),xv(1),xv(2));
199 %if mm=3 then plot(xv(0),xv(1),xv(2),xv(3));
200 for k:=1:mm do begin
201     v:=evecs(k);
202     write signs := for j:=3:n-1 sum
203         abs(sign(v(j,1))-sign(v(j-1,1)))/2;

```

```

204     if signs neq k then rederr("wrong pattern of signs");
205 end;%for k

```

Output pgfplots commands to subsequently draw the eigenvectors in L^AT_EX via pgfplots.

```

210 out "hcegEvecs.tex";
211 writeTheCase();
212 write"\begin{tikzpicture}
213 \makeatletter\let\gob\@gobble\makeatother
214 \begin{axis}[no marks,
215     xlabel={microscale  $\theta$ },ylabel={eigenvector},
216     legend pos=south east,legend style={font=\tiny}];
217 for k:=0:mm do begin
218     write "\addplot+[",if k=mm then "dashed" else ""
219         ,"] plot coordinates {";
220     foreach qu in xv(k) do write
221         " (" ,part(qu,1)," ,",part(qu,2),")\gob"$
222     write ";";
223     \addlegendentry{" ,evals(k), "$}$"
224 end;%for k
225 write "\end{axis}
226 \end{tikzpicture}";
227 shut "hcegEvecs.tex";

```

B.3 Form inverse for homological updates

Corrections to the approximate invariant manifold shape and evolution are done by simplified the homological equation (5.12), a physics-informed linear system (e.g., Roberts 2015b, §5.3). The following inverse would be ‘wrong’ for multi-mode updates involving non-zero eigenvalues in the manifold, but as part of an adiabatic iteration it is good enough upon more iterations.

```

241 matrix llinv(n+mm,n+mm),rhs0(n+mm,1);
242 for i:=1:n do for j:=1:n do llinv(i,j):=kk(i,j);
243 for i:=1:mm do begin
244     v:=evecs(i-1);
245     for j:=1:n do llinv(n+i,j):=-v(j,1);
246     for j:=1:n do llinv(j,n+i):=-v(j,1);
247 end;
248 llinv:=1/llinv$
249 write "Formed Linv OK";
250 off roundbf; write "--- RoundBF turned off";

```

B.4 Iteration systematically constructs multi-modal model

Second, we iteratively construct the improved homogenizations (4.4), (4.5), (4.6) and (4.9).

```

263 write "
264 Iteratively Construct
265 -----";
266 maxit:=99;

Start the iteration from the trivial approximation for the field and its evolu-
tion.

273 u:=for n:=0:mm-1 sum uu(n)*evecs(n)$
274 for n:=0:mm-1 do write dudt(n):=evals(n)*uu(n);

Seek solution to the specified orders of errors (via the instant evaluation
property of the for loop index).

279 for it:=orodd:orodd do let d^it=>0;
280 for it:=1:maxit do begin

Compute the PDE residual via the flux, trace printing the length of the
residual expression. The embedding PDE (2.4) is discretised across the cell,
but retaining algebraic  $x, t$ -dependence, in terms of mean  $\mu$  and difference  $\delta$ 
operators, as


$$\text{flux } F := -\kappa \left( \mu \frac{\partial u}{\partial x} + \frac{\delta u}{d\theta} \right), \quad \text{residual} := \frac{\partial u}{\partial t} + \mu \frac{\partial F}{\partial x} + \frac{\delta F}{d\theta},$$


for micro-grid spacing  $d\theta := 2\pi/n$ . Here compute  $E^{-1/2}F$ , and write out
the overall size of the coefficients on the residual.

298 emflux:=-emkapep*((Id+tp ee)/2*d*df(u,x)+(Id-tp ee)*u/dq);
299 pde:=df(u,t,alpha)+(Id+ee)/2*d*df(emflux,x)+(ee-Id)*emflux/dq;

Optionally add in example nonlinearity (when not gamma=>0).

304 for j:=1:n do pde(j,1):=pde(j,1)+gamma*u(j,1)*(d*df(u(j,1),x)
305 + (u(mod(j,n)+1,1)-u(mod(j-2,n)+1,1))/(2*dq) );

Compute a norm of the residual, assuming the magnitude of coefficients in
derivative  $\partial_x^m$  typically grows like  $R^m$  for factor  $R \approx 2$  or 3, so the norm is
weighted accordingly. Make the convergence test relative to the maximum
norm found to date during the iteration.

314 rr := part({2,3,2,2,2},mm);% extend set for more modes
315 maxnorm := (if it=1 then 1 else max(maxnorm,normpde));
316 tmp := (pde where { df(uu(~n),x,~m)=>uu(n)/rr^m
317 , df(uu(~n),x)=>uu(n), gamma=>1 } );

```

```

318     tmp := (tmp where uu(~n)=>uu^n);
319     write "Iteration ",it,", ",
320     normpde:=max(abs( for j:=1:n join (
321         foreach l in coeff(tmp(j,1),uu) join
322             coeff(l,d) ) ));

```

Update the manifold and evolution quasi-adiabatically, zeroing coefficients smaller than tolerance.

```

328     for j:=1:n do rhs0(j,1):=pde(j,1);
329     for j:=1:mm do rhs0(n+j,1):=0;
330     ugd:=llinv*rhs0;
331     for j:=1:n do u(j,1):=u(j,1)+ugd(j,1);
332     u:=zeroSmall(u);
333     for j:=1:mm do
334         dudt(j-1):=zeroSmall(dudt(j-1)+ugd(n+j,1));

```

Finish the loop when the residuals of the PDE are zero to the specified error tolerance,

```

340     if normpde<relTolerance*maxnorm %pde=zeros
341     then write "Success: ",it:=it+100000;
342 end;%for it
343 showtime;
344 if normpde>relTolerance*maxnorm %pde neq zeros
345 then rederr("Iteration Failed to Converge");

```

B.5 Post-process

Post-process writes out the multi-continuum, multi-modal, evolution,

```

356 for i:=0:mm-1 do write "U",i
357     ,if alpha=1 then "_t = " else "_tt= " ,dudt(i);

```

Also write out the instructions to draw \LaTeX graphs of the spatial structure of the invariant manifold, up to coefficients of the second order.

```

363 nd:=2$
364 array xs(nd); xs(0):=""$ xs(1):="x"$ xs(2):="xx"$
365 operator slct1; linear slct1;
366 let { slct1(1,~a)=>0
367     , slct1(~b,~a)=>1 when b neq 1
368     };
369 out "hcegManifold.tex";
370 writeTheCase();
371 write"\begin{tabular}{@{}c@{}c@{}}";
372 for k:=0:mm-1 do begin

```

```

373     uk:=map(slct1(~a,uu(k)),u);
374     write if evenp(k+mm-1) then "& "
375     else if k>0 then "\\ " else ""
376     ,"\begin{tikzpicture}
377     \makeatletter\let\gob\@gobble\makeatother
378     \begin{axis}[no marks,small
379         ,xlabel={microscale $\theta$}
380         ,ylabel={component in $u(\theta)$}
381         ,legend pos=south west
382         ,legend style={font=\footnotesize}]";
383     for l:=0:nd do begin
384         ukl:=map(coeffn(~a,d,l),uk);
385         write "\addplot+[] plot coordinates {";
386         for j:=1:n do write
387             "      (,q(j),",",ukl(j,1),")\gob"$
388         write ";";
389         \addlegendentry{$U_{",k,xs(l),"}$}$
390     end;%for l
391     write "\end{axis}
392     \end{tikzpicture}";
393 end;%for k
394 write"\end{tabular}";
395 shut "hcegManifold.tex";

Finish of script.

400 end;% script

```

C Computer algebra constructs 2-D elastic homogenisation

This Reduce-algebra code constructs any chosen multi-continuum, micromorphic, invariant manifold homogenisation of the 2-D heterogeneous elasticity example of (6.1) and (6.2) discussed by Section 6. Specify the number of macroscale multi-continuum modes M , and the microscale cell size $n_x \times n_y$.

```

17 mm:=3;
18 nx:=ny:=10;

```

Parameter `ordd` sets the order of the error residual, and `maxit` the maximum number of iterations.

```

23 ordd:=3;
24 maxit:=99;

```

Turn on rounded to get numerical coefficients, and only report two significant digits.

```
29 on rounded; print_precision 2$
```

Coefficients smaller than the following tolerance are set to zero. This enables the simple-minded iteration to terminate, but gives a small numerical error in coefficients.

```
36 tolerance:=1e-7;
```

Improve printed output:

```
42 on div; off allfac; on revpri;
```

```
43 factor d;
```

Load function zeroSmall that zeros all numbers smaller than the set tolerance. Only works with roundbf off.

```
49 in "zeroSmall.txt"$
```

Let the heterogeneity be 1-periodic in both x, y , and the same periodicity of say 20 in the sub-cell lattice. These lattices are half-spaced in x, y and so double size—provides for staggered micro-grid.

```
58 dx:=1/nx; dy:=1/ny;
```

```
59 matrix xx(2*nx,2*ny),yy(2*nx,2*ny),ones(2*nx,2*ny);
```

```
60 for i:=1:2*nx do for j:=1:2*ny do xx(i,j):=(i-0.5)*dx/2;
```

```
61 for i:=1:2*nx do for j:=1:2*ny do yy(i,j):=(j-0.5)*dy/2;
```

```
62 for i:=1:2*nx do for j:=1:2*ny do ones(i,j):=1;
```

```
63 zeros:=0*ones$
```

Define sets of staggered grid indices: horizontal u is in evens \times evens, whereas vertical v is in odd \times odds.

```
69 odds:= for i:=1 step 2 until 2*nx collect i;
```

```
70 evns:= for i:=2 step 2 until 2*nx collect i;
```

Define heterogeneity Define the heterogeneity in terms of Young's modulus and Poisson parameter. Recall $2 \sin A \sin B = \cos(A - B) - \cos(A + B)$. The following sub-cell heterogeneity, for $n_x = 10$, leads to a eigenvalue gap ratio 1.8 which is enough for linear problems.

```
80 ee := 1/(2*pi)*(map(cos,(xx-yy)*pi)-map(cos,(xx+yy)*pi))$
```

```
81 write ee := ee+0.01/pi*ones;
```

```
82 write nu:=0.4*ones+0*xx+0*yy;
```

```
83 harmonicMeanE:=(4*nx*ny)
```

```
84 /(for i:=1:2*nx sum for j:=1:2*ny sum 1/ee(i,j));
```


Compute corresponding Lamé parameters.

```

88 matrix lla(2*nx,2*ny),lmu(2*nx,2*ny);
89 for i:=1:2*nx do for j:=1:2*ny do begin
90     lla(i,j):=nu(i,j)*ee(i,j)/(1+nu(i,j))/(1-2*nu(i,j));
91     lmu(i,j):=ee(i,j)/2/(1+nu(i,j)); end;

```

Account for the cell-periodicity of indices, assumes $n_x = n_y$

```

96 procedure c(i); mod(i-1,2*nx)+1;

```

C.1 Compute the cell operator

Then the cell operator returns matrix of residuals of PDEs on the (odd,odd) and (even,even) lattice points of the matrix, zero otherwise. Take 1s for $n_x=6$ and 4s for $n_x=8$.

```

106 matrixproc rescell(uv); begin
107     scalar pde; pde:=0*uv; % local variable
108     % stress xy in (even,odd) points
109     foreach i in evns do for each j in odds do
110         uv(i,j):=lmu(i,j)*( (uv(c(i+1),j)-uv(c(i-1),j))/dx
111                             +(uv(i,c(j+1))-uv(i,c(j-1)))/dy );
112     % stress xx in (odd,even) points
113     foreach i in odds do for each j in evns do
114         uv(i,j):=(lla(i,j)+2*lmu(i,j))*(uv(c(i+1),j)-uv(c(i-1),j))/dx
115                             +lla(i,j)*(uv(i,c(j+1))-uv(i,c(j-1)))/dy);
116     % horizontal u in (even,even) points
117     foreach i in evns do for each j in evns do
118         pde(i,j):= (uv(c(i+1),j)-uv(c(i-1),j))/dx
119                 +(uv(i,c(j+1))-uv(i,c(j-1)))/dy ;
120     % stress yy in (odd,even) points, overwrites xx
121     foreach i in odds do for each j in evns do
122         uv(i,j):=          lla(i,j)*(uv(c(i+1),j)-uv(c(i-1),j))/dx
123                 +(lla(i,j)+2*lmu(i,j))*(uv(i,c(j+1))-uv(i,c(j-1)))/dy);
124     % vertical v in (odd,odd) points
125     foreach i in odds do for each j in odds do
126         pde(i,j):= (uv(c(i+1),j)-uv(c(i-1),j))/dx
127                 +(uv(i,c(j+1))-uv(i,c(j-1)))/dy ;
128     return pde;
129 end;%matrixproc rescell

```

C.2 Finds eigenmodes via cell Jacobian and SVD

The displacements u, v fit into half of a $2n_x \times 2n_y$ matrix, so the vector of displacements would be of length $2n_x n_y$, and the Jacobian is $2n_x n_y$ -square. For $n_x = n_y = 6$ takes 2.4s to compute the SVD for $n_x=6$, 20 s for $n_x=8$.

```

140 write "Forming Jacobian";
141 matrix jac(2*nx*ny,2*nx*ny);
142 l:=0$
143 foreach li in odds do foreach lj in odds do
144   for lo:=0:1 do begin
145     l:=l+1; %compute lth column of Jacobian
146     uv:=zeros; uv(li+lo,lj+lo):=1;
147     lop:=rescell(uv);
148     k:=0; % store in (k,l) elements
149     foreach ki in odds do foreach kj in odds do
150       for ko:=0:1 do jac(k:=k+1,l):=lop(ki+ko,kj+ko);
151   end;%for li,lj,lo
152   jacSym:=max(abs( jac-tp jac ));
153   if zeroSmall(jacSym)neq 0 then
154     rederr("Jacobian is not symmetric");
155   showtime;

```

Use the SVD to get eigenvalues and eigenvectors of the symmetric Jacobian.

```

161 load_package linalg;
162 Write "Computing SVD of Jacobian (aka eigenvalues)";
163 usv:=svd(jac)$
164 uvc:=part(usv,1)$
165 ss:=part(usv,2)$
166 showtime;

```

Normalise all eigenvectors to have max-abs value equal one.

```

170 for l:=1:2*nx*ny do begin
171   tmp := max abs(for k:=1:2*nx*ny collect uvc(k,l));
172   for k:=1:2*nx*ny do uvc(k,l):=uvc(k,l)/tmp;
173 end;%for l

```

Find the smallest $M + 1$ singular values (assuming the first is not one of the smallest): here, eigenvalues are the negative of these.

```

180 array ls(mm+1);
181 for m:=1:mm+1 do ls(m):=1;
182 procedure ssmm(l,m);
183   if ss(l,1)<ss(ls(m),ls(m)) then <<
184     for q:=mm+1 step -1 until m+1 do ls(q):=ls(q-1);

```

```

185         ls(m):=1; >>
186         else if m<mm+1 then ssmin(1,m+1);
187     for l:=2:2*nx*ny do ssmin(1,1);
188     lss := for m:=1:mm+1 collect ls(m); % trace print
189     smallest := for m:=1:mm+1 collect ss(ls(m),ls(m)); % trace print

```

Override the two zero singular values and their vectors as we know these are equivalent to neutral horizontal and vertical displacements.

```

195     l1:=ls(1)$ l2:=ls(2)$
196     ss(l1,l1):=ss(l2,l2):=0$
197     for l:=1:nx*ny do begin
198         uvc(2*l,l1):=1; uvc(2*l-1,l1):=0;
199         uvc(2*l,l2):=0; uvc(2*l-1,l2):=1;
200     end;%for l

```

Form gravest M eigenvectors and eigenvalues into arrays of spatial matrices.

```

205     clear evc;
206     array evl(mm),evc(mm);
207     for m:=1:mm do begin
208         write evl(m-1):=-ss(ls(m),ls(m));
209         ev:=zeros;
210         k:=0; % store in (k,l) elements
211         foreach ki in odds do foreach kj in odds do
212             for ko:=0:1 do ev(ki+ko,kj+ko):=uvc(k:=k+1,ls(m));
213         evc(m-1):=ev;
214     end;%for m

```

Write approximations to the slow manifold model of the embedding PDE (5.4) in terms of ‘modal’ fields $U_i(t, x, y)$, denoted by $uu(i)$, that evolves according to $\partial^2 U_i / \partial t^2 = dudtt(i)$ for whatever $dudtt(i)$ happens to be.

```

224     array dudtt(mm);
225     operator uu; depend uu,x,y,t;
226     let { df(uu(~i),t,2)=>dudtt(i)
227         , df(uu(~i),t,2,x)=>df(dudtt(i),x)
228         , df(uu(~i),t,2,y)=>df(dudtt(i),y)
229         , df(uu(~i),t,2,x,~p)=>df(dudtt(i),x,p)
230         , df(uu(~i),t,2,y,~p)=>df(dudtt(i),y,p)
231     };

```

C.3 Iteration systematically constructs multi-modal model

Let's iteratively construct the standard, higher-order, and/or multi-continuum homogenizations (6.7), (6.8) and (6.9). For $M = 3$ modes and $n_x = 6$ takes about 1 s per iteration.

```
245 write "
246 Iteratively Construct
247 -----";
```

Define spatial shift operators of (6.4) in terms of derivatives in x, y . From the operator identity that $E = \exp(h\partial_x)$ (e.g., [Natl Physical Lab 1961](#), p.65), and using `d` to count the number of derivatives. Let E_x, E_y denote forward half-shifts, and F_x, F_y denote backward half-shifts.

```
257 operator ex,fx,ey,fy;
258 let { ex(~f)=>f+for n:=1:orodd-1 sum d^n*df(f,x,n)*(+dx/2)^n/factorial(n)
259       , fx(~f)=>f+for n:=1:orodd-1 sum d^n*df(f,x,n)*(-dx/2)^n/factorial(n)
260       , ey(~f)=>f+for n:=1:orodd-1 sum d^n*df(f,y,n)*(+dy/2)^n/factorial(n)
261       , fy(~f)=>f+for n:=1:orodd-1 sum d^n*df(f,y,n)*(-dy/2)^n/factorial(n)
262     };
```

Form the extended matrix to use to solve for updates.

```
267 write "Finding LU-decomposition for updates";
268 matrix zerom(mm,mm);
269 tmp := get_columns(uvc,for m:=1:mm collect ls(m))$
270 zz := matrix_augment(foreach z in tmp collect z)$ %weird work-around
271 jaczz := matrix_augment( jac,zz )$
272 zz := matrix_augment( (tp zz),zerom )$
273 jaczz:=matrix_stack(jaczz,zz)$
```

Perform LU decomposition

```
277 in_tex "lu_decomp.tex"$
278 in_tex "lu_backsub.tex"$
279 lu:=lu_decomp(jaczz)$
280 showtime;
```

If it got turned on, need to turn off `roundbf` in order for `zeroSmall` to work its magic.

```
285 off roundbf;
```

Start the iteration from the base invariant subspace approximation for the field and its evolution.

```
292 uv:=for m:=0:mm-1 sum evc(m)*uu(m)$
293 for m:=0:mm-1 do dudtt(m):=evl(m)*uu(m);
```

Seek solution to the specified orders of errors.

```

297 for it:=ordd:ordd do let d^it=>0;
298 for it:=1:maxit do begin write "
299 **** ITERATION ",it;

Zero the stress entries in uv before computing time derivatives:

305 foreach i in evns do foreach j in odds do uv(i,j):=0;
306 foreach i in odds do foreach j in evns do uv(i,j):=0;

Compute the residual of the embedding equations (6.5), via the stresses:

311 pde:=-df(uv,t,t);
312 % stress xy in (even,odd) points
313 foreach i in evns do for each j in odds do
314   uv(i,j):=lmu(i,j)*( (ex uv(c(i+1),j) -fx uv(c(i-1),j))/dx
315                       +(ey uv(i,c(j+1)) -fy uv(i,c(j-1)))/dy );
316 % stress xx in (odd,even) points
317 foreach i in odds do for each j in evns do
318   uv(i,j):=(lla(i,j)+2*lmu(i,j))*(ex uv(c(i+1),j) -fx uv(c(i-1),j))/dx
319           +lla(i,j)*(ey uv(i,c(j+1)) -fy uv(i,c(j-1)))/dy);
320 % horizontal u in (even,even) points
321 foreach i in evns do for each j in evns do
322   pde(i,j):=pde(i,j)
323     +(ex uv(c(i+1),j) -fx uv(c(i-1),j))/dx
324     +(ey uv(i,c(j+1)) -fy uv(i,c(j-1)))/dy ;
325 pde:=pde;
326 % stress yy in (odd,even) points, overwrites xx
327 foreach i in odds do for each j in evns do
328   uv(i,j):=
329     lla(i,j)*(ex uv(c(i+1),j) -fx uv(c(i-1),j))/dx
330     +(lla(i,j)+2*lmu(i,j))*(ey uv(i,c(j+1)) -fy uv(i,c(j-1)))/dy);
331 % vertical v in (odd,odd) points
332 foreach i in odds do for each j in odds do
333   pde(i,j):= pde(i,j)
334     +(ex uv(c(i+1),j) -fx uv(c(i-1),j))/dx
335     +(ey uv(i,c(j+1)) -fy uv(i,c(j-1)))/dy ;

Trace print the length of the residual.

338 pde:=zeroSmall(pde);
339 if length(pde(1,1))<10 then write pde11:=pde(1,1);
340 write maxlengthpde:=max( map(length,pde) );

On the first iteration check the invariant subspace.

344 if it=1 then if sub(d=0,pde) neq zeros then
345   rederr("Invariant subspace not satisfied");

```

To compute update, form residual into column vector, then apply pre-computed LU factorisation.

```

351 matrix res(2*nx*ny+mm,1);%sets to zero
352 k:=0;
353 foreach ki in odds do foreach kj in odds do
354     for ko:=0:1 do res(k:=k+1,1):=pde(ki+ko,kj+ko);
355 upd:=lu_backsub(lu,res);

    Unpack update into corrections

359 k:=0;
360 foreach ki in odds do foreach kj in odds do
361     for ko:=0:1 do uv(ki+ko,kj+ko):=uv(ki+ko,kj+ko)-upd(k:=k+1,1);
362 for m:=0:mm-1 do dudtt(m):=dudtt(m)+upd(k:=k+1,1);

    Finish the loop when the residuals of the PDE are zero to the specified error,

369     showtime;
370     if pde=zeros then write "Success: ",it:=it+100000;
371 end;%for it
372 if pde neq zeros then rederr("Iteration Failed to Converge");

```

C.4 Post-process

Check amplitudes of at least the mean displacement modes (more robust would be to check these inside the loop, and update accordingly).

```

383 print_precision 3$
384 meanu:= zeroSmall( (foreach i in evns sum
385                     foreach j in evns sum uv(i,j))/nx/ny );
386 meanv:= zeroSmall( (foreach i in odds sum
387                     foreach j in odds sum uv(i,j))/nx/ny );
388 if meanu neq uu(0) then rederr("U0 amplitude not preserved");
389 if meanv neq uu(1) then rederr("U1 amplitude not preserved");

```

Report effective material constants of the second-order derivative terms when have chosen two-mode bi-continuum.

```

395 if mm=2 then begin
396     write mu_h:=coeffn(dudtt(0),df(uu(0),y,2),1);
397     write lambda_2:=coeffn(dudtt(0),df(uu(1),x,y),1)-mu_h;
398     write lambda_1:=coeffn(dudtt(0),df(uu(0),x,2),1)-2*mu_h;
399     write errors:={ mu_h-coeffn(dudtt(1),df(uu(1),x,2),1)
400                    , lambda_2-coeffn(dudtt(1),df(uu(0),x,y),1)+mu_h
401                    , lambda_1-coeffn(dudtt(1),df(uu(1),y,2),1)+2*mu_h};
402 end;%if mm

```

Neglect any small coefficients (e.g., less than 0.001), and print out the evolution PDEs, to up to two decimal places.

```

409 tolerance:=0.001;
410 for m:=0:mm-1 do write dudtt(m):=zeroSmall( dudtt(m) );
411 uv:=map(zeroSmall,uv)$

Print out the terms grouped by order.

416 array ord(ordd);
417 for p:=0:ordd-1 do write
418     ord(p):=for m:=0:mm-1 collect coeffn(dudtt(m),d,p);

Finish of the script.

423 end;
424 rederr("Post script: should not occur");

```

D General solution of modal fractional differential equation

To fillin details for [Section 5.2.4](#), this appendix seeks a general solution $u(t)$ of the fractional differential equation (FDE)

$$\partial_t^\alpha u(t) = \lambda u(t) + q(t), \quad (\text{D.1})$$

for parameter λ that is typically real and negative, and where $q(t)$ is some given forcing. In terms of functions to be defined next, we show a general solution is of the form

$$u(t) := \sum_{k=0}^{\hat{\alpha}} c_k \mu^{-k} e_\alpha^{(-k)}(\mu t) - \mu^{1-\alpha} e_\alpha^{(1)}(\mu t) \star q(t), \quad \text{for } \mu := (-\lambda)^{1/\alpha}. \quad (\text{D.2})$$

The free constants c_k may be identified as the initial values $c_k = u^{(k)}(0^+)$. Useful large time asymptotics, from [\(D.7\)](#) and for negative real λ , are

$$e_\alpha^{(0)}(t) \sim \frac{t^{-\alpha}}{\Gamma(1-\alpha)}, \quad e_\alpha^{(-1)}(t) \sim \frac{t^{1-\alpha}}{\Gamma(2-\alpha)}, \quad e_\alpha^{(1)}(t) \sim \frac{t^{-1-\alpha}}{\Gamma(-\alpha)}. \quad (\text{D.3})$$

[Figure 10](#) plots the solution component $e_\alpha^{(0)}(t)$ for various $0 < \alpha < 1$ with their large-time approximations. Further, for various $1 < \alpha < 2$, [Figure 11](#) plots the two solution components $e_\alpha^{(0)}(t)$ and $e_\alpha^{(-1)}(t)$.

The following adapts and generalises some of the report by [Gorenflo & Mainardi \(1997\)](#), cited by the acronym GM.

We define ∂_t^α in the Caputo sense (GM, (1.17)). First define the fractional integral operator as the following convolution (GM, (1.2)): for every $\alpha > 0$

$$\mathcal{J}^\alpha f(t) := \frac{1}{\Gamma(\alpha)} t^{\alpha-1} \star f(t) := \frac{1}{\Gamma(\alpha)} \int_0^t (t-\tau)^{\alpha-1} \star f(\tau) d\tau. \quad (\text{D.4})$$

Secondly for non-integer α , and defining the integer $\hat{\alpha} := \lceil \alpha \rceil$, the fractional derivative in FDE (D.1) is

$$\partial_t^\alpha u(t) := \mathcal{J}^{\hat{\alpha}-\alpha} u^{(\hat{\alpha})}(t), \quad (\text{D.5})$$

Then solutions (D.2) of the FDE (D.1) are expressed in terms of the function $e_\alpha^{(0)}(t) := E_{\alpha,1}(-t^\alpha)$ (GM, (3.11)), where in turn we define the Mittag-Leffler function $E_{\alpha,\beta}(z) := \sum_{k=0}^{\infty} \frac{z^k}{\Gamma(\alpha k + \beta)}$ (GM, (A.1)). Special cases are $E_{0,1} = 1/(1-z)$, $E_{1/2,1} = e^{z^2} \operatorname{erfc}(-z)$, $E_{1,1} = e^z$, $E_{2,1} = \cosh \sqrt{z}$. Various relations and derivatives are useful (GM, (A.8)–(A.10)), such as

$$\frac{d}{dz} E_{\alpha,\beta}(z) = \frac{1}{\alpha z} [E_{\alpha,\beta-1}(z) - (\beta-1)E_{\alpha,\beta}(z)]. \quad (\text{D.6})$$

Two asymptotic expansions may be of interest (GM, (A.22)–(A.23); and Haubold et al. (2011), (6.10)–(6.11)): for $0 < \alpha < 2$ and as $|z| \rightarrow \infty$,

$$E_{\alpha,\beta}(z) \sim - \sum_{k=1}^{\infty} \frac{z^{-k}}{\Gamma(\beta - \alpha k)} + \begin{cases} \frac{1}{\alpha} z^{(1-\beta)/\alpha} \exp(z^{1/\alpha}), & |\arg z| < \alpha\pi/2, \\ 0, & |\arg(-z)| < \alpha\pi/2. \end{cases} \quad (\text{D.7})$$

For integer $k > 0$, define $e_\alpha^{(k)}(t)$ to be the k th derivative of $e_\alpha^{(0)}(t)$, and $e_\alpha^{(-k)}(t)$ to be the k th integral from zero of $e_\alpha^{(0)}(t)$, that is, $e_\alpha^{(-k)}(t) := 1 \star e_\alpha^{(-k+1)}(t) = \int_0^t e_\alpha^{(-k+1)}(\tau) d\tau$. For examples of each, and using (D.6): $e_\alpha^{(1)}(t) = \frac{1}{t} E_{\alpha,0}(-t^\alpha)$; and $e_\alpha^{(-1)}(t) = t E_{\alpha,2}(-t^\alpha)$ (e.g., differentiate the right-hand side).

Lemma 12. *The fractional differential equation (D.1) has general solution (D.2).*

Proof. We show that solutions (D.2) satisfy the FDE (D.1). Take Laplace transform, $L\{\cdot\}$, of (D.2), and since $L\{f(at)\} = \frac{1}{a} \tilde{f}(s/a)$,

$$\tilde{u}(s) = \sum_{k=0}^{\hat{\alpha}} c_k \mu^{-k} \frac{1}{\mu} L\{e_\alpha^{(-k)}\}(s/\mu) - \mu^{1-\alpha} \frac{1}{\mu} L\{e_\alpha^{(1)}\}(s/\mu) \tilde{q}(s). \quad (\text{D.8a})$$

Now $\tilde{e}_\alpha^{(0)}(t) = \frac{s^{\alpha-1}}{s^{\alpha+1}}$ (GM, (3.11)). Hence by the integration rule, for integer $k > 0$, $L \left\{ e_\alpha^{(-k)}(t) \right\} = \frac{s^{\alpha-k-1}}{s^{\alpha+1}}$, and by the differentiation rule $L \left\{ e_\alpha^{(1)}(t) \right\} = s\tilde{e}_\alpha^{(0)} - e_\alpha^{(0)}(0^+) = s\frac{s^{\alpha-1}}{s^{\alpha+1}} - 1 = -\frac{1}{s^{\alpha+1}}$ (GM, (3.14)). Hence the transform (D.8a) becomes

$$\begin{aligned} \tilde{u}(s) &= \sum_{k=0}^{\hat{\alpha}} c_k \mu^{-k-1} \frac{(s/\mu)^{\alpha-k-1}}{(s/\mu)^\alpha + 1} + \mu^{-\alpha} \frac{1}{(s/\mu)^\alpha + 1} \tilde{q}(s) \\ &= \sum_{k=0}^{\hat{\alpha}} c_k \frac{s^{\alpha-k-1}}{s^\alpha + \mu^\alpha} + \frac{1}{s^\alpha + \mu^\alpha} \tilde{q}(s) \\ &= \sum_{k=0}^{\hat{\alpha}} c_k \frac{s^{\alpha-k-1}}{s^\alpha - \lambda} + \frac{1}{s^\alpha - \lambda} \tilde{q}(s). \end{aligned} \quad (\text{D.8b})$$

Multiplying by $1 - \lambda/s^\alpha = (s^\alpha - \lambda)/s^\alpha$ gives

$$\begin{aligned} (1 - \lambda/s^\alpha) \tilde{u}(s) &= \sum_{k=0}^{\hat{\alpha}} c_k \frac{1}{s^{k+1}} + \frac{1}{s^\alpha} \tilde{q}(s), \\ \text{that is, } \tilde{u}(s) - \sum_{k=0}^{\hat{\alpha}} c_k \frac{1}{s^{k+1}} &= \lambda \frac{1}{s^\alpha} \tilde{u}(s) + \frac{1}{s^\alpha} \tilde{q}(s). \end{aligned} \quad (\text{D.8c})$$

Take the inverse Laplace transform:

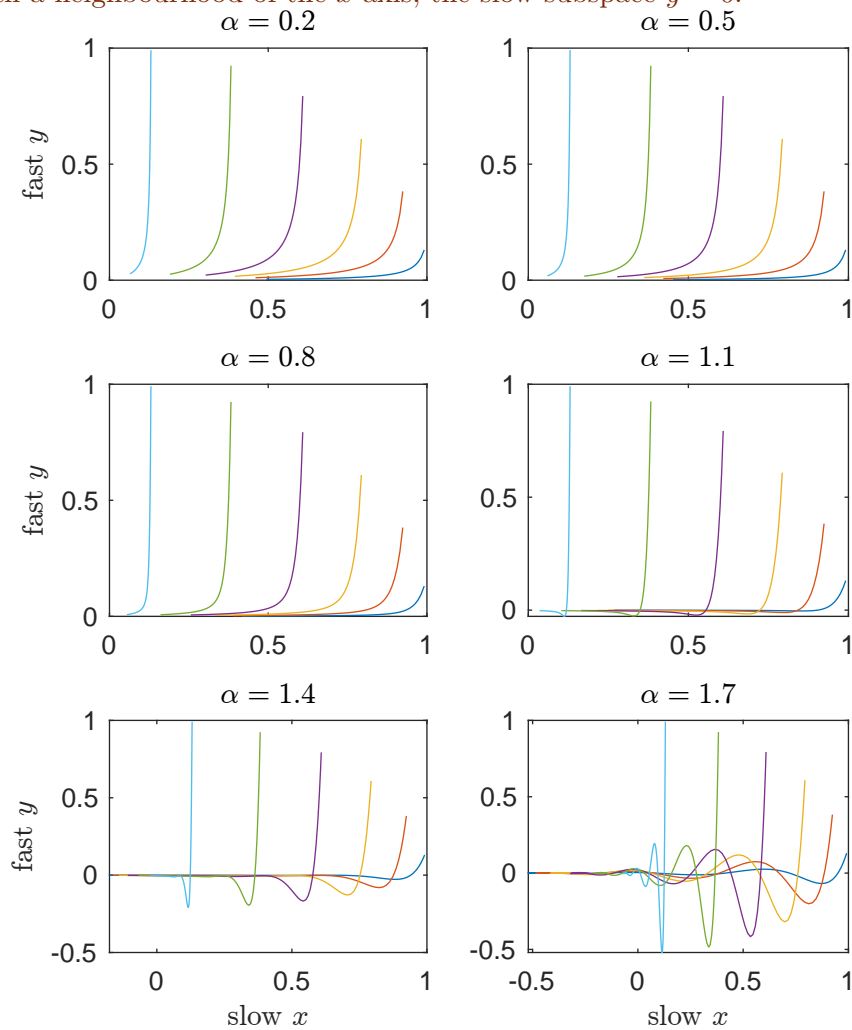
$$u(t) - \sum_{k=0}^{\hat{\alpha}} c_k \frac{t^k}{k!} = \lambda \frac{t^{\alpha-1}}{\Gamma(\alpha)} \star u(t) + \frac{t^{\alpha-1}}{\Gamma(\alpha)} \star q(t) = \lambda \mathcal{J}^\alpha u(t) + \mathcal{J}^\alpha q(t). \quad (\text{D.8d})$$

Since $\partial_t^\alpha u = \mathcal{J}^{-\alpha} \left[u(t) - \sum_{k=0}^{\hat{\alpha}} u^{(k)}(0^+) \frac{t^k}{k!} \right]$ (GM, (1.20)), identifying $c_k = u^{(k)}(0^+)$, and applying the operator $\mathcal{J}^{-\alpha}$ to (D.8d) immediately gives that the $u(t)$ of (D.2) satisfies the FDE (D.1), as required. \square

References

- Alavi, S. E., Ganghoffer, J. F., Reda, H. & Sadighi, M. (2023), ‘Hierarchy of generalized continua issued from micromorphic medium constructed by homogenization’, *Continuum Mechanics and Thermodynamics* **35**(6), 2163–2192.
- Anthoine, A. (2010), ‘Second-order homogenisation of functionally graded materials’, *International Journal of Solids and Structures* **47**(11), 1477–1489.
- Arneodo, A., Couillet, P. H., Spiegel, E. A. & Tresser, C. (1985), ‘Asymptotic chaos’, *Physica D* **14**, 327–347.

Figure 15: elementary emergence of a slow subspace. Plot six representative trajectories of the ‘multiscale’ FDE system in $(x(t), y(t))$: $\partial_t^\alpha x = -0.03x$ and $\partial_t^\alpha y = -y$. The six subplots are for six different $\alpha \in (0, 2)$. The trajectories show, especially for $\alpha \approx 1$, that solutions of the system reasonably quickly reach a neighbourhood of the x -axis, the slow subspace $y = 0$.



- Aulbach, B. & Wanner, T. (2000), ‘The Hartman–Grobman theorem for Caratheodory-type differential equations in Banach spaces’, *Nonlinear Analysis* **40**, 91–104.
- Bates, P. W., Lu, K. & Zeng, C. (1998), *Existence and persistence of invariant manifolds for semiflows in Banach space*, Vol. 135 of *Memoirs Amer. Math. Soc.*, Amer. Math. Soc.
http://books.google.com.au/books?hl=en&lr=&id=mVUHNtSNaaIC&oi=fnd&pg=PA1&dq=related:ctpLfDZ0LS4J:scholar.google.com/&ots=3TYgcQ_Jk0&sig=gn6D1qQcsyq51ScDe2LX0HtFWGo#v=onepage&q&f=false
- Bažant, Z. P. & Jirásek, M. (2002), ‘Nonlocal Integral Formulations of Plasticity and Damage: Survey of Progress’, *Journal of Engineering Mechanics* **128**(11), 1119–1149.
- Bender, C. M. & Orszag, S. A. (1981), *Advanced mathematical methods for scientists and engineers: Asymptotic methods and perturbation theory*, McGraw–Hill.
- Bokhove, O. & Shepherd, T. G. (1996), ‘On the Hamiltonian balanced dynamics and the slowest invariant manifold’, *J. Atmos Sci* **53**(2), 276–297.
- Boyd, J. P. (1995), ‘Eight definitions of the slow manifold: seiches, pseudoseiches and exponential smallness’, *Dynamics of Atmospheres and Oceans* **22**(1–2), 49–75.
<http://www.sciencedirect.com/science/article/B6VCR-3YCMH9H-B/2/1a3f0392189659c07097640f3a502dfc>
- Brenner, M. P. & Koumoutsakos, P. (2021), ‘Editorial: Machine Learning and Physical Review Fluids: An Editorial Perspective’, *Physical Review Fluids* **6**(7), 070001.
- Bunder, J. E. & Roberts, A. J. (2021), ‘Nonlinear emergent macroscale PDEs, with error bound, for nonlinear microscale systems’, *Springer Nature Applied Sciences* **3**(703), 1–28.
- Carr, J. (1981), *Applications of centre manifold theory*, Vol. 35 of *Applied Math. Sci.*, Springer–Verlag.
<http://books.google.com.au/books?id=93BdN7btysoc>
- Chekroun, M. D., Liu, H. & Wang, S. (2015), *Approximation of Stochastic Invariant Manifolds: Stochastic manifolds for nonlinear SPDEs I*, Springer Briefs in Mathematics, Springer, Cham.

- Chen, C., Roberts, A. J. & Bunder, J. E. (2018), ‘Boundary conditions for macroscale waves in an elastic system with microscale heterogeneity’, *IMA Journal of Applied Mathematics* **83**(3), 1–33.
<http://arxiv.org/abs/1603.06686>
- Chen, D., Gao, K., Yang, J. & Kitipornchai, S. (2024), *An introduction to functionally graded porous materials and composite structures*, Woodhead Publishing, chapter 1, pp. 3–15.
- Chen, Y., Hou, T. Y. & Wang, Y. (2023), ‘Exponentially convergent multi-scale methods for 2d high frequency heterogeneous helmholtz equations’, *Multiscale Modeling & Simulation* **21**(3), 849–883.
- Chernatynskiy, A., Phillpot, S. R. & LeSar, R. (2013), ‘Uncertainty quantification in multiscale simulation of materials: A prospective’, *Annual Review of Materials Research* **43**(1), 157–182.
- Combescure, C. (2022), ‘Selecting Generalized Continuum Theories for Non-linear Periodic Solids Based on the Instabilities of the Underlying Microstructure’, *Journal of Elasticity* .
- Cong, N. D., Doan, T. S., Siegmund, S. & Tuan, H. T. (2016), ‘On stable manifolds for fractional differential equations in high-dimensional spaces’, *Nonlinear Dynamics* **86**(3), 1885–1894.
- Cornaggia, R. & Guzina, B. B. (2020), ‘Second-order homogenization of boundary and transmission conditions for one-dimensional waves in periodic media’, *International Journal of Solids and Structures* **188–9**, 88–102.
- Craster, R. V. (2015), Dynamic homogenization, in V. V. Mityushev & M. Ruzhansky, eds, ‘Analytic Methods in Interdisciplinary Applications’, Vol. 116 of *Springer Proceedings in Mathematics and Statistics*, Springer, pp. 41–50.
- Cross, M. C. & Hohenberg, P. C. (1993), ‘Pattern formation outside of equilibrium’, *Rev. Mod. Phys.* **65**(3), 851–1112.
- Domb, C. & Sykes, M. F. (1957), ‘On the susceptibility of a ferromagnetic above the Curie point’, *Proc. Roy. Soc. Lond. A* **240**, 214–228.
- Efendiev, Y. & Leung, W. T. (2023), ‘Multicontinuum homogenization and its relation to nonlocal multicontinuum theories’, *Journal of Computational Physics* **474**(111761), 1–20.
- Fateman, R. (2003), ‘Comparing the speed of programs for sparse polynomial multiplication’, *ACM SIGSAM Bulletin* **37**(1), 4–15.
<http://www.cs.berkeley.edu/~fateman/papers/fastmult.pdf>
- Fish, J., Wagner, G. J. & Keten, S. (2021), ‘Mesoscopic and multiscale modelling in materials’, *Nature Materials* **20**(6), 774–786.

- Forest, S. & Trinh, D. K. (2011), ‘Generalized continua and non-homogeneous boundary conditions in homogenisation methods’, *ZAMM—Journal of Applied Mathematics and Mechanics / Zeitschrift für Angewandte Mathematik und Mechanik* **91**(2), 90–109.
- Frank, M., Drikakis, D. & Charissis, V. (2020), ‘Machine-learning methods for computational science and engineering’, *Computation* **8**(15), 1–35.
- Golub, G. H. & van Loan, C. F. (2013), *Matrix computations*, 4th edition edn, John Hopkins University Press.
- Gorenflo, R. & Mainardi, F. (1997), Fractional calculus: Integral and differential equations of fractional order, in ‘Fractals and Fractional Calculus in Continuum Mechanics’, Vol. 378 of *International Centre for Mechanical Sciences*, Springer, Vienna.
- Guo, T., Kouznetsova, V. G., Geers, M. G. D., Veroy, K. & Rokoš, O. (2024), Reduced-order modeling for second-order computational homogenization with applications to geometrically parameterized elastomeric metamaterials, Technical report, arXiv.org.
- Haragus, M. & Iooss, G. (2011), *Local Bifurcations, Center Manifolds, and Normal Forms in Infinite-Dimensional Dynamical Systems*, Springer.
- Haubold, H. J., Mathai, A. M. & Saxena, R. K. (2011), ‘Mittag-Leffler Functions and Their Applications’, *Journal of Applied Mathematics* **2011**(e298628), 1–51.
- Hii, A. K. W. & El Said, B. (2022), ‘A kinematically consistent second-order computational homogenisation framework for thick shell models’, *Computer Methods in Applied Mechanics and Engineering* **398**, 115136.
- Hochs, P. & Roberts, A. J. (2019), ‘Normal forms and invariant manifolds for nonlinear, non-autonomous PDEs, viewed as ODEs in infinite dimensions’, *J. Differential Equations* **267**(12), 7263–7312.
- Hunter, C. (1987), ‘Oscillations in the coefficients of power series’, *SIAM J. Appl Math* **47**, 483–497.
- Jiang, K., Li, S. & Zhang, P. (2024), ‘Numerical Methods and Analysis of Computing Quasiperiodic Systems’, *SIAM Journal on Numerical Analysis* **62**(1), 353–375.
- Jiang, K. & Zhang, P. (2014), ‘Numerical methods for quasicrystals’, *Journal of Computational Physics* **256**, 428–440.
- Leung, W. T. (2024), Some convergence analysis for multicontinuum homogenization, Technical report, arXiv.org.

- Lorenz, E. N. (1986), ‘On the existence of a slow manifold’, *J. Atmos. Sci.* **43**, 1547–1557.
- Lorenz, E. N. (1992), ‘The slow manifold—what is it?’, *Journal of the Atmospheric Sciences* **49**(24), 2449–2451.
- Lorenz, E. N. & Krishnamurthy, V. (1987), ‘On the non-existence of a slow manifold’, *J. Atmos. Sci.* **44**, 2940–2950.
- Ma, L. & Li, C. (2015), ‘Center manifold of fractional dynamical system’, *Journal of Computational and Nonlinear Dynamics* **posted 23 July**.
- MacKenzie, T. (2005), Create accurate numerical models of complex spatio-temporal dynamical systems with holistic discretisation, PhD thesis, University of Southern Queensland.
https://research.usq.edu.au/download/9b26ce2d7d0bd72849b0e3b792cdd4ca16e7991f103845e89e61fa532c9484fe/22666361/Mackenzie_2005_whole.pdf
- Martin, A., Opreni, A., Vizzaccaro, A., Debeurre, M., Salles, L., Frangi, A., Thomas, O. & Touze, C. (2022), Reduced order modeling of geometrically nonlinear rotating structures using the direct parametrisation of invariant manifolds, Technical report, <https://hal.archives-ouvertes.fr/hal-03886793>.
- Mercer, B. S., Mandadapu, K. K. & Papadopoulos, P. (2015), ‘Novel formulations of microscopic boundary-value problems in continuous multiscale finite element methods’, *Computer Methods in Applied Mechanics and Engineering* **286**, 268–292.
- Mercer, G. N. & Roberts, A. J. (1990), ‘A centre manifold description of contaminant dispersion in channels with varying flow properties’, *SIAM J. Appl. Math.* **50**, 1547–1565.
- Mercer, G. N. & Roberts, A. J. (1994), ‘A complete model of shear dispersion in pipes’, *Jap. J. Indust. Appl. Math.* **11**, 499–521.
- Muncaster, R. G. (1983*a*), ‘Invariant manifolds in mechanics i: The general construction of coarse theories from fine theories’, *Arch. Rat. Mech. Anal.* **84**, 353–373.
- Muncaster, R. G. (1983*b*), ‘Invariant manifolds in mechanics ii: Zero-dimensional elastic bodies with directors’, *Arch. Rat. Mech. Anal.* **84**, 375–392.
- Natl Physical Lab (1961), *Modern Computing Methods*, Vol. 16 of *Notes on Applied Science*, 2nd edition edn, Her Majesty’s Stationery Office, London.
- Potzsche, C. & Rasmussen, M. (2006), ‘Taylor approximation of integral manifolds’, *Journal of Dynamics and Differential Equations* **18**, 427–460.

- Prizzi, M. & Rybakowski, K. P. (2003), ‘On inertial manifolds for reaction-diffusion equations on genuinely high-dimensional thin domains’, *Studia Mathematica* **154**(3), 253–275.
- Rizzi, G., Hütter, G., Madeo, A. & Neff, P. (2021), ‘Analytical solutions of the simple shear problem for micromorphic models and other generalized continua’, *Archive of Applied Mechanics* **91**(5), 2237–2254.
- Roberts, A. J. (1988), ‘The application of centre manifold theory to the evolution of systems which vary slowly in space’, *J. Austral. Math. Soc. B* **29**, 480–500.
- Roberts, A. J. (1989), ‘Appropriate initial conditions for asymptotic descriptions of the long term evolution of dynamical systems’, *J. Austral. Math. Soc. B* **31**, 48–75.
- Roberts, A. J. (1992), ‘Boundary conditions for approximate differential equations’, *J. Austral. Math. Soc. B* **34**, 54–80.
- Roberts, A. J. (1993), ‘The invariant manifold of beam deformations. part 1: the simple circular rod’, *J. Elas.* **30**, 1–54.
- Roberts, A. J. (1996), ‘Low-dimensional models of thin film fluid dynamics’, *Phys. Letts. A* **212**, 63–72.
- Roberts, A. J. (1997), ‘Low-dimensional modelling of dynamics via computer algebra’, *Computer Phys. Comm.* **100**, 215–230.
- Roberts, A. J. (2000), ‘Computer algebra derives correct initial conditions for low-dimensional dynamical models’, *Computer Phys. Comm.* **126**(3), 187–206.
- Roberts, A. J. (2015a), ‘Macroscale, slowly varying, models emerge from the microscale dynamics in long thin domains’, *IMA Journal of Applied Mathematics* **80**(5), 1492–1518.
- Roberts, A. J. (2015b), *Model emergent dynamics in complex systems*, SIAM, Philadelphia.
<https://epubs.siam.org/doi/10.1137/1.9781611973563>
- Roberts, A. J. (2021), Rigorous modelling of nonlocal interactions determines a macroscale advection-diffusion PDE, in D. R. Wood, J. d. Gier, C. E. Praeger & T. Tao, eds, ‘2019-20 MATRIX Annals’, MATRIX Book Series, Springer International Publishing, pp. 423–437.
- Roberts, A. J. (2022), Backwards theory supports modelling via invariant manifolds for non-autonomous dynamical systems, Technical report, [<http://arxiv.org/abs/1804.06998>].

- Roberts, A. J. (2024), ‘Embed in ensemble to rigorously and accurately homogenise quasi-periodic multi-scale heterogeneous material’, *ANZIAM Journal* **accepted 08-Mar-2024**.
- Roberts, A. J. & Bunder, J. E. (2017), ‘Slowly varying, macroscale models emerge from microscale dynamics over multiscale domains’, *IMA Journal of Applied Mathematics* **82**, 971–1012.
<http://arxiv.org/abs/1612.02079>
- Roberts, A. J. & Li, Z. (2006), ‘An accurate and comprehensive model of thin fluid flows with inertia on curved substrates’, *J. Fluid Mech.* **553**, 33–73.
- Roberts, A. J., MacKenzie, T. & Bunder, J. (2014), ‘A dynamical systems approach to simulating macroscale spatial dynamics in multiple dimensions’, *J. Engineering Mathematics* **86**(1), 175–207.
- Roberts, A. J. & Strunin, D. V. (2004), ‘Two-zone model of shear dispersion in a channel using centre manifolds’, *Quart. J. Mech. Appl. Math.* **57**, 363–378.
- Rokoš, O., Ameen, M. M., Peerlings, R. H. J. & Geers, M. G. D. (2019), ‘Micromorphic computational homogenization for mechanical metamaterials with patterning fluctuation fields’, *Journal of the Mechanics and Physics of Solids* **123**, 119–137.
- Rosencrans, S. (1997), ‘Taylor dispersion in curved channels’, *SIAM J. Appl. Math.* **57**, 1216–1241.
<http://www.jstor.org/stable/2951850>
- Sanderse, B., Stinis, P., Maulik, R. & Ahmed, S. E. (2024), Scientific machine learning for closure models in multiscale problems: a review, Technical report, arXiv.org.
- Sarhil, M., Scheunemann, L., Lewintan, P., Schröder, J. & Neff, P. (2024), A computational approach to identify the material parameters of the relaxed micromorphic model, Technical report, arXiv.org.
- Siettos, C. & Russo, L. (2021), ‘A numerical method for the approximation of stable and unstable manifolds of microscopic simulators’, *Numerical Algorithms* .
- Sijbrand, J. (1985), ‘Properties of center manifolds’, *Trans. Amer. Math. Soc.* **289**(2), 431–469.
- Somnic, J. & Jo, B. W. (2022), ‘Status and challenges in homogenization methods for lattice materials’, *Materials* **15**(2), 605.
- Suslov, S. A. & Roberts, A. J. (1999), ‘Advection-dispersion in symmetric field-flow fractionation channels’, *J. Math. Chem.* **26**, 27–46.

- Suslov, S. A. & Roberts, A. J. (2000), ‘Modelling of sample dynamics in rectangular asymmetrical flow field-flow fractionation channels’, *Analytical Chemistry* **72**(18), 4331–4345.
- Touze, C. & Amabili, M. (2006), ‘Nonlinear normal modes for damped geometrically nonlinear systems: Application to reduced-order modelling of harmonically forced structures’, *J. Sound & Vibration* **298**(4–5), 958–981.
- Touzé, C. & Vizzaccaro, A. (2021), ‘Model order reduction methods for geometrically nonlinear structures: a review of nonlinear techniques’, *Nonlinear Dynamics* **105**(2), 1141–1190.
- van Kampen, N. G. (1985), ‘Elimination of fast variables’, *Physics Reports* **124**, 69–160.
- Vanneste, J. & Yavneh, I. (2004), ‘Exponentially small inertia-gravity waves and the breakdown of quasigeostrophic balance’, *J. Atmos. Sci.* **61**, 211–223.
- Wanga, F., Wang, Y., Leung, W. T. & Xu, Z. (2024), Learning-based multi-continuum model for multiscale flow problems, Technical report, arXiv.org.
- Watt, S. D. & Roberts, A. J. (1995), ‘The accurate dynamic modelling of contaminant dispersion in channels’, *SIAM J. Appl. Math.* **55**(4), 1016–1038.